University of California, Merced

Engineering Multifunctional Nanoparticle Assemblies through DNA Guided Self-Assembly

A dissertation submitted in partial satisfaction of the

requirements for the degree Doctor of Philosophy

in

Chemistry and Biochemistry

by

Paniz Rahmani

2023

Committee Members:

Professor Yue Wang, Chair

Professor Tao Ye, Advisor

Professor Michael Scheibner

Professor Shahar Sukenik

The Dissertation of Paniz Rahmani is approved, and it is acceptable in quality and form for publication on microfilm and in digital formats.

Professor Tao Ye, Advisor

Professor Yue Wang, Chair

Professor Michael Scheibner

Professor Shahar Sukenik

University of California, Merced

2022

Table of Contents

Acknowledgement

As I conclude my doctoral journey, I wish to express my deep appreciation to those who have been instrumental in enabling me to achieve this academic milestone. It is a privilege to extend my gratitude to those who have selflessly offered their support, encouragement, and guidance during this journey.

First and foremost, I express my profound gratitude to my beloved parents and brother. Their unwavering love and support have been a continuous source of inspiration and have enabled me to persist in the face of seemingly insurmountable challenges. I would like to especially acknowledge their decision to let me pursue my academic aspirations abroad in the United States. Though this decision entailed a great deal of sacrifice, it was their love and dedication that made it possible for me to continue my journey. Despite the geographical distance, their support remained constant throughout my academic journey, and for that, I will be eternally grateful.

Second, I would also like to express my heartfelt gratitude to my advisor, Dr.Tao Ye, for his mentorship and guidance throughout my doctoral journey. His profound knowledge, and dedication to my success have been a constant source of inspiration and have enabled me to reach this significant academic achievement. He has consistently provided invaluable feedback and constructive criticism, enabling me to improve my research work's quality and depth. Additionally, I am grateful to my colleagues, lab mates, Melissa Goodlad, Zachary Petrek, Rambod Rezayan and Yehan Zhang. I would also like to express my sincere gratitude to Dr.Huan Cao, for his mentorship, support, and contributions to my research work. His extensive knowledge, expertise, and guidance have been invaluable in helping me navigate the challenges and opportunities that arose during my doctoral studies.

I would also like to extend my sincere gratitude to my committee members Dr.Wang, Dr.Sukenik and Dr.Scheibner, who have supported me throughout my doctoral journey. Their expertise, insight, and constructive feedback have been invaluable in shaping my research and enriching my academic journey. Their unwavering support and guidance have encouraged me to develop a deeper understanding of my field and to pursue research questions that are both innovative and impactful.

I am also deeply grateful to my friends who have been there for me through thick and thin. Their unwavering friendship, support, and kindness have helped me persevere through difficult times. Their encouragement and unwavering presence have provided me with an alternative support system in times of need, making the academic journey more manageable and fulfilling.

Finally, I wish to dedicate my dissertation to the brave women in Iran, who are fighting for their freedom and gender equality in the Women's Life, Freedom movement. Their resilience and perseverance in the face of oppression are an inspiration to me and countless others. As an Iranian woman myself, I am deeply committed to contributing to the empowerment of women in my country and across the globe. I am hopeful that my dedication to gender equality will bring about positive change and create a more equitable future for women.

Curriculum Vitae

Education

Ph.D. in Biophysical & Nanomaterial Chemistry | University of California Merced

Merced, CA Aug 2017-May 2023

Thesis title: Engineering Multifunctional Nanoparticle Assemblies through DNA Guided Self-Assembly

Master of Science in Organic Chemistry | Southern Illinois University Edwardsville

Edwardsville, IL Jan 2016-Aug 2017

Thesis title: Study of the Primary Isotope Dependence of the Secondary Kinetic Isotope Effects and Hammett Correlations in Hydride Transfer Reactions in Solution

Bachelor of Science Chemistry | Shahid Beheshti University

Tehran, Iran | Aug 2008-May 2012

Non-thesis: Development of enhanced palladium (Pd) nanocomposites medical nonenzymatic sensors for glucose and hydrogen peroxide detection

Publications

- Rahmani, P.; Goodlad, M.; Zhang, Y.; Li, Y.; Ye, T. One-Step Ligand-Exchange Method to Produce Quantum Dot–DNA Conjugates for DNA-Directed Self-Assembly.*ACS Applied Materials & Interfaces* **2022**, *14* (42), 47359-47368
- Ma, L.; Sakhaee, N.; Jafari, S.; Wilhelm, S.; Rahmani, P.; Lu, Y. Imbalanced Transition States from α-H/D and Remote β-Type N-CH/D Secondary Kinetic Isotope Effects on the NADH/NAD+ Analogues in Their Hydride Tunneling Reactions in Solution. *The Journal of Organic Chemistry* **2019**, *84* (9), 5431-5439
- Hosseini, H.; Rezaei, S. J. T.; Rahmani, P.; Sharifi, R.; Nabid, M. R.; Bagheri, A. Nonenzymatic glucose and hydrogen peroxide sensors based on catalytic properties of palladium nanoparticles/poly(3,4-ethylenedioxythiophene) nanofibers. *Sensors and Actuators B: Chemical* **2014**, *195*, 85-91

Selected Honors and Awards

- UC Merced Chemistry and Chemical Biology Department Rresearch Fellowship, 2021

- Center for Cellular and Biomolecular Machines Scholar by NSF-CREST, 2018-2021
- Graduate Dean Steve Hanson Symposium Poster Award, by Phi Kappa Phi and SIUE, 2017
- Southern Illinois University Edwardsville Thomas D. Bouman Memorial Research

  Award, March *2017 by SIUE and sigma Aldrich*
- Best Graduate Student Research Award, *Chemistry Department of Southern Illinois*

  University Edwardsville December 2016
- Honored *Southern Illinois University Edwardsville* dean's list *2016-2017*
- Research Grant for graduate students Award (RGGS), *Southern Illinois University*

  Edwardsville, December *2016*

Selected Presentations

- American Chemical Society National meeting (ACS), 2019 & 2022 San Diego, CA
- Quantum Atomic and Molecular tunneling in solids and other condensed phases, 2017 Madison, WI

Abstract of the Dissertation

Engineering Multifunctional Nanoparticle Assemblies through DNA Guided Self-Assembly

by

Paniz Rahmani

Doctor of Philosophy in Chemistry and Biochemistry

University of California, Merced, 2023

DNA nanotechnology is a rapidly evolving field that exploits the remarkable properties of DNA molecules to create complex and functional nanostructures. One of the key techniques in DNA nanotechnology is self-assembly, wherein DNA molecules are designed to interact and assemble into specific structures with precise control over their size, shape, and composition. This dissertation focuses on the self-assembly of plasmonic, fluorescent, and magnetic nanoparticles in both 2D and 3D using DNA as a programmable scaffold, and explores their applications in various areas, including biosensing and magnetic metamaterials.

Chapter 1 provides a comprehensive overview of DNA nanotechnology, self-assembly techniques, and DNA origami. The principles of DNA self-assembly are discussed, including the design rules for creating DNA nanostructures with precise control over their shape and size. The versatility of DNA as a programmable scaffold is highlighted, allowing for the assembly of diverse nanoparticles with unique functionalities. The chapter also discusses the fundamentals of DNA origami, a powerful technique that utilizes the folding of a long single-stranded DNA template to create complex nanostructures with high precision.

In Chapter 2, a novel ligand exchange method is presented, which allows for the functionalization of quantum dots (QDs) with DNA to form self-assembled heterodimers. The heterodimers serve as probes for detection, with one QD acting as a reporter and the other AuNP (gold nanoparticle) as a quencher. The chapter elaborates on the design and fabrication of the QD-AuNP heterodimer. The changes in photoluminescence (PL) signals upon binding of the heterodimers to target DNA molecules are investigated.

Chapter 3 focuses on the application of the heterodimer probes in the development of a biosensor for nucleic acid detection. The biosensor is designed based on the change in PL signal upon target DNA binding, allowing for sensitive and selective detection. The chapter provides details on the fabrication and characterization of the biosensor, including the optimization of experimental parameters such as probe design and concentration, and target DNA concentration. The performance of the biosensor is also evaluated using different target DNA concentrations. The kinetics of the DNA displacement process in the biosensor are also investigated, shedding light on the dynamics of target DNA binding and release from the heterodimers.

In Chapter 4, a novel method for the self-assembly of gold-coated magnetic nanoparticles in 3D using DNA as a scaffold is presented. The chapter discusses the fabrication of DNA-modified magnetic nanoparticles and their subsequent self-assembly into 3D structures by exploiting the programmable base-pairing interactions of DNA molecules. The chapter highlights the unique capabilities of this 3D self-assembly approach and discusses the future prospects and potential directions for further research in this area.

In conclusion, this dissertation presents a comprehensive investigation into the use of DNA nanotechnology for the self-assembly of plasmonic, fluorescent, and magnetic nanoparticles in 2D and 3D. The methods and findings presented in this dissertation contribute to the advancement of DNA nanotechnology and demonstrate the potential of self-assembled nanostructures for various applications, including biosensing, nucleic acid detection, DNA data storage and magneto-plasmonic measurements.

Chapter 1:

DNA Nanotechnology and Self-Assembly of Nanoparticles

1.1 Overview

Nanotechnology is a field of science and engineering that deals with the design, production, and manipulation of materials and devices at the nanoscale level, typically with dimensions ranging from 1 to 100 nanometers. This field has the potential to revolutionize many areas of technology, including medicine, electronics, energy, and materials. The goal of nanotechnology is to control materials at the nanometer scale to achieve the miniaturization of devices and the exploration of new functions. It is a field of study comprised of two subfields: first, the fabrication and application of nanomaterials; and second, the investigation of the relationship between the physical characteristics of nanomaterials and their dimensions. [4] As a result, the field of nanotechnology is very multidisciplinary. It encompasses the fabrication of nanoparticles, self-assembly, molecular biology, organic and polymer chemistry, surface science, and optical, magnetic, and condensed matter physics.

There are two main approaches to nanotechnology: bottom-up and top-down. The top-down approach to nanotechnology necessitates the shrinking of bulk materials to create nanostructures or surface patterns. A few examples include electron beam lithography (ref), which involves etching patterns into a material using a beam of electrons or ions, and chemical vapor deposition, which involves depositing a thin layer of material onto a substrate (ref). Other noteworthy examples include ball milling and photolithography (ref). One of the main advantages of a top-down approach is the ability to produce materials and devices on a large scale with a high degree of precision. This makes top-down approaches well-suited for the production of microelectronics and other industrial applications. However, top-down approaches can be limited by the high cost of equipment and the limited resolution of existing techniques. Additionally, the materials produced using top-down approaches may have limitations in terms of their properties and functionality.

Contrastingly, bottom-up approaches to nanotechnology start with molecules or atoms. They include self-assembly, which involves designing molecules that spontaneously organize themselves into a desired structure, and synthetic biology, which involves engineering biological systems to produce novel materials and devices. DNA nanotechnology is a prime example of a bottom-up approach, as it involves using the molecular properties of DNA to assemble complex structures and devices. The primary advantage of bottom-up approaches is the ability to create complex, three-dimensional structures with precision and control and engineer material functionalities at the molecular level. This allows for the creation of novel materials and devices with unique properties that cannot be achieved using traditional manufacturing techniques. Bottom-up approaches can be limited by the complexity of the molecular interactions involved as well as the difficulty of scaling up production. Additionally, the materials produced using bottom-up approaches may be less robust and stable than those produced using top-down approaches. In conclusion, both bottom-up and top-down approaches to nanotechnology have their own advantages and limitations. They are both used for nanofabrication and the study of nanomaterial properties. The choice of approach depends on the specific application and desired properties of the material or device being produced.

Nanomaterials have a number of extraordinary remarkable qualities that are a direct result of their small size as well as the distinctive chemical and physical properties that

exist at the nanoscale level.[5] Some of the most notable properties of nanomaterials are unique optical and mechanical properties, superior electrical conductivity, as well as their unique surface chemistry and high surface-to-bulk ratio which is mainly responsible for their high reactivity and enhances their ability to interact with other materials.

In addition to a nanomaterial's composition, the shape, size and its surface, in particular, play important roles in its chemical properties. The surface properties are crucial in the process of transforming the assembly of nanomaterials into superstructures. This is because the process relies on surface charge and surface ligand interactions. [6-9] Among all the techniques for assembling nanoparticles into superstructures[7, 9] the DNA-mediated self-assembly technique is one of the most powerful, in which the hybridization of surface DNA ligands can serve as bonds between nanoparticles. Due to the unique specificity of the Watson-Crick base pairing in DNA, Adenosine to Thymidine (A-T) and Guanosine to Cytidine (G-C), the strength, selectivity, and bond length could be modulated through the sequence design.

Over the last ten years, DNA functionalization of nanoparticles has made it possible to bring these colloidal particles into proximity and make highly ordered structures with nanometer precision. [3, 5, 10-12] In colloidal nanostructures, the physical characteristics of the various building blocks are merged to display a collective behavior that is not apparent in the constituent parts. To make such nanoarchitectures for any purpose, stable DNA-functionalized colloidal nanoparticles must be obtained, which remains a challenge in many cases. [13-16] In my dissertation, I aim to address some of these challenges and provide a number of possible solutions. Chapter 2 provides a solution for the surface functionalization of quantum dots (QD) with DNA and discusses how, combined with DNA self-assembly techniques, 2D nanostructures with optical characteristics could be made. Chapter 3 focuses on using such a structure to detect and design an optical-based DNA-assembly biosensor. Chapter 4 discusses the utilization of the DNA self-assembly technique to make a 3D superlattice of iron oxide magnetic nanoparticles.

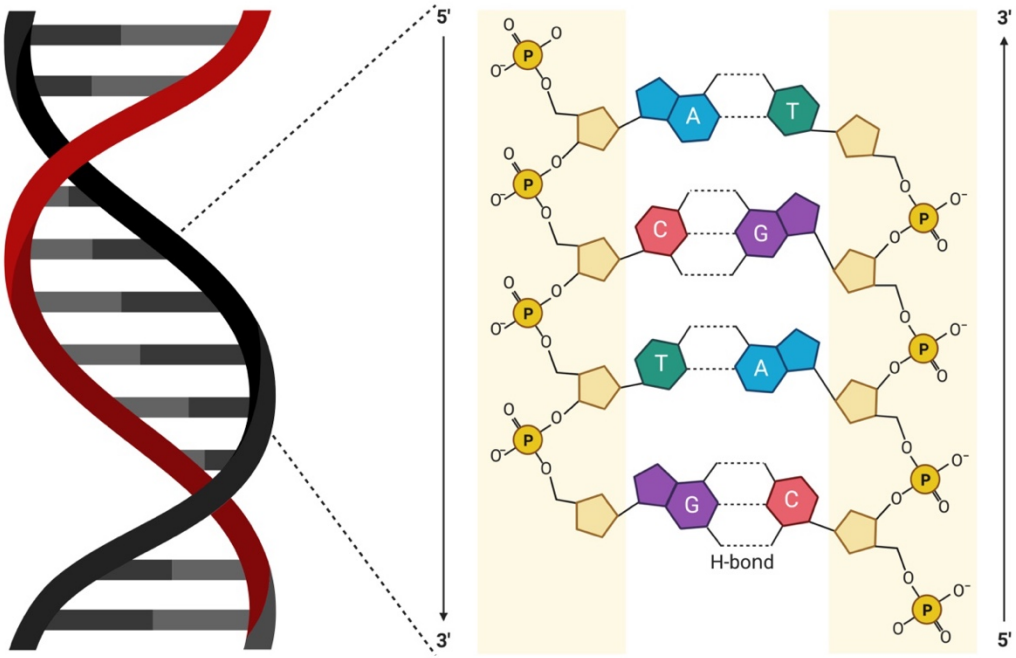

Figure 1. Illustration of DNA base pairing and hybridization.

1.1.1 Surface functionalization of nanoparticles with DNA

Functionalizing the surface with an adapter ligand is the first step in self-assembling nanoparticles, which can facilitate self-assembly through interparticle interactions. Since DNA-based self-assembly techniques are the primary method for templated assembly of nanoparticles, this section focuses mostly on the DNA functionalization methodology. So far, DNA has been successfully used to functionalize a wide variety of nanoparticles, including gold, quantum dots, and iron oxide, which exhibit plasmonic, optical, and magnetic characteristics, respectively. [9, 17-19] Gold nanoparticles are the simplest nanomaterials to study in terms of chemistry, optics, biology, and self-assembly because of their simple fabrication, easy surface modification, and adjustable optical and plasmonic characteristics. The plasmonic properties of Au nanoparticles are created through the interaction of the gold nanoparticle's surface electrons with incident light due to the combined influence of light absorption as well as the scattering on nanoparticles. The Mie theory predicts that, when the diameter of nanoparticles gets larger, both absorption and scattering values will rise. Absorption is the primary cause of extinction for particles smaller than 40 nm, while for larger diameters, scattering is more prominent. The extinction value is mostly influenced by scattering at sizes greater than 80 nm. The functionalization of gold nanoparticles not only increases their stability but also enables their practical applications, such as sensing.

The incorporation of thiol-modified DNA into nanoparticles is made possible by capitalizing on the strong covalent interaction that exists between thiol (-SH) and gold (Au), which has an adsorption energy of 40 kcal/mol. [1,20] Although surface functionalization is a relatively simple process, its effectiveness is dependent on a wide range of parameters and environmental circumstances. [21, 22] These include the careful design of the DNA ligand sequence, the pH of the reaction, the ratio of DNA to NP, and the concentration of salt and surfactants. For instance, the incorporation of surfactants like SDS, Tween, and Triton might stabilize the gold nanoparticles by generating an interdigitated bilayer structure in addition to exerting charge and steric stabilization. [22] This would be necessary in order to maintain an aggregation-free state for the nanoparticles. During the functionalization process, overcoming the electrostatic repulsion between the negatively charged DNA ligands is another important consideration. Although adding salt directly to screen charge repulsion is an option, this method is inapplicable to AuNPs for DNA attachment due to the problem of colloidal stability. Mirkin and his colleagues devised the salt-aging process in which the NaCl salt is gradually added to the reaction mixture and adjusted to a final concentration of ~0.5M.[22] It is also common knowledge that various DNA bases have varying degrees of attraction to the surface, with the order of adsorption energy being as follows: A > C > G > T > Phosphate. [23, 24] Because of this, the DNA ligand that is utilized for this method is often engineered to include a poly T-tail in order to avoid surface adsorption.[25, 26]

Quantum dots (QD), a nanoparticle with unique optical properties due to the quantum confinement effect, are commonly employed in biomedical research and bioimaging applications. These nanoparticles are often made using organometallic methods in organic solvents, making it more challenging to make them water-soluble so that they can interact with DNA ligands. This makes the DNA surface functionalization of these nanoparticles more challenging than that of gold nanoparticles. [27-29] Common methods for functionalizing these nanoparticles with DNA include surface ligand exchange with thiol or polyhistidine-modified DNA,[19, 30] covalent coupling of DNA to QD surface ligands through EDC or miscellaneous covalent conjugation (MCC) [31, 32] and incorporation of a DNA ligand during synthesis. [33] Magnetic iron oxide nanoparticles are another category of nanoparticles that find widespread use in therapeutics, cancer therapy, drug delivery, and magnetic resonance imaging (MRI). Contrary to QDs, iron oxide nanoparticles may be produced by a wide variety of inorganic processes in both organic and aqueous conditions. Co-precipitation, microemulsion, thermal decomposition, solvothermal, microwave-aided, chemical vapor deposition, and combustion procedures are some examples of these methods; however, generally, only organometallic approaches at high temperatures might yield monodispersed nanoparticles. [34-40] Due to their strong magnetic and dipolar interactions, producing monodispersed nanoparticles is difficult. Because of this, they are often densely coated with capping agents, which makes DNA functionalization of these nanoparticles challenging. In recent years, a handful of technologies and techniques for the functionalization of DNA have surfaced, including the application of gold coating. [41] Azide R-N3 (R=silica, PMAO) surface ligand through Cu[I]-catalyzed azide-alkyne Huisgen cycloadditions (CuAAC) click chemistry or DBCO-

modified DNA, [42, 43] biotin-streptavidin chemistry, [44] and DNA-grafted poly (acrylic acid) (PAA-g-DNA). [45]

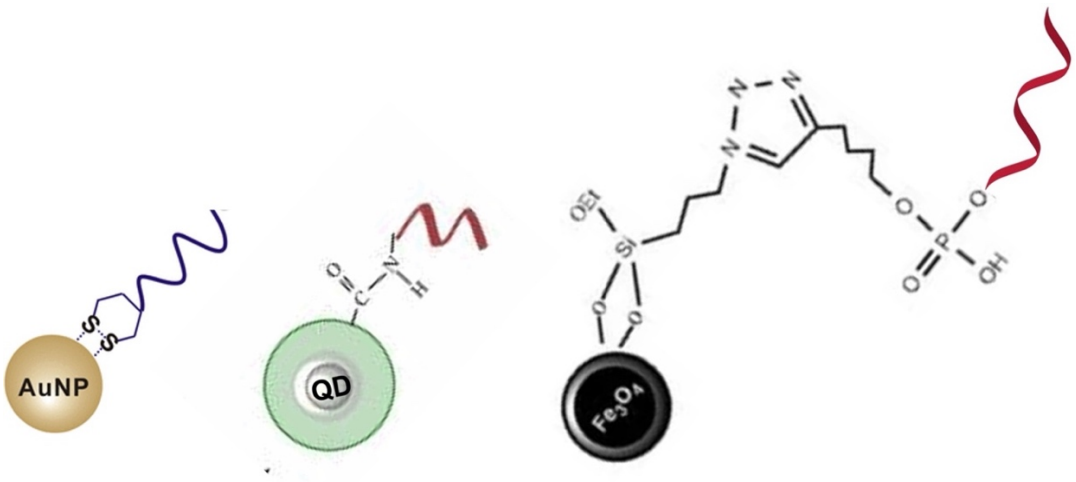

Figure 2.DNA functionalization of gold, quantum dot, and iron oxide nanoparticles.[44, 46, 47]

1.2 DNA-mediated self-assembly techniques

The term "self-assembly" refers to a process used extensively in nanotechnology and describes the spontaneous arrangement of separate components into ordered structures. The process of self-assembly is affected by several different elements. To begin, the system that assembles itself may have a single sort of component or several different kinds. The components may interact with one another through a dynamic interplay of forces that are both attractive and repulsive to one another. The interactions between the components must adhere to two principles in order to build ordered structures: first, they must be weak enough to allow reversible binding, and second, they must be strong enough to resist the disruptive forces that impede assembly. Additionally, whether in a solution or on the surface, the environment for self-assembly needs to provide the necessary mobility of the components in order for them to successfully complete the process of self-assembly by self-adjusting their orientation. [48]

In colloidal nanoparticles, their interactions are governed by the ligands on their surfaces. [49] The ligands are necessary reactants in the wet-chemistry synthesis of colloidal nanoparticles. When the dimensions of a particle are downsized to the nanoscale, The effects of nanoparticles' small sizes become more noticeable. The surface atoms then become more unstable and reactive as a result of the particles beginning to have an elevated surface energy. One of the most essential roles that ligands play is to reduce surface energy through the introduction of steric or electrostatic repulsion as a means of preventing aggregation. Most significantly, if the surface ligands that are supplied have the appropriate binding interactions, then nanoparticles have the potential to spontaneously arrange themselves into particular assemblies. [50, 51]

The self-assembly of nanoparticles allows for the transformation of amorphous aggregates into periodic and ordered geometries. Solitary nanoparticles and amorphous aggregates cannot compare to the various collective effects that can be exhibited by nanoparticles that are grouped in a periodic pattern. DNA-mediated self-assembly of nanoparticles can be categorized into two methods: first, direct self-assembly through surface ligand interactions, and second, DNA-templated self-assembly.

1.1.2 DNA-mediated self-assembly via direct linkage

Direct linkage organizes different components into specific structures using short DNA oligonucleotides as linker molecules. The DNA linkers are designed to have complementary sequences that can hybridize with specific regions on the surfaces of the components, enabling the components to be linked together in a specific way. The process of direct linkage typically involves several steps. First, the components to be assembled are modified with functional groups that can bind to the DNA linker molecules. Then, the DNA linkers are designed and synthesized with specific sequences that are complementary to the functional groups on the components. Next, the components and DNA linkers are mixed together in a solution, and the complementary sequences on the DNA linkers hybridize with the functional groups on the components, creating a stable linkage between the components. By designing the DNA linkers with different sequences and lengths, it is possible to control the overall structure of the assembled components. [52-54] Aside from hybridization of complementary strands of DNA, hydrogen bonds, coordination bonds, charge-charge interactions, and dipole-dipole interactions are some of the interactions that can be used for self-assembly. The distinguishing feature of these interactions is their non-covalent nature. Under thermodynamic equilibrium conditions, the self-assembly process can be advanced by nanoparticles that have been functionalized with these molecular pairs. The continuous binding and unbinding of free species to precursors allows newly formed components to automatically change orientations and locations. An effective collision can take place only when new components link to existing ones through a predefined minimum threshold of cooperative non-covalent interactions. At some point in time, the system's free energy will be reduced to a minimum, and the self-assembly process will be accomplished. [6, 48, 55]

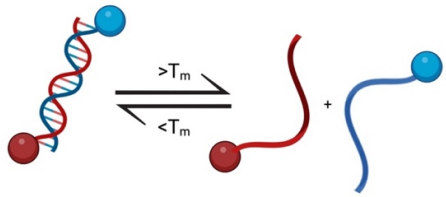

Figure 3. hybridization of DNA complementary strands below the melting temperature can lead be used for organizing nanoparticles.

DNA is one type of ligand that has received a lot of attention as a possible way to introduce directed interactions to surface isotropic nanoparticles. The straightforward concept that complementary DNA strands will hybridize (Figure 3) and the ability to adjust the intensity of the hybridization reaction by temperature, strand length, and sequence make it possible to create extremely precise orthogonal interactions. The production of densely packed, three-dimensional nanoparticle crystals may be the result of sequence-based hybridization of oligonucleotides at the recognition sites. Figure 3 depicts a few examples of direct DNA-assisted self-assembly techniques to make ordered 2D and 3D structures.

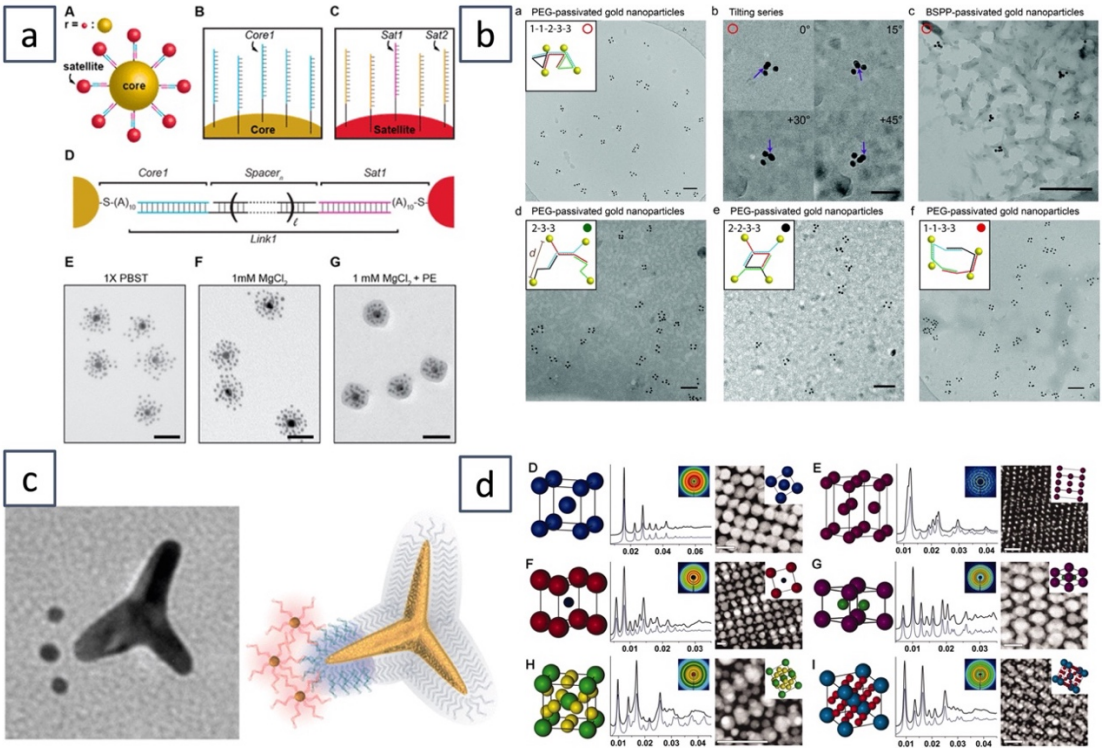

Figure 4. Direct DNA-mediated self-assembly of nanoparticles. a)construction of nanosatellites using polyvalent counterions[56] b)Plasmonic isomers via DNA-based self-assembly of gold nanoparticles[57] c)Light-Mediated Directed Placement of Different DNA Sequences on Single Gold Nanoparticles[58] d)nanoparticle superlattice engineering with DNA.[59]

1.1.3 Binding to DNA templates

DNA templated self-assembly is a technique that uses DNA as a template to organize various components or molecules into specific structures. This technique is based on the programmable base-pairing of DNA, where complementary strands of DNA bind together to form a stable double-stranded structure. The use of DNA as a template allows for precise control over the location and orientation of the assembled components. [1, 10, 60]

The basic process of DNA templated self-assembly involves designing and synthesizing DNA strands with specific sequences that will serve as templates for assembling the different components. These DNA strands are typically modified with functional groups that can bind to the desired components, either directly or through linker molecules. Once the DNA templates and components are mixed together, the programmable base-pairing of DNA directs the assembly of the components into the desired structure. For example, if the DNA template is designed to form a particular shape, such as a cube or a tetrahedron, the components will assemble around the template to form that shape. [2, 61]

Once the DNA templates and components are mixed together, the programmable base-pairing of DNA directs the assembly of the components into the desired structure. For example, if the DNA template is designed to form a particular shape, such as a cube or a tetrahedron, the components will assemble around the template to form that shape.[2, 61] This technique has the advantage of high precision and reproducibility, which can be difficult to achieve with other self-assembly methods. [62, 63] Furthermore, because DNA is a biocompatible material, it is frequently used in biomedical applications. One of the earliest attempts to utilize DNA as a framework to self-assemble diverse components was the crystallization of proteins using a pre-assembled DNA brand by Seeman et al. [64, 65] A few years later, the same group of researchers revealed what was essentially the first DNA cube construction in three dimensions. A new area of study, known as "structural DNA nanotechnology," was established as a result of a subsequent breakthrough that involved the utilization of unique DNA patterns to construct specific forms and assemblies. [66-68] Over the last thirty years, DNA templated self-assembly has emerged as one of the most efficient techniques for assembling single DNA strands into complex objects that could be used for a variety of applications. The three main structures used in DNA self-assembly for DNA nanotechnology are DNA tiles, DNA origami, and bricks. [61, 69-71]

DNA-tile is an example of previous attempts in the field of DNA nanotechnology. [72] Specifically, it performs an initial assembly of short DNA oligonucleotides into DNA-tile structures that have a predetermined shape. Interactions between adjacent DNA tiles result in them being assembled into larger structures. Single-stranded DNA bricks are used to create complex structures directly from individual DNA strands. [73] This concept is quite comparable to the notion of DNA-tile-based assembly. DNA-origami is another well-known DNA templated self-assembly method that involves folding a long single-stranded DNA scaffold of approximately 7K bases to construct a customized 2D or 3D nanosized structure on a scale ranging from a few tens to several hundred nanometers. Instead of using only short, single-stranded DNA oligonucleotides, this method makes use of the interactions between the various scaffold segments by using a large number of short oligonucleotides called "staples" to create the structures (Figure 3). [72-74] After the formation of the DNA template is complete, nanoparticles or any other desired components can be site-specifically assembled on predetermined locations of the template through Watson-Crick base pairing between their surface DNA ligand and the capture strands on the template. Self-assembled structures of proteins and gold nanoparticles in 2D and 3D are shown in Figure 4.

Site-specific deposition of nanoparticles on prefabricated DNA nanostructures has distinct advantages over packing them into 3D lattices. First, the structural stiffness and connection are provided by the DNA template. On the DNA structures, nanoparticles are positioned in certain locations, as it is not required to have direct interactions between nanoparticles. Second, the size of the DNA templates determines how large an assembly of nanoparticles will be. Thirdly, the deposition of nanoparticles on DNA templates may generate additional driving forces, which in turn may cause the DNA templates to take on a variety of diverse forms. For instance, the placement of gold nanoparticles compels DNA tile-based structures to adopt a tubular structure due to the steric repulsion forces. [75, 76] On the one hand, DNA-templated self-assembly offers the assembly of nanoparticles more latitude. The same DNA structures may spontaneously host a variety of nanoparticle types. Alternately, high-quality large DNA templates are required for large-scale assembly of guest nanocomponents. The programmable creation of properly specified monomeric DNA templates and the precise regulation of the extent of interaction between monomers are now made possible by DNA self-assembly. [77, 78]

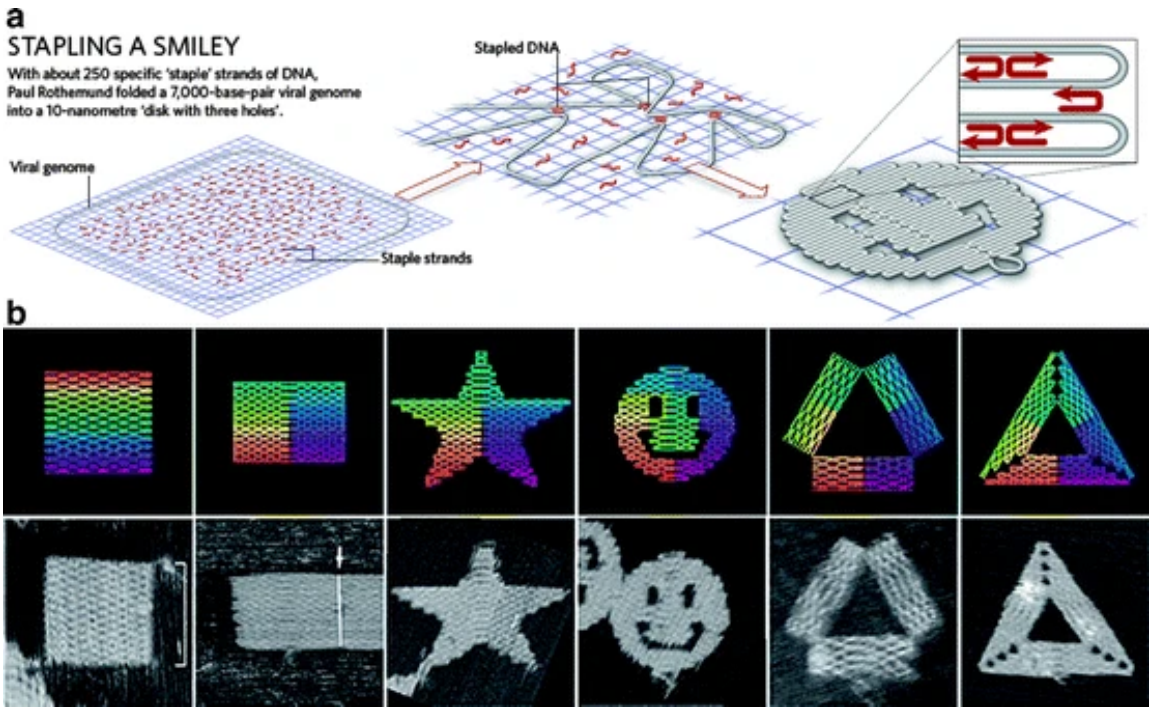

Figure 3. DNA origami folded scaffold into different shapes.[72, 79]

1.1.4 DNA origami

Scaffolded DNA origami, which represents the pinnacle of structural DNA nanotechnology, provides a unique approach for the precise control of site-specific and programmable self-assembly. [61, 72, 80] In 2004, the first use of this approach was demonstrated by William Shih's group, which folded a long single-stranded DNA molecule with 1669 bases together with five oligonucleotides of 40 bases into the shape of

an octahedron with a 20-nm diameter. [81] In 2006, Rothemund *et al.* devised a straightforward and versatile strategy for fabricating 2-dimensional nanosized structures via directly folding a bacteriophage single-strand DNA of 7249 bases and employing more than 200 short ssDNA staples to keep the scaffold in place. This is referred to as a DNA template. William Shih et al. were later able to create more complex, three-dimensional, multi-layer DNA solid structures with precisely defined forms by extending this technique. [61]

DNA origami has a number of advantages compared to other forms of self-assembly. To begin, the fundamental design principles of scaffolded DNA origami have been extensively studied. It is quite likely that the cooperative assembly of one hundred short staple oligos or the synergistic function of these oligos causes the single-stranded DNA scaffold to conform to the predefined monomeric DNA nanostructures. The sequence of each staple strand as well as its place within that sequence have been precisely determined, which adds a programmability feature to the DNA self-assembly technique. Also, scaffold-guided assembly combined with a densely packed helix results in a rigid DNA structure. Furthermore, computer-aided design software such as caDNAno and CanDo is available to design arbitrary shapes. [82, 83] There are established design algorithms, [84] standard annealing and purification protocols, [85] and characterization techniques for the design and folding of monomeric DNA origami structures. With the ability to form monomeric designer structures, these individual structures have the potential to be polymerized into larger structures and create macroscopic functional devices. [86, 87]

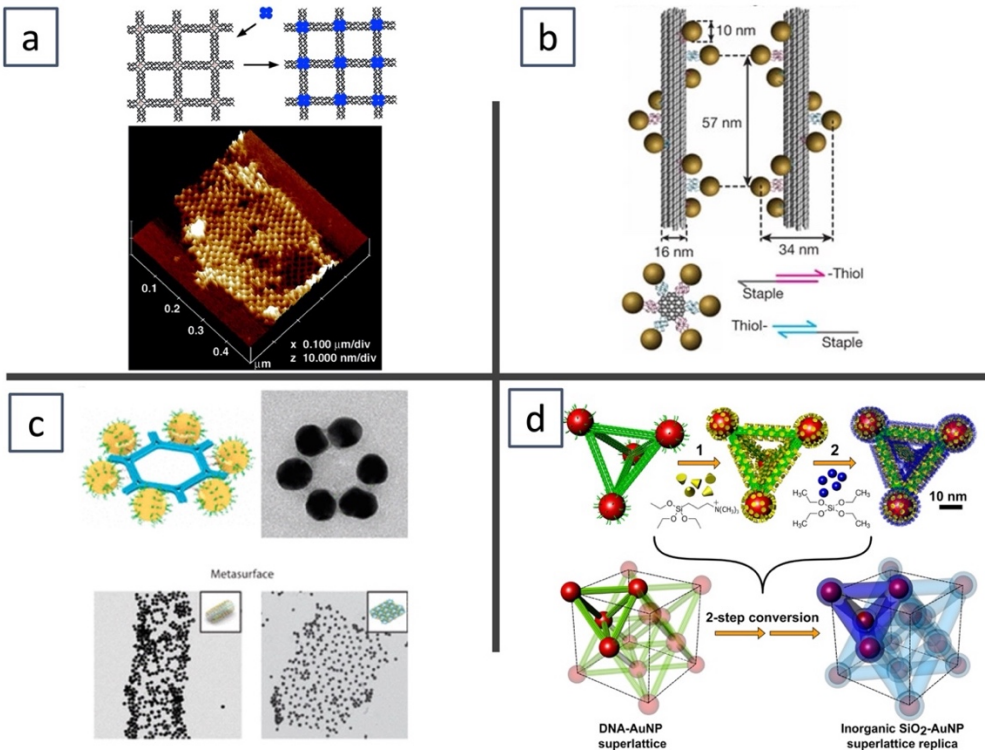

Figure 4.DNA assisted self-assembly of nanoparticles and biomarkers. a)DNA assisted self-assembly of ***proteins***[1] *b, c)DNA templated self-assembly of gold nanoparticles in 2D*[2, 3]*. d)programmable assembly of gold nanoparticles in 3D superlattices.*[5]

The technique of designing DNA origami structures can be accomplished using the program caDNAno. [82] Initially, the intended shape is estimated by simply choosing the scaffold route. Since the vast majority of scaffold strands now consist of circular single-stranded oligoes, the scaffold has to be linked together to form one continuous circular strand. Next, a DNA staple with typically 15 to 50 bases must be manually created from the staples. To sufficiently prevent aggregation caused by blunt ends stacking, the scaffold loop at the edge is left unfolded. The scaffold loop is a region of the single-stranded DNA molecule that is not involved in binding with any of the staple strands that will fold the DNA into the desired shape. Instead, it acts as a flexible region that allows the DNA origami structure to bend and twist into the desired shape without breaking or losing its stability. Finally, the data, including staple sequences and positions, is exported into an excel file, which can be used to order custom oligonucleotides.

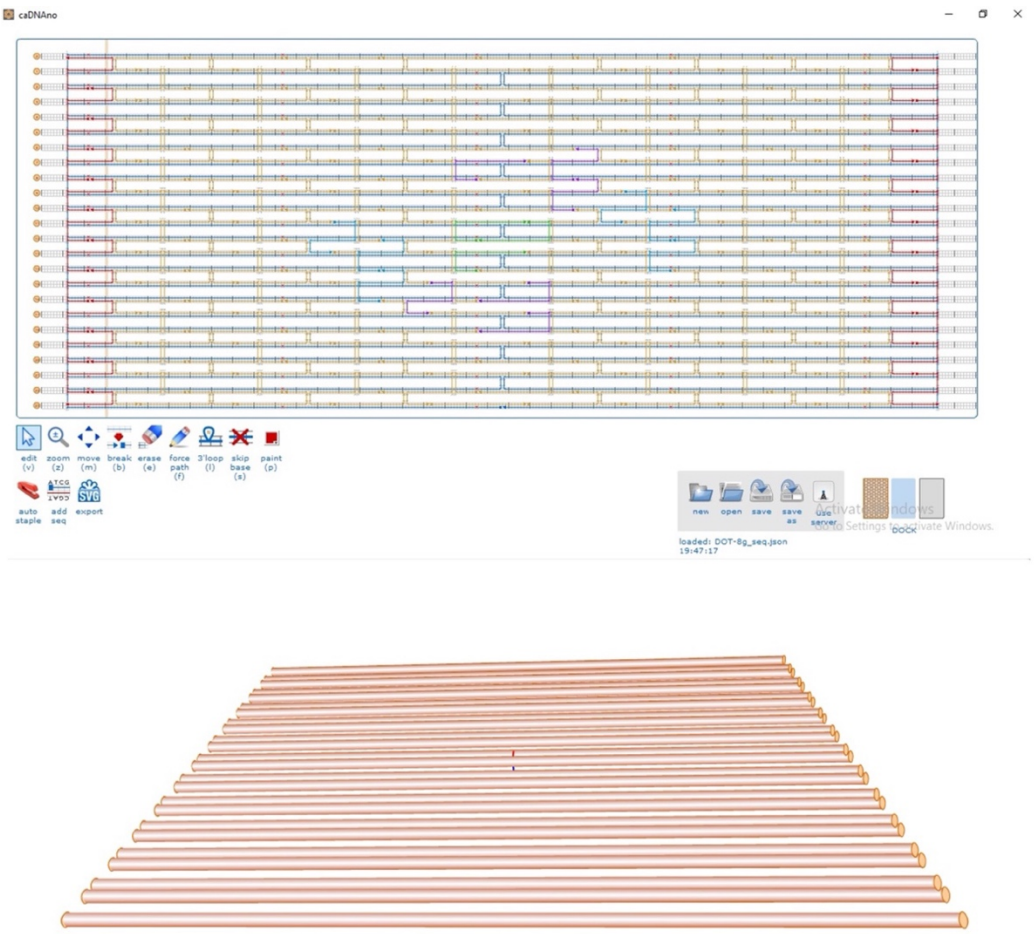

Figure 5. caDNano interface, example of the design of a DNA tile.

1.2 Conclusion and Outlook

Bottom-up methodologies produce nanomaterials from smaller building blocks compared to top-down approaches. These methods also have the potential to create vast quantities of uniform nanostructures simultaneously and can be less expensive. Furthermore, unlike top-down approaches, bottom-up approaches, such as DNA-mediated self-assembly techniques, allow for precise, site-specific, and programable self-assembly of various components. However, in order to deposit these components (nanoparticles) on DNA templates, it is necessary to modify them with DNA ligands, which have complementary sequences for hybridization with strands on the DNA template.

DNA functionalization of 10-30 nm spherical gold nanoparticles is fairly common in the case of gold nanoparticles,[88] but it is difficult to functionalize gold nanoparticles of very small sizes, such as gold nanoclusters, very large nanoparticles (>50nm), or other shapes, such as gold nanorods. For magnetic nanoparticles, it is difficult to produce monodispersed DNA-functionalized nanoparticles due to the magnetic and dipolar interactions between the nanoparticles. For optically active nanoparticles such as quantum dots, surface defects, the types of materials used, and the purity of the precursors all have a significant impact on the optical properties of the nanoparticles, therefore optimum functionalization is required to preserve the optical properties of the nanoparticles. The process of self-assembling nanoparticles needs the alteration of the ligands. Surface imperfections brought on by ligand exchange may potentially alter the optical characteristics of nanoparticles. Low assembly yield or nanoparticle aggregations may also occur as a result of low initial ligand surface coverage or ligand desorption due to low bind energies of these ligands. Therefore, systematic research in the chemistry of ligands and nanoparticle surfaces is necessary to find solutions for these issues. The assembly of nanoparticles can benefit from a better knowledge of the association between a nanoparticle's surface-ligand interaction and the ligand design. In the chapters that follow, some of these problems are analyzed in greater depth, and a few potential solutions are explored.

1.3 References

(1) Yan, H.; Park, S. H.; Finkelstein, G.; Reif, J. H.; LaBean, T. H. DNA-Templated Self-Assembly of Protein Arrays and Highly Conductive Nanowires. *Science* **2003**, *301* (5641), 1882-1884

(2) Wang, P.; Gaitanaros, S.; Lee, S.; Bathe, M.; Shih, W. M.; Ke, Y. Programming Self-Assembly of DNA Origami Honeycomb Two-Dimensional Lattices and Plasmonic Metamaterials. *Journal of the American Chemical Society* **2016**, *138* (24), 7733-7740

(3) Kuzyk, A.; Schreiber, R.; Fan, Z.; Pardatscher, G.; Roller, E.-M.; Högele, A.; Simmel, F. C.; Govorov, A. O.; Liedl, T. DNA-based self-assembly of chiral plasmonic nanostructures with tailored optical response. *Nature* **2012**, *483* (7389), 311-314

(4) Cao, G. W., Y. *Nanostructures and Nanomaterials: Synthesis, Properties,*

and Applications; World Scientific series in nanoscience and nanotechnology (World

Scientific), 2011,

(5) Zhu, C.; Wang, M.; Dong, J.; Zhou, C.; Wang, Q. Modular Assembly of Plasmonic Nanoparticles Assisted by DNA Origami. *Langmuir* **2018**, *34* (49), 14963-14968

(6) Boles, M. A.; Engel, M.; Talapin, D. V. Self-Assembly of Colloidal Nanocrystals: From Intricate Structures to Functional Materials. *Chemical Reviews* **2016**, *116* (18), 11220-11289

(7) Jones, M. R.; Seeman, N. C.; Mirkin, C. A. Programmable materials and the nature of the DNA bond. *Science* **2015**, *347* (6224), 1260901

(8) Walker, D. A.; Leitsch Ek Fau - Nap, R. J.; Nap Rj Fau - Szleifer, I.; Szleifer I Fau - Grzybowski, B. A.; Grzybowski, B. A. Geometric curvature controls the chemical patchiness and self-assembly of nanoparticles. (1748-3395 (Electronic)),

(9) Mirkin, C. A.; Letsinger, R. L.; Mucic, R. C.; Storhoff, J. J. A DNA-based method for rationally assembling nanoparticles into macroscopic materials. *Nature* **1996**, *382* (6592), 607-609

(10) Pal, S.; Deng, Z.; Ding, B.; Yan, H.; Liu, Y. DNA-Origami-Directed Self-Assembly of Discrete Silver-Nanoparticle Architectures. *Angewandte Chemie International Edition* **2010**, *49* (15), 2700-2704

(11) Loretan, M.; Domljanovic, I.; Lakatos, M.; Rüegg, C.; Acuna, G. P. DNA Origami as Emerging Technology for the Engineering of Fluorescent and Plasmonic-Based Biosensors. In *Materials*, 2020; Vol. 13.

(12) Hübner, K.; Pilo-Pais, M.; Selbach, F.; Liedl, T.; Tinnefeld, P.; Stefani, F. D.; Acuna, G. P. Directing Single-Molecule Emission with DNA Origami-Assembled Optical Antennas. *Nano Letters* **2019**, *19* (9), 6629-6634

(13) Sun, L.; Lin, H.; Kohlstedt, K. L.; Schatz, G. C.; Mirkin, C. A. Design principles for photonic crystals based on plasmonic nanoparticle superlattices. *Proceedings of the National Academy of Sciences* **2018**, *115* (28), 7242-7247

(14) Park, D. J.; Ku, J. C.; Sun, L.; Lethiec, C. M.; Stern, N. P.; Schatz, G. C.; Mirkin, C. A. Directional emission from dye-functionalized plasmonic DNA superlattice microcavities. *Proceedings of the National Academy of Sciences* **2017**, *114* (3), 457-461

(15) Ross, M. B.; Ku, J. C.; Vaccarezza, V. M.; Schatz, G. C.; Mirkin, C. A. Nanoscale form dictates mesoscale function in plasmonic DNA-nanoparticle superlattices. (1748-3395 (Electronic)),

(16) Park, D. J.; Zhang, C.; Ku, J. C.; Zhou, Y.; Schatz, G. C.; Mirkin, C. A. Plasmonic photonic crystals realized through DNA-programmable assembly. (1091-6490 (Electronic)),

(17) Park, S.; Urbach, Z.; Brisbois, C.; Parker, K.; Partridge, B.; Oh, T.; Dravid, V.; de la Cruz, M.; Mirkin, C. DNA- and Field-Mediated Assembly of Magnetic Nanoparticles into High-Aspect Ratio Crystals. *Advanced Materials* **2020**, *32* (4),

(18) Park, S. J.; Lazarides, A. A.; Storhoff, J. J.; Pesce, L.; Mirkin, C. A. The structural characterization of oligonucleotide-modified gold nanoparticle networks formed by DNA hybridization. *Journal of Physical Chemistry B* **2004**, *108* (33), 12375-12380

(19) Mitchell, G. P.; Mirkin, C. A.; Letsinger, R. L. Programmed assembly of DNA functionalized quantum dots. *Journal of the American Chemical Society* **1999**, *121* (35), 8122-8123

(20) Ulman, A. Formation and Structure of Self-Assembled Monolayers. *Chemical Reviews* **1996**, *96* (4), 1533-1554

(21) Liu, B.; Liu, J. Methods for preparing DNA-functionalized gold nanoparticles, a key reagent of bioanalytical chemistry. *Analytical Methods* **2017**, *9* (18), 2633-2643

(22) Hurst, S. J.; Lytton-Jean, A. K. R.; Mirkin, C. A. Maximizing DNA Loading on a Range of Gold Nanoparticle Sizes. *Analytical Chemistry* **2006**, *78* (24), 8313-8318

(23) Cutler, J. I.; Auyeung, E.; Mirkin, C. A. Spherical Nucleic Acids. *Journal of the American Chemical Society* **2012**, *134* (3), 1376-1391

(24) Storhoff, J. J.; Elghanian, R.; Mucic, R. C.; Mirkin, C. A.; Letsinger, R. L. One-Pot Colorimetric Differentiation of Polynucleotides with Single Base Imperfections Using Gold Nanoparticle Probes. *Journal of the American Chemical Society* **1998**, *120* (9), 1959-1964

(25) Storhoff, J. J.; Elghanian, R.; Mirkin, C. A.; Letsinger, R. L. Sequence-Dependent Stability of DNA-Modified Gold Nanoparticles. *Langmuir* **2002**, *18* (17), 6666-6670

(26) Kimura-Suda, H.; Petrovykh, D. Y.; Tarlov, M. J.; Whitman, L. J. Base-Dependent Competitive Adsorption of Single-Stranded DNA on Gold. *Journal of the American Chemical Society* **2003**, *125* (30), 9014-9015

(27) Liu, J. DNA-stabilized, fluorescent, metal nanoclusters for biosensor development. *TrAC Trends in Analytical Chemistry* **2014**, *58*, 99-111

(28) Huang, D.; Freeley, M.; Palma, M. DNA-Mediated Patterning of Single Quantum Dot Nanoarrays: A Reusable Platform for Single-Molecule Control. *Scientific Reports* **2017**, *7* (1), 45591

(29) Su, S.; Fan, J.; Xue, B.; Yuwen, L.; Liu, X.; Pan, D.; Fan, C.; Wang, L. DNA-Conjugated Quantum Dot Nanoprobe for High-Sensitivity Fluorescent Detection of DNA and micro-RNA. *ACS Applied Materials & Interfaces* **2014**, *6* (2), 1152-1157

(30) Boeneman, K.; Prasuhn, D. E.; Blanco-Canosa, J. B.; Dawson, P. E.; Melinger, J. S.; Ancona, M.; Stewart, M. H.; Susumu, K.; Huston, A.; Medintz, I. L. Self-Assembled Quantum Dot-Sensitized Multivalent DNA Photonic Wires. *Journal of the American Chemical Society* **2010**, *132* (51), 18177-18190

(31) Dyadyusha, L.; Yin, H.; Jaiswal, S.; Brown, T.; Baumberg, J. J.; Booy, F. P.; Melvin, T. Quenching of CdSe quantum dot emission, a new approach for biosensing. *Chemical Communications* **2005**, (25), 3201-3203

(32) Pathak, S.; Choi Sk Fau - Arnheim, N.; Arnheim N Fau - Thompson, M. E.; Thompson, M. E. Hydroxylated quantum dots as luminescent probes for in situ hybridization. (0002-7863 (Print)),

(33) Tikhomirov, G.; Hoogland, S.; Lee, P. E.; Fischer, A.; Sargent, E. H.; Kelley, S. O. DNA-based programming of quantum dot valency, self-assembly and luminescence. *Nature Nanotechnology* **2011**, *6* (8), 485-490

(34) Smith, M.; McKeague, M.; DeRosa, M. C. Synthesis, transfer, and characterization of core-shell gold-coated magnetic nanoparticles. *MethodsX* **2019**, *6*, 333-354

(35) Tay, Z. A.-O.; Savliwala, S. A.-O.; Hensley, D. W.; Fung, K. A.-O.; Colson, C.; Fellows, B. A.-O.; Zhou, X.; Huynh, Q. A.-O.; Lu, Y.; Zheng, B.; et al. Superferromagnetic Nanoparticles Enable Order-of-Magnitude Resolution & Sensitivity Gain in Magnetic Particle Imaging. (2366-9608 (Electronic)),

(36) Xie, J.; Peng, S.; Brower, N.; Pourmand, N.; Wang, S. X.; Sun, S. One-pot synthesis of monodisperse iron oxide nanoparticles for potential biomedical applications. **2006**, *78* (5), 1003-1014

(37) Sapsford, K. E.; Algar, W. R.; Berti, L.; Gemmill, K. B.; Casey, B. J.; Oh, E.; Stewart, M. H.; Medintz, I. L. Functionalizing Nanoparticles with Biological Molecules: Developing Chemistries that Facilitate Nanotechnology. *Chemical Reviews* **2013**, *113* (3), 1904-2074

(38) Teja, A. S.; Koh, P.-Y. Synthesis, properties, and applications of magnetic iron oxide nanoparticles. *Progress in Crystal Growth and Characterization of Materials* **2009**, *55* (1), 22-45

(39) Akbarzadeh, A.; Samiei, M.; Davaran, S. Magnetic nanoparticles: preparation, physical properties, and applications in biomedicine. *Nanoscale Research Letters* **2012**, *7* (1), 144

(40) Martinez-Boubeta, C.; Simeonidis, K.; Makridis, A.; Angelakeris, M.; Iglesias, O.; Guardia, P.; Cabot, A.; Yedra, L.; Estradé, S.; Peiró, F.; et al. Learning from Nature to

Improve the Heat Generation of Iron-Oxide Nanoparticles for Magnetic Hyperthermia Applications. *Scientific Reports* **2013**, *3* (1), 1652

(41) Freitas, M.; Sá Couto, M.; Barroso, M. F.; Pereira, C.; de-los-Santos-Álvarez, N.; Miranda-Ordieres, A. J.; Lobo-Castañón, M. J.; Delerue-Matos, C. Highly Monodisperse Fe3O4@Au Superparamagnetic Nanoparticles as Reproducible Platform for Genosensing Genetically Modified Organisms. *ACS Sensors* **2016**, *1* (8), 1044-1053

(42) Bruce, I. J.; Sen, T. Surface Modification of Magnetic Nanoparticles with Alkoxysilanes and Their Application in Magnetic Bioseparations. *Langmuir* **2005**, *21* (15), 7029-7035

(43) Meyer, T. A.; Zhang, C.; Bao, G.; Ke, Y. Programmable Assembly of Iron Oxide Nanoparticles Using DNA Origami. *Nano Letters* **2020**, *20* (4), 2799-2805

(44) Damavandi, F.; Wang, W.; Shen, W.-Z.; Cetinel, S.; Jordan, T.; Jovel, J.; Montemagno, C.; Wong, G. K.-S. Enrichment of low abundance DNA/RNA by oligonucleotide-clicked iron oxide nanoparticles. *Scientific Reports* **2021**, *11* (1), 13053

(45) Hu, X.; Kim, C.-J.; Albert, S. K.; Park, S.-J. DNA-Grafted Poly(acrylic acid) for One-Step DNA Functionalization of Iron Oxide Nanoparticles. *Langmuir* **2018**, *34* (47), 14342-14346

(46) Banerjee, A. A.-O.; Pons, T. A.-O.; Lequeux, N. A.-O.; Dubertret, B. A.-O. Quantum dots-DNA bioconjugates: synthesis to applications. (2042-8898 (Print)),

(47) Li, F.; Zhang, H.; Dever, B.; Li, X.-F.; Le, X. C. Thermal Stability of DNA Functionalized Gold Nanoparticles. *Bioconjugate Chem.* **2013**, *24* (11), 1790-1797

(48) Whitesides, G. M.; Boncheva, M. Beyond molecules: Self-assembly of mesoscopic and macroscopic components. *Proceedings of the National Academy of Sciences* **2002**, *99* (8), 4769-4774

(49) Boles, M. A.; Ling, D.; Hyeon, T.; Talapin, D. V. The surface science of nanocrystals. (1476-4660 (Electronic)),

(50) Grzelczak, M.; Vermant, J.; Furst, E. M.; Liz-Marzán, L. M. Directed Self-Assembly of Nanoparticles. *ACS Nano* **2010**, *4* (7), 3591-3605

(51) Nie, Z.; Petukhova A Fau - Kumacheva, E.; Kumacheva, E. Properties and emerging applications of self-assembled structures made from inorganic nanoparticles. (1748-3395 (Electronic)),

(52) Macfarlane, R. J.; Lee, B.; Hill, H. D.; Senesi, A. J.; Seifert, S.; Mirkin, C. A. Assembly and organization processes in DNA-directed colloidal crystallization. *Proceedings of the National Academy of Sciences* **2009**, *106* (26), 10493-10498

(53) Julin, S.; Nummelin, S.; Kostiainen, M. A.; Linko, V. DNA nanostructure-directed assembly of metal nanoparticle superlattices. *Journal of Nanoparticle Research* **2018**, *20* (5), 119

(54) Auyeung, E.; Macfarlane, R. J.; Choi, C. H. J.; Cutler, J. I.; Mirkin, C. A. Transitioning DNA-Engineered Nanoparticle Superlattices from Solution to the Solid State. *Advanced Materials* **2012**, *24* (38), 5181-5186

(55) Nickel, B.; Liedl, T. DNA-linked superlattices get into shape. (1476-4660 (Electronic)),

(56) Chou, L. Y. T.; Song, F.; Chan, W. C. W. Engineering the Structure and Properties of DNA-Nanoparticle Superstructures Using Polyvalent Counterions. *Journal of the American Chemical Society* **2016**, *138* (13), 4565-4572

(57) Lermusiaux, L.; Funston, A. M. Plasmonic isomers via DNA-based self-assembly of gold nanoparticles. *Nanoscale* **2018**, *10* (41), 19557-19567

(58) Coughlin, E. E.; Hu, J.; Lee, A.; Odom, T. W. Light-Mediated Directed Placement of Different DNA Sequences on Single Gold Nanoparticles. *Journal of the American Chemical Society* **2021**, *143* (10), 3671-3676

(59) Macfarlane Robert, J.; Lee, B.; Jones Matthew, R.; Harris, N.; Schatz George, C.; Mirkin Chad, A. Nanoparticle Superlattice Engineering with DNA. *Science* **2011**, *334* (6053), 204-208

(60) Sharma, J.; Chhabra, R.; Cheng, A.; Brownell, J.; Liu, Y.; Yan, H. Control of Self-Assembly of DNA Tubules Through Integration of Gold Nanoparticles. *Science* **2009**, *323* (5910), 112-116

(61) Douglas, S. M.; Dietz H Fau - Liedl, T.; Liedl T Fau - Högberg, B.; Högberg B Fau - Graf, F.; Graf F Fau - Shih, W. M.; Shih, W. M. Self-assembly of DNA into nanoscale three-dimensional shapes. (1476-4687 (Electronic)),

(62) Sharma, J.; Ke, Y.; Lin, C.; Chhabra, R.; Wang, Q.; Nangreave, J.; Liu, Y.; Yan, H. DNA-tile-directed self-assembly of quantum dots into two-dimensional nanopatterns. *Angew Chem Int Ed Engl* **2008**, *47* (28), 5157-5159

(63) Wang, R.; Nuckolls, C.; Wind, S. J. Assembly of Heterogeneous Functional Nanomaterials on DNA Origami Scaffolds. *Angewandte Chemie International Edition* **2012**, *51* (45), 11325-11327

(64) Seeman, N. C. DNA in a material world. *Nature* **2003**, *421* (6921), 427-431

(65) Seeman, N. C. Nucleic acid junctions and lattices. (0022-5193 (Print)),

(66) Seeman, N. C. An overview of structural DNA nanotechnology. (1073-6085 (Print)),

(67) Seeman, N. C. At the crossroads of chemistry, biology, and materials: structural DNA nanotechnology. (1074-5521 (Print)),

(68) Seeman, N. C. DNA engineering and its application to nanotechnology. (0167-7799 (Print)),

(69) Winfree, E.; Liu F Fau - Wenzler, L. A.; Wenzler La Fau - Seeman, N. C.; Seeman, N. C. Design and self-assembly of two-dimensional DNA crystals. (0028-0836 (Print)),

(70) He, Y.; Chen Y Fau - Liu, H.; Liu H Fau - Ribbe, A. E.; Ribbe Ae Fau - Mao, C.; Mao, C. Self-assembly of hexagonal DNA two-dimensional (2D) arrays. (0002-7863 (Print)),

(71) Dietz, H.; Douglas Sm Fau - Shih, W. M.; Shih, W. M. Folding DNA into twisted and curved nanoscale shapes. (1095-9203 (Electronic)),

(72) Rothemund, P. W. K. Folding DNA to create nanoscale shapes and patterns. *Nature* **2006**, *440* (7082), 297-302

(73) Ke, Y. G.; Ong, L. L.; Sun, W.; Song, J.; Dong, M. D.; Shih, W. M.; Yin, P. DNA brick crystals with prescribed depths. *Nature Chemistry* **2014**, *6* (11), 994-1002

(74) Cox, A. J.; Bengtson, H. N.; Rohde, K. H.; Kolpashchikov, D. M. DNA nanotechnology for nucleic acid analysis: multifunctional molecular DNA machine for RNA detection. *Chemical Communications* **2016**, *52* (99), 14318-14321

(75) Sharma, J.; Chhabra R Fau - Cheng, A.; Cheng A Fau - Brownell, J.; Brownell J Fau - Liu, Y.; Liu Y Fau - Yan, H.; Yan, H. Control of self-assembly of DNA tubules through integration of gold nanoparticles. (1095-9203 (Electronic)),

(76) Zheng, J.; Constantinou Pe Fau - Micheel, C.; Micheel C Fau - Alivisatos, A. P.; Alivisatos Ap Fau - Kiehl, R. A.; Kiehl Ra Fau - Seeman, N. C.; Seeman, N. C. Two-dimensional nanoparticle arrays show the organizational power of robust DNA motifs. (1530-6984 (Print)),

(77) Jungmann, R.; Scheible M Fau - Kuzyk, A.; Kuzyk A Fau - Pardatscher, G.; Pardatscher G Fau - Castro, C. E.; Castro Ce Fau - Simmel, F. C.; Simmel, F. C. DNA origami-based nanoribbons: assembly, length distribution, and twist. (1361-6528 (Electronic)),

(78) Woo, S.; Rothemund, P. W. Programmable molecular recognition based on the geometry of DNA nanostructures. (1755-4349 (Electronic)),

(79) Liu, H.; Fan, C. DNA Origami Nanostructures. In *DNA Nanotechnology: From Structure to Function*, Fan, C. Ed.; Springer Berlin Heidelberg, 2013; pp 207-224.

(80) Wagenbauer, K. F.; Wachauf, C. H.; Dietz, H. Quantifying quality in DNA self-assembly. (2041-1723 (Electronic)),

(81) Shih, W. M.; Quispe Jd Fau - Joyce, G. F.; Joyce, G. F. A 1.7-kilobase single-stranded DNA that folds into a nanoscale octahedron. (1476-4687 (Electronic)),

(82) Douglas, S. M.; Marblestone, A. H.; Teerapittayanon, S.; Vazquez, A.; Church, G. M.; Shih, W. M. Rapid prototyping of 3D DNA-origami shapes with caDNAno. *Nucleic Acids Research* **2009**, *37* (15), 5001-5006

(83) Castro, C. E.; Kilchherr F Fau - Kim, D.-N.; Kim Dn Fau - Shiao, E. L.; Shiao El Fau - Wauer, T.; Wauer T Fau - Wortmann, P.; Wortmann P Fau - Bathe, M.; Bathe M Fau - Dietz, H.; Dietz, H. A primer to scaffolded DNA origami. (1548-7105 (Electronic)),

(84) Martin, T. G.; Dietz, H. Magnesium-free self-assembly of multi-layer DNA objects. *Nature Communications* **2012**, *3* (1), 1103

(85) Stahl, E.; Martin Tg Fau - Praetorius, F.; Praetorius F Fau - Dietz, H.; Dietz, H. Facile and scalable preparation of pure and dense DNA origami solutions. (1521-3773 (Electronic)),

(86) Aghebat Rafat, A.; Pirzer T Fau - Scheible, M. B.; Scheible Mb Fau - Kostina, A.; Kostina A Fau - Simmel, F. C.; Simmel, F. C. Surface-assisted large-scale ordering of DNA origami tiles. (1521-3773 (Electronic)),

(87) Liu, W.; Zhong, H.; Wang, R.; Seeman, N. C. Crystalline Two-Dimensional DNA-Origami Arrays. *Angewandte Chemie International Edition* **2011**, *50* (1), 264-267

(88) Hurst, S.; Lytton-Jean, A.; Mirkin, C. Maximizing DNA loading on a range of gold nanoparticle sizes. *Analytical Chemistry* **2006**, *78* (24), 8313-8318

Chapter 2:

One-Step Ligand Exchange Method to Produce Quantum Dot - DNA Conjugates for DNA Directed Self-Assembly

2.1 Abstract

To address the difficulties of making bright, stable, and small DNA-functionalized quantum dots, we have developed a one-step ligand exchange method. Our method allows QD-DNA conjugates to be produced from commonly available hydrophobic quantum dots. We show that by systematically adjusting reaction conditions such as the ligand-to-nanoparticle ratio, pH, and solvent composition, stable and highly photoluminescent water-soluble DNA-QD conjugates with relatively high ligand loadings can be produced. Moreover, by site-specifically binding these QD-DNA conjugates to a DNA origami template, we demonstrate that these bioconjugates have sufficient colloidal stability for DNA-directed self-assembly. Fluorescence quenching by an adjacent gold nanoparticle was demonstrated. Our simple method can facilitate the assembly of QDs into more complex superlattices and discrete clusters that may enable novel photophysical properties. The schematic of a one-step cap exchange/phase transfer reaction for quantum dot nanoparticles can be seen in the figure below. On the left side, QD nanoparticles capped with Octadecyl Amine are initially dissolved in the organic phase (CH_3Cl/DMSO). By adding the DNA ligands, and in the presence of NaOH as a base and TCEP as a reducing agent, the ligand exchange/phase transfer takes place. On the right, the QD nanoparticles that are capped with DNA move to the aqueous phase (H_2O/DMSO).

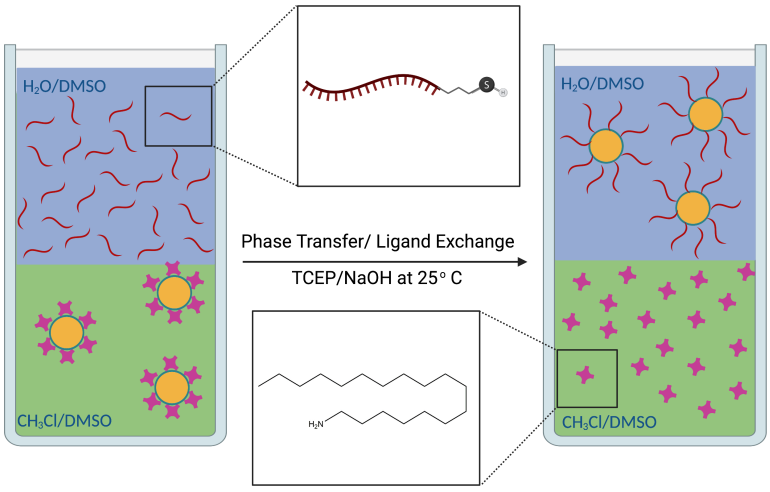

2.2 Introduction

2.2.1 Introduction to Quantum Dots

Colloidal quantum dots are small fluorescent semiconductor nanoparticles (2–20 nm) with size-dependent band gaps due to quantum confinement. As a result of this 3D confinement, quantum dots process unique electronic structures such as wider band gaps compared to bulk materials. The absorption of a photon leads to the excitation of electrons in the valance band into the conduction band. This excitation creates a hole in the valance band. The recombination of the holes and excited electrons triggers the emission of photons, which is called fluorescence. The size of the nanoparticle affects the band gap and, therefore, the wavelength of the emitted light, as is shown by the Brus equation.

(1) $$\Delta E(r) = E_{gap} + \frac{h^2}{8r^2}\left(\frac{1}{m_e^*} + \frac{1}{m_h^*}\right)$$

In equation (1), E is the energy of emitted light; B is the energy of the band gap; h is Planck's constant; r is the radius of the QD; and M and S mass of the excited electron and excited hole, respectively. Based on this equation, as the size of the particle increases, the energy of the emitted light decreases, and therefore the wavelength of the emission is changed. Additionally, the shape and composition of the quantum dot also affect the energy states, making the electronic and optical properties highly tunable based on the size, shape, and composition. The correlation between the optical properties and the size of the quantum dots is shown in Figure 1.

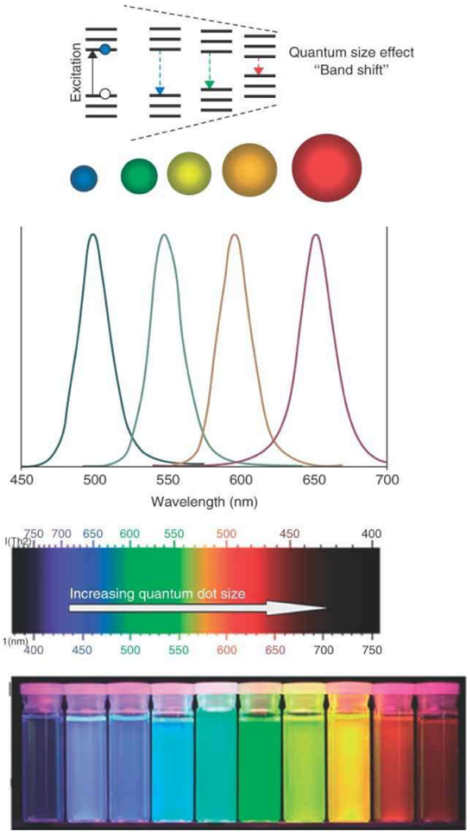

Figure 6. correlation between the size of the quantum dots and their optical properties. [1].

When QDs are assembled in specific geometrical arrangements, they may couple to enable novel collective properties such as super-radiance,[3] energy transfer [4] and have potential applications in data storage,[5] energy harvesting,[6] to information processing.[7,8] Among numerous nanoparticle self-assembly methods, DNA-mediated self-assembly received considerable attention due to its ability to produce some of the most complex structures, including 1D, 2D, and 3D superlattices, as well as geometrically complex clusters. [8–10] To allow the information encoded in the DNA sequence to direct the self-assembly of QDs, these nanoparticles must be conjugated with DNA ligands. QD-DNA conjugates are also bright, photostable, and wavelength-tunable emitters that are appealing for sensing and bioimaging. [11–13]

Even though synthesizing high-quality QDs directly in water is an active area of research, and so far, CdTe, ZnS, CdS, and HgTe QDs have been made in water.[14–18] These methods often suffer from low photoluminescence quantum yield (PLQY) and broad size distribution. Therefore, QD-DNA conjugates are typically produced from hydrophobic ligand-capped QDs that are synthesized through an organometallic route,[19–22] which ensures a narrow size distribution and high photoluminescence quantum yields. However, the conversion of such hydrophobic QDs into ones that are highly stable in aqueous buffers and have the smallest possible sizes remains challenging.

2.2.2 Bioconjugation of Quantum dots with DNA

Making QDs water-soluble is doubtlessly a breakthrough towards their use in biomedical, technical, and biological fields. Unlike organic dyes, QDs have broad absorption and narrow emission spectra that are tunable with their size. To make the QDs soluble in water, many conjugation methods first encapsulate the hydrophobic QDs with a bifunctional coating, such as silica (Figure 2a) [23], amphiphilic polymers [24] (Figure 2b), or phospholipids containing aliphatic chains and polar head groups, and then link DNA to the coating. [25–27] While such coatings improve the stability of QDs in aqueous solutions, the increase in the shell thickness weakens the coupling between QDs and makes them undesirable for enabling emergent functions such as energy transfer. [28–30]

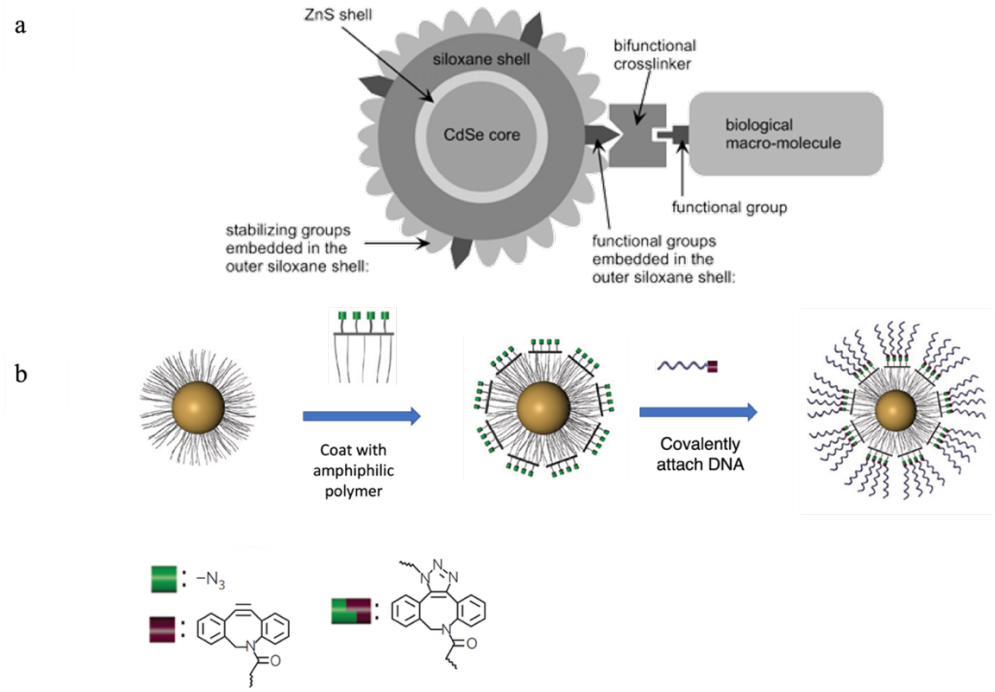

Figure 7. DNA functionalization of QDs with bifunctional coating, such as silica (a)[23]and amphiphilic polymers[24](b).

Alternatively, the hydrophobic ligands can be first replaced with small amphiphilic ligands such as DHLA or MPA that render the QDs water-soluble. [31] Dispersed in an aqueous solution, these QDs can then be conjugated with oligonucleotides through bioconjugation reactions such as amide coupling [18,32–34] (Figure 3a) or ligand exchange with polyhistidine-DNA or thiol-DNA (Figure 3b and Figure 3c). [12,35] While the coupling reactions and two-step cap exchange strategy produce QDs with smaller hydrodynamic sizes, the steric hindrance at the surface of the particles and low colloidal stability often limit the coupling efficiencies, making this method less suitable for many applications that require dense packing of DNA ligands, such as DNA-mediated self-assembly of superlattices[36] and DNA origami-mediated self-assembly of clusters. [37–40]

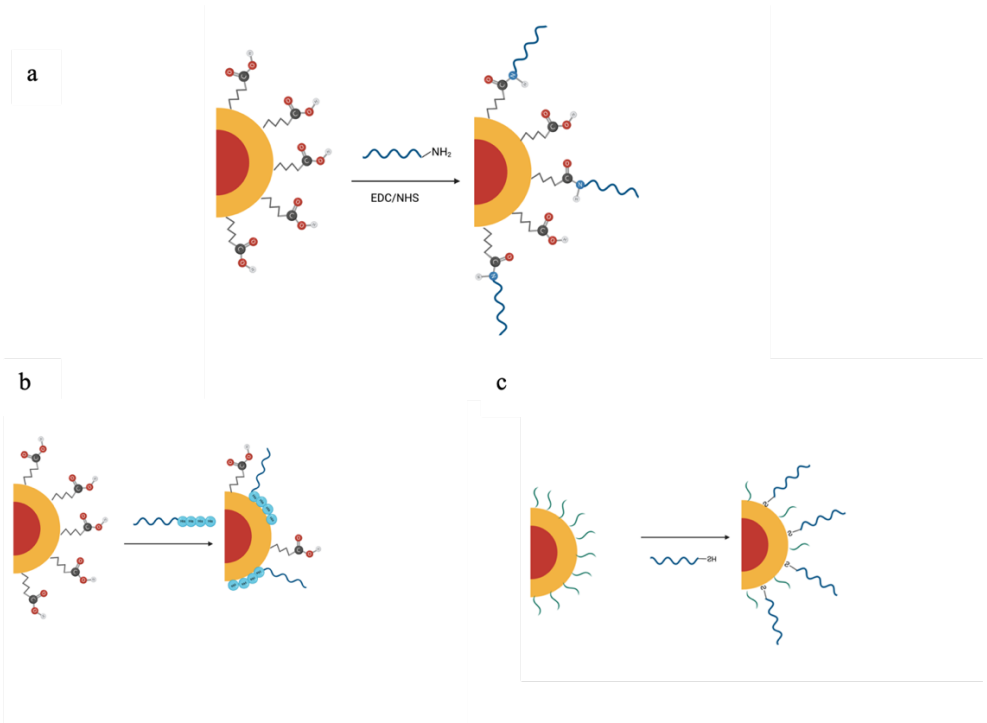

Figure 8.QD functionalization with DNA using bioconjugation reactions such as amide coupling (a) and ligand exchange with polyhistidine modified-DNA (b) or thiol modified-DNA (c).

Lastly, QD-DNA conjugates can be produced by embedding the end part of the DNA ligands in a passivating shell (Figure 4). [37,41,42] While these QD-DNA conjugates have small sizes as well as excellent chemical and photophysical stability, wider adoption of this method is hindered by the requisite expertise in QD synthesis, a broad size distribution, the PL band, as well as reduced crystallinity. [43] Due to the difficulties in forming QD-DNA conjugates that are compact, stable, and have the smallest possible size, the reported successes in DNA-mediated self-assembly of QDs are notably more limited compared to those in DNA-mediated self-assembly of gold nanoparticles [44–47] which are more readily conjugated with DNA ligands [16,48–56] into a large variety of superlattices, [57] as well as discrete clusters. [36, 45]

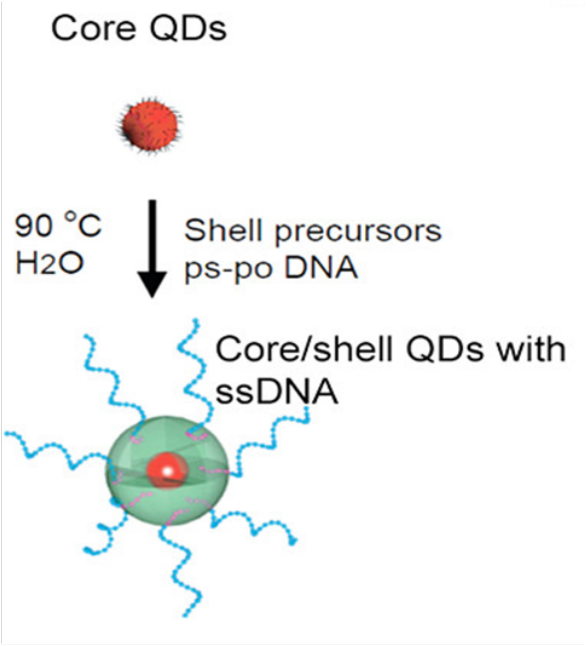

Figure 9. QD-DNA conjugation by embedding the end part of the DNA ligands in a passivating shell. [41]

Here we report a one-pot ligand exchange/phase transfer process that uses hydrophobic QDs to produce QD-DNA conjugates that are compact, bright, and stable in aqueous solutions. We discovered that our ligand exchange process can directly replace the hydrophobic ligands on commercially available QDs with thiol-modified DNA and transfer the QDs into an aqueous phase. These DNA-conjugated QDs are as emissive as their hydrophobic counterparts. We demonstrate that these QD-DNA conjugates, possessing high colloidal stability, can site-specifically bind to DNA origami templates. Fluorescence quenching by an adjacent gold nanoparticle was also demonstrated. Our simple method, which can be readily carried out without expertise in QD synthesis, can facilitate the assembly of QDs into more complex superlattices and discrete clusters that may enable novel photophysical properties.

2.3 Experimental Section

2.3.1 DNA Preparation

The disulfide bonds of an 18-nt (5' CA TGT TCA GCG TAA TTTT/(CH2)3SH 3') modified oligonucleotide (from IDT DNA) were cleaved by mixing 100 mM of oligonucleotides with 100 mM tris(2-carboxyethyl) phosphine (TCEP) in a 1:600 ratio and left at room temperature overnight. The TCEP-reduced 18-nt DNA was purified with a 3K Da Amicon Ultra-0.5 Centrifugal Filter (Millipore Sigma, Burlington, MA, USA) twice at 14000× g for 20 minutes, and the concentration was measured with a Thermo Scientific Nanodrop spectrophotometer. Then the solution mixture was replenished with 1 ml of 100 mM TCEP. It is known that TCEP helps retain the photoluminescence by suppressing the

surface etching of the quantum dots. Then the mixture was diluted with Millipore water to minimize the chance of aggregation.

2.3.2 Phase transfer/ligand exchange

Octadecylamine-capped CdSe/ZnS QDs in a solid form (Sigma Aldrich, Product #: 748080) were first dissolved in chloroform. The concentration was then measured using the extinction coefficient and absorbance. Previously reduced and purified 18-nt DNA (5' CA TGT TCA GCG TAA TTTT/$(CH_2)_3$SH 3') was used for surface functionalization. To find the optimal condition for this reaction, reaction mixtures with DNA/QD molar ratios of 20, 80, 160, 320, 640 were prepared under the following conditions: reduced DNA-TCEP mixture, 50 ml of dimethyl sulfoxide (DMSO), and 100 ml of chloroform were added to each vial, followed by the addition of the QDs (typically 2.44 mM). Due to slow evaporation during the reaction, chloroform was replenished during the phase transfer. A previous study[48] has shown that zinc ions in the solution help to preserve the QD photoluminescence by passivating the electron surface/hole traps. [20, 22] Therefore, 9 ml of 25 mM $Zn(NO_3)_2$ was added to the reaction to retain the photoluminescence. The mixtures were left on the vortex for at least 0.5 hr. before the addition of NaOH. This stepwise addition of NaOH is typically done at 1 hr. intervals and stops when the pH reaches around 9.5-10. The final concentration of NaOH at which this pH is achieved is dependent on the amount of DNA.

2.3.3 Preparation of DNA conjugated gold nanoparticles

The salt-aging method developed by Mirkin et al. [46] was used to conjugate gold nanoparticles with DNA. Thiol-modified oligonucleotides of 18 nt (5'-GT AGT CGC AGA TTA TTTT/$(CH_2)_3$SH 3') were treated with TCEP (600×) overnight to cleave the disulfide bond and purified with a 3KDa Amicon Ultra-0.5 Centrifugal Filter (Millipore Sigma, Burlington, MA, USA) twice at 14000× g for 20 minutes, and the concentration was measured with a NanoDrop™ spectrophotometer. Then the oligonucleotides were mixed with 10 nm AuNPs at a molar ratio of 660:1. After adjusting the final concentration of SDS to 0.01% w/v, a 5 M NaCl solution was added to the mixture to gradually increase the final concentration of NaCl in the mixture to 0.3 M over the course of 3 hrs. The mixture was then purified using 100K Da Amicon Ultra-0.5 Centrifugal Filter 8 times at 14000× g for 5 minutes.

2.3.4 DNA origami formation

The DNA origami tiles used in this study were designed with Cadnano [49] (supporting information) and prepared using a previously published method. [50] M13mp18 DNA (New England Biolabs) in 1× TAE-Mg^{2+} buffer (10 mM Tris base, 1 mM Ethylenediamine Tetra Acetic Acid (EDTA), 14 mM $MgCl_2$) was mixed with a 100-fold excess of short staple strands and thermally annealed from 95 °C to 20 °C in a thermocycler

(BIO-RAD T100) at a rate of -1°C per minute. The folded DNA nanostructures were separated from excess DNA staple strands using a 50K Da Amicon Ultra-0.5 Centrifugal Filter. The filtration was performed at 3500× g for 2 minutes and five times. Each time, the solution was replenished with 1× TAE, and the final concentration of $MgCl_2$ was adjusted to 10 mM.

2.3.5 Self-assembly of nanoparticles on DNA origami

To bind the DNA-conjugated gold nanoparticles and QDs to the DNA origami tile, we used a 2-step sequential annealing method. In the first step, the purified tiles were mixed with the prepared QD nanoparticles and were annealed to the tiles at a 2× equimolar concentration in 1× TAE buffer and 12.5 mM $MgCl_2$. The annealing was performed in a thermocycler (Eppendorf) from 41 °C to 20 °C at a rate of 1 °C per minute. In order to remove unbound nanoparticles, two rounds of purification were performed using size exclusion spin columns (gel filtration purification method in SI). In the second step, purified AuNP-DNA conjugates were annealed to the previously made QD-tiles at a 2× equimolar concentration in 1× TAE buffer and 12.5 mM $MgCl_2$. The annealing was performed in a thermocycler (BIO-RAD T100) starting at 41°C and slowly decreasing to 20 °C at a rate of -1 °C per minute. The nanoparticle-DNA origami conjugates were then purified again with size exclusion spin columns twice before TEM imaging.

2.3.6 Transmission electron microscopy

Transmission electron microscopy (TEM) imaging of the DNA origami and QD–DNA origami assemblies was carried out using a Talos F200C G2 transmission electron microscope operating at 200 kV in the UC Merced Imaging and Microscopy Facility. Typically, 4-5 ml of the sample was deposited onto an Argon plasma-treated formvar/carbon-coated (copper mesh) grid (Ted Pella, Inc., Redding, CA, USA; prod no. 01753-f) for up to 5 min. The excess liquid was then blotted off, and the grid was washed and stained using a 2% aqueous uranyl formate solution and let dry overnight.

2.3.7 pH Measurement

pH measurements were done at room temperature using a microglass pH electrode (Fisher Scientific Accumet combination electrodes (13-620-851) and an Orion Star5 thermoscientific pH meter.

2.3.8 DLS Measurement

All dynamic light scattering (DLS) experiments were performed using ZETASIZER NANO series S90 (Malvern Panalytical). Measurements were done using a

microvolume quartz cuvette (50 μL) using 632.8 nm laser, with 90° scattering angle at room temperature.

2.3.9 Spectroscopic characterization

Concentrations of DNA origami, thiol-modified DNA, unfunctionalized, and functionalized AuNP were determined using a NanoDropTM ND-1000 spectrophotometer (Thermo Fisher Scientific). UV-Vis spectra of unfunctionalized QDs were collected using a Perkin-Elmer Lambda 35 UV/Vis spectrophotometer with a 100 μL quartz cuvette. Fluorescence spectroscopy measurements were done using a HORIBA Instruments Inc. (FL-1000) spectrometer equipped with a thermoelectrically cooled BIUV Synapse CCD detector. Although the slit width and the integration time were varied to optimize the signals, identical slit widths and integration times were used for the same set of spectra. The fluorescence intensity of functionalized QD was measured using a 50 μL Quartz 701MF sub-micro black fluorometer cuvette (Fireflysci), and the QD-Origami and QD-Au-Origami samples were run using a HORIBA Microsense (1-5 μL cuvette).

2.3.10 Agarose gel electrophoresis

For DNA-functionalized nanoparticles, 0.5% agarose gels were prepared with 0.5× TBE buffer and were run for 40 minutes with 0.5× TBE buffer at 65 volts. For origami tiles and the annealed products, 1% agarose gels were prepared with 0.5× TBE/12mM $MgCl_2$. The gels were stained with fluorescent SYBR Green I (10,000×, Invitrogen), and a blue loading dye (6×, NEB) was added to the sample solutions before gel electrophoresis. The running buffer for the tiles was 0.5× TBE with 5 mM $MgCl_2$, and the gels were run for 1 hour at 65 volts.

2.3.11 Quantification of DNA surface ligands

To quantify the number of surface DNA ligands using fluorimetry, we used a Cy5-modified oligonucleotide (Cy5-DNA) that has the same sequence as the unlabeled oligonucleotide. Ligand exchange with the fluorophore modified oligonucleotide was performed at 5 different DNA-to-QD molar ratios: 20, 80, 160, 320, and 640. After the completion of ligand exchange, the solutions were filtered through an ultrafiltration unit with 100 kDa to collect the DNA-functionalized QDs and remove excess unbound ssDNAs. Then the samples were treated with dithiothreitol (DTT) overnight and incubated at 40 °C to remove the ligands from the surface of the particles. The solutions were then spun down at 14000 × g to precipitate the QDs at the bottom of the test tube, and the supernatants were used for fluorimetry quantification.

The molar concentrations of the Cy5-DNA in the supernatants were calculated from the fluorescence intensity maxima at 560 nm and a standard linear calibration curve, which was obtained with known concentrations of Cy5-DNA in the same buffer. The DNA

loading, *i.e.*, the average number of ssDNA strands per QD, was obtained by dividing the measured concentration of fluorescent oligonucleotides by the concentration of the QDs.

2.3.12 Purification of nanoparticle-DNA origami conjugates with gel filtration method

The nanoparticle-DNA origami conjugates were purified using a previously reported size-exclusion spin-column-based method [1] with slight modifications. In short, the size exclusion Sepharose CL-4B resins (Sigma-Aldrich) were buffer exchanged by repetitive resuspension or pelleting in 0.5× TAE, 4mM $MgCl_2$ six times (200 µL of crude resin was diluted to 1000 µL with 0.5× TAE and 4mM $MgCl_2$ and spun at 800*g* for 3 min) and the resin was adjusted to a 50% v/v slurry. The resins were then loaded into empty spin columns (Thermo Scientific) and spun twice to fill the tube with the resin up to 80% volume. Each time, the excess buffer in the resin was removed by spinning the columns at 15 °C at 800*g* for 1 min. The crude nanoparticle-origami tile mixture was then subsequently passed through two spin columns (spun at 800 *g* for 3 min).

2.3.13 Atomic Force microscopy imaging

The DNA origami structures with nanoparticles were deposited onto a mica substrate in the presence of 5 mM $NiAc_2$. All AFM images were collected in an imaging buffer containing 1X Tris-acetate-EDTA (TAE) buffer and 5 mM $NiAc_2$ at room temperature. The AFM probes (Model SNL-10, Bruker Nano Inc., Santa Barbara, CA, U.S.A.) with a nominal spring constant of 0.35 (tip A) or 0.24 (tip C) N/m were used for intermittent contact mode imaging with an NTEGRA AFM (NT-MDT America, Tempe, AZ, U.S.A.). All images were collected using the Nova software (version 1.1.0.1903) at a scan rate of 0.7–1.3 Hz, a driving frequency of 13–15 kHz, and a driving amplitude of 30–50 nm.

2.3.14 Synthesis of dithiol-modified DNA

The synthesis of dithiol-modified DNA was done in a two-step reaction: in the first step, the NHS ester of lipoic acid was synthesized and purified with recrystallization, and in the second step, the activated lipoic acid ester was reacted with amino-modified DNA. The method was adapted from Liu et al[76], with slight modifications.

2.3.15 Surface functionalization of Quantum dots with bidentate dithiol-modified DNA

Functionalizing quantum dots (QDs) with dithiol DNA could be a more effective method than functionalizing with monothiol DNA for several reasons. Firstly, dithiol DNA has two thiol groups per molecule, while monothiol DNA only has one. Thiol groups can

form strong bonds with the surface of QDs, allowing the DNA to anchor more firmly to the QD surface. Secondly, dithiol DNA can form stronger and more stable bonds with the QD surface than monothiol DNA, which can result in more complete functionalization of the QD surface and fewer unbound or unfunctionalized QDs. The formation of two thiol bonds between the dithiol DNA and the QD surface can increase the stability of the functionalized QDs, making them less likely to degrade or detach from the surface over time. Furthermore, dithiol DNA is less susceptible to oxidation than monothiol DNA, which can cause the thiol groups to lose their ability to bind to the QD surface, leading to a decrease in the stability and functionality of the QD-DNA conjugate.

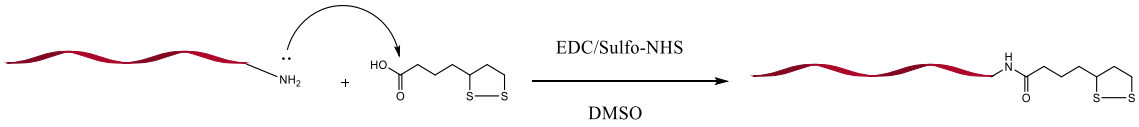

Figure 10.synthesis of the dithiol-modified DNA mechanism.

2.3.16 Synthesis of lipoic acid sulfo-NHS ester (activation)

First, 2.6 mg of lipoic acid was dissolved in 2.3 ml of DMSO. Then, a solution of 10.3 mg of sulfo-NHS in 85% DMSO and 15% H2O was prepared. Next, 4.3mg of EDC was added to the sulfoNHS solution. Finally, 220 µL of the sulfoNHS/EDC solution and 230 µL of the lipoic acid solution were combined and stirred for one hour at 30°C. It is important to maintain the pH of the reaction at around 5 during the reaction.

2.3.17 Dithiol modified DNA (conjugation) purification and Characterization

The sulfo-NHS ester of lipoic acid was added in excess to (4.98 nmol) amine modified oligonucleotides at pH ~8. The reaction mixture was kept overnight at room temperature. The reaction mixture was first diluted with 14 ml of water and purified using a 15-ml Amicon ultrafiltration unit with 3 kDa MWCO and spun down twice at 10,000×g. Dithiol-modified oligonucleotides were further purified by reverse-phase HPLC (Agilent 1100, Column type C18, Gradient 40 minutes, 5–25% Acetronitrile, Buffer A: TEAA (0.1 M, pH 7), Buffer B: CH3CN). Fractions containing lipoic acid modified oligonucleotides were collected and resuspended in distilled water. The product was further characterized with LC-MS (Thermo Scientific: Q-Exactive Hybrid Quadrupole-Orbitrap coupled with Vanquish UHPLC) at UC Merced BMSF facilities. For the MS, 35 ml of 7.7 mM functionalized DNA and 5 ul of ammonium acetate 200 mM in negative mode were used, and the time of injection was 800 ms.

2.4 Results and Discussion

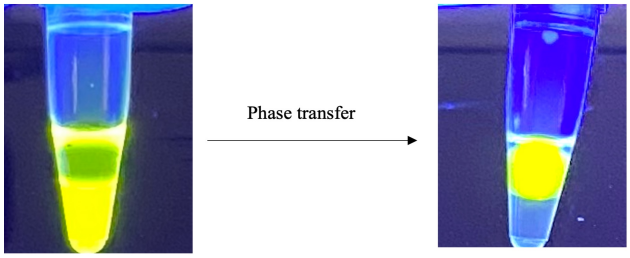

Figure 11.Phase transfer of CdSe/ZnS quantum dots (QDs) from an organic phase (CHCl3 /DMSO,100 µl/50 µl, bottom) to an aqueous phase (79.6 µM of 16 nt. thiol modified DNA, 150 µl, top). Left: 0.398 µM QDs were dissolved in the organic phase. Right: after ligand exchange, the QDs were transferred to the aqueous phase.

The direct conversion of such hydrophobic QDs into ones that are conjugated with hydrophilic DNA molecules is inherently challenging. Figure S1 shows that QDs dissolved in chloroform cannot be transferred to the aqueous phase containing DNA ligands. The hydrophobic QDs reside exclusively in the organic phase and the DNA in the aqueous phase. Therefore, it is difficult for the DNA to displace the ligands on the QDs. Even if a few DNA ligands were attached to the QDs, the DNA ligands would make the QDs unstable in the organic phase. At the same time, the QDs would remain too hydrophobic to be dispersed in the aqueous phase. To address this challenge, DMSO, which could dissolve both DNA and the octadecylamine ligands, was added. We found that in the presence of DMSO, these QDs migrated to the aqueous phase in as little as a few minutes (Figure 1), suggesting that hydrophilic DNAs were attached to the QDs, which made them soluble in the aqueous phase. Although the mechanistic details of the process remain to be fully explored, the likely roles for DMSO include increasing the solubility of DNA ligands in the organic phase and increasing the solubility of the QDs in the aqueous phase. Even if the DNA and hydrophobic QDs remain confined to their respective phases and initial ligand exchange of QDs takes place exclusively at the interface between the two phases, once an octadecylamine-capped QD is conjugated with one or a few DNA ligands, it could have sufficient hydrophilic characteristics to migrate to the aqueous phase, which contains DMSO that stabilizes the amphiphilic QD. Once such QDs are in the aqueous phase, ligand exchange would accelerate. With the initial success in ligand exchange, we studied how the DNA/QD molar ratio and addition–of a strong base affected the size, stability, and photoluminescence of the QD-DNA conjugates.

2.4.1 The roles of NaOH addition

Previous reports suggested that the thiol groups needed to be deprotonated for facile binding to QDs. [51] As TCEP was added to prevent surface etching of the QDs, the pH of the as-prepared aqueous phase was about 3. At this pH, the thiol groups of the ssDNA ligands are protonated, making ligand exchange challenging. To promote the conjugation of thiol-modified oligonucleotides to the QDs, we added 200 mM NaOH to the aqueous phase in a dropwise fashion to increase the pH to 9–10, which is close to the pk_a of thiol-

modified DNA. The effect of base addition was monitored with dynamic light scattering and fluorescence spectroscopy. Figure 2 shows that when ligand exchange was carried out at pH 5, the hydrodynamic sizes were in the range of hundreds of nanometers for both [DNA]/[QD] molar ratios, 320 and 640, suggesting significant agglomeration of these QDs. As more NaOH was added and the pH raised, the hydrodynamic sizes declined to tens of nanometers, indicating that the QDs became more dispersed. At higher pH values, more thiol-modified DNAs became deprotonated, and the ligand exchange with octadecyl amine was facilitated, diminishing the aggregation of the QDs. While this trend was observed for both [DNA]/[QD]=320 and [DNA]/[QD]=640 samples, the samples with more DNA showed smaller hydrodynamic sizes, suggesting that the DNA ligands at a higher concentration formed a denser DNA shell around the QDs and reduced aggregation.

Fluorescence spectroscopy was also used to monitor the reaction progression. The fluorescence spectra of samples with different [DNA]/[QD]:160, 320, and 640 were measured at pH ~5, ~7 and ~9. As NaOH was added to the reaction mixture to increase the pH, the fluorescence of these QD-DNA conjugates was enhanced for all three molar ratios (Figure 2c).

Another possible role of the NaOH addition in the ligand exchange reaction is raising the ionic strength. The repulsion between the negatively charged DNA ligands makes it difficult to conjugate DNA to nanoparticles at high surface densities. As the concentration of Na^+ is increased in the solution, the electrostatic repulsion between the nanoparticles becomes stronger, allowing more DNA to bind to the QDs. This role is similar to the role that NaCl played in the salt aging method to functionalize gold nanoparticles with DNA, where the ionic strength is gradually increased to allow more DNA ligands to bind.

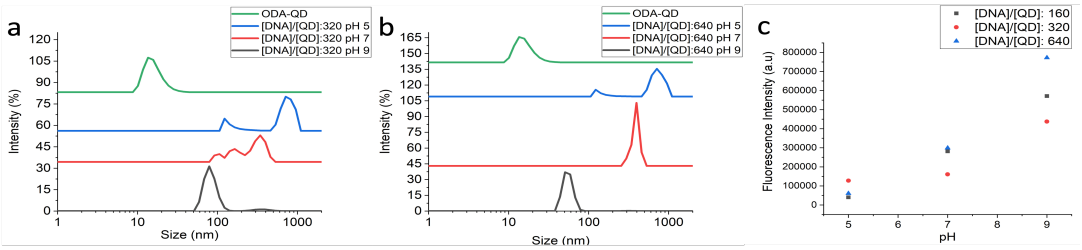

Figure 12. Size distributions of octadecylamine-QDs as well as QD-DNA conjugates that were prepared under different pHs and two, (a)320 and (b) 640. (c) Peak fluorescence intensities (λmax= 560 nm) of the QD-DNA conjugates.

Evidence for this role is that the addition of base should be completed in a stepwise manner over the course of a few hours. Rapid addition of NaOH within a few minutes produced precipitates visible under UV light (Figure S2). While the electrostatic repulsion between DNA needs to be reduced for facile conjugation, QDs in the aqueous phase are stabilized by electrostatic repulsion. When the ionic strength is increased too quickly, the repulsive interactions between QDs that are not covered with enough DNA ligands may be reduced too quickly, leading to irreversible aggregation. Additionally, to understand the roles of pH and ionic strength, NaCl was used instead of NaOH in the ligand exchange process. Figure S6 shows that the resulting QDs were heavily aggregated, suggesting that a higher ionic strength alone is not sufficient to ensure facile ligand exchange with thiolated DNA. A sufficiently high pH is also important for successful conjugation of the hydrophobic QDs with thiolated DNA.

2.4.2 The effect of DNA/QD molar ratio

Figure 3a shows that the QDs were transferred to the aqueous phase at all [DNA]/[QD] ratios tested. Under UV illumination, the bottom organic layer no longer showed fluorescence. Instead, the fluorescence originated exclusively from the top aqueous layer. However, there are visible differences in the aqueous phase. The samples prepared at lower [DNA]/[QD] displayed lower fluorescence and were less uniform. Dynamic light scattering (DLS) was used to measure the hydrodynamic diameter of the QD-DNA conjugates prepared at different [DNA]/[QD] ratios (Figure 3c). The larger hydrodynamic sizes at smaller molar ratios suggest agglomeration at lower DNA concentrations. As the [DNA]/[QD] increased, the hydrodynamic sizes of the resulting QD-DNA conjugates declined. At 640× DNA, the size is 30 nm, which is close to 29 nm, and the calculated physical dimension of the QD-DNA conjugate is based on assuming the average length of a stretched single-stranded DNA ligand to be 10.8nm [52] and the diameter of the QD to be 7 nm. As the scattered intensity scales with the hydrodynamic size to the sixth power, [53] even a small fraction of larger aggregates could dominate the intensity distribution. Therefore, the observed size distribution shows that 640× DNA can form well-dispersed QD-DNA conjugates of the expected dimension with minimal aggregation.

To further assess the efficiency of the phase transfer, the QDs transferred to the aqueous phase were characterized using agarose gel electrophoresis (1% agarose, 1× TAE (40 mM Tris base, 20 mM Acetic acid, 1 mM EDTA, 11 mM $MgCl_2$ buffer; 6.5 V/cm for 1.5 hr). The bands at the bottom correspond to the free DNA ligands, and the bands just below the wells correspond to QDs that are conjugated with DNA (Figure 3b). The lower mobility bands provide additional confirmation of the success of the ligand exchange reaction: unlike the QDs with the neutral hydrophobic ligands, the QDs functionalized with DNA are negatively charged and can migrate out of the wells. The faint band for the 20-cm DNA sample suggests that the ligand exchange was incomplete and that many of the particles were trapped in the interface between the two phases rather than migrating to the aqueous phase.

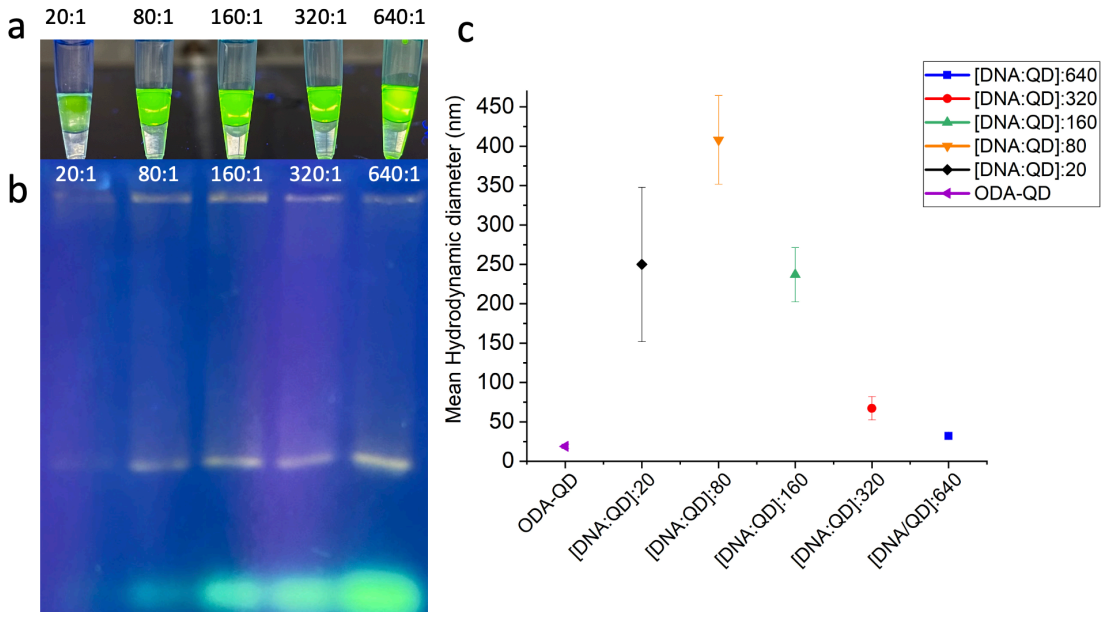

Figure 13. (a)Phase transfer products for different molar ratios of DNA/QD at pH ~9.5-10. The image was captured under 302 nm UV illumination (b) Agarose gel image of QD-DNA conjugates formed at different [DNA]/[QD]. SYBR Green II was used to stain the ssDNA. (c) Hydrodynamic diameter of DNA functionalized QD with 3' end poly T, thiol modified DNA with different [DNA]/[QD]. NaOH was added to all these samples to achieve a final pH of 9.5-10.

We note that the measured hydrodynamic size does not monotonically decline with increasing [DNA]/[QD]. Specifically, the QD sample prepared with 20× DNA shows smaller hydrodynamic sizes compared to QD samples with 80× DNA and 160× DNA (Figure 3c). This anomaly may be understood by considering that at 20× DNA, most of the QDs were trapped at the organic/water interface, and only a small fraction of them successfully migrated to the aqueous phase (Figure 3a). The QDs that migrated to the aqueous phase were less agglomerated than QDs conjugated under 80× and 160× base DNA, which were able to transfer a higher fraction of the aggregated QDs to the aqueous phase. The trends shown in Figures 3b and 3c confirm that as the [DNA]/[QD] ratio increased, more QDs left the two-phase interface and got dispersed in the aqueous solution. The more ligands available for this transition, the less aggregation is obtained (Figure 3c). The mono-dispersity of the QD-DNA conjugates was also confirmed with transmission electron microscopy (TEM) (Figure 4). Our TEM measurements show that the average size of the QD-DNA conjugates, 8.4±1 nm, is virtually identical to that of the original hydrophobic QDs, 7.5±1 nm.

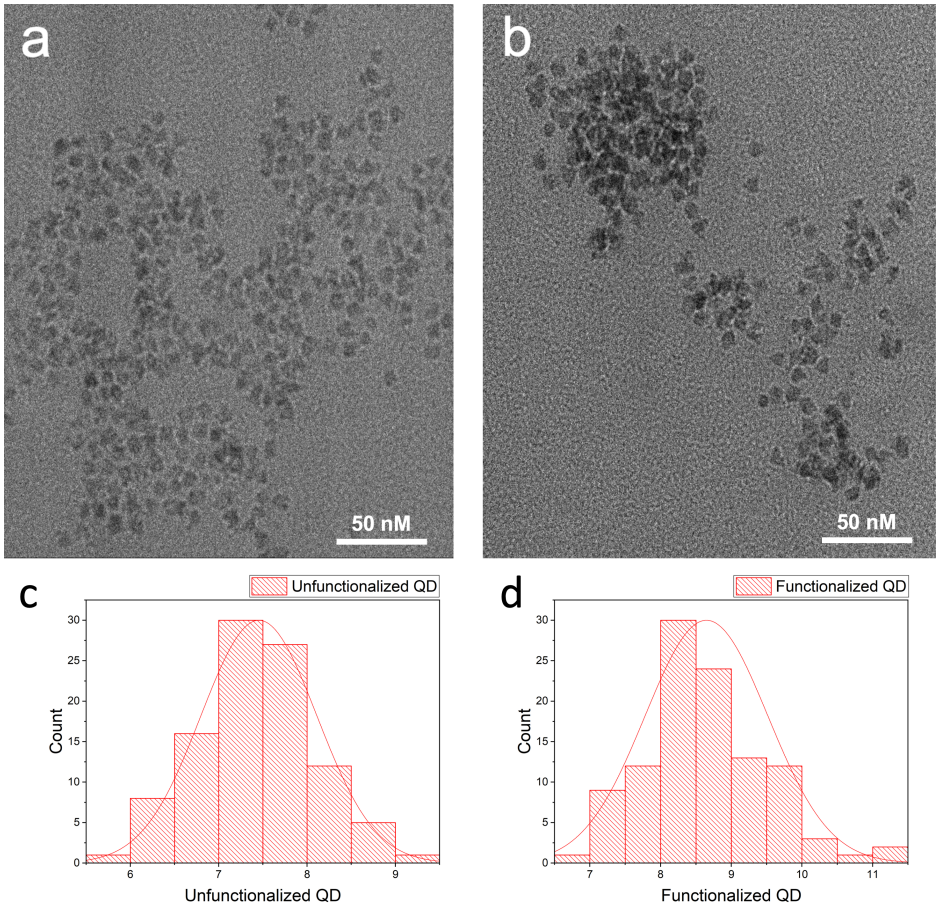

Figure 14. TEM image of (a),1-octadecylamine capped QDs and (c), their size distribution. TEM image of (b) QD-DNA conjugates (prepared with [DNA]/[QD]=640) and (d) their size distribution.

While mono-dispersity is an important criterion for successful QD bioconjugation, the QDs must also retain photoluminescence after conjugation. Therefore, we measured the fluorescence spectra of the QDs conjugated under different conditions (Figure 5). Our measurements show that the higher overall [DNA]/[QD] ratios produce QD-DNA conjugates with higher photoluminescence. The lower photoluminescence with 20 nm DNA and 80 nm DNA is likely a consequence of the incomplete transfer of the nanoparticles to the aqueous phase at these lower DNA concentrations. As many of the QDs were not conjugated with enough DNA ligands to be water-soluble, they were trapped at the interface between two phases. Moreover, many of the QDs that were transferred to the aqueous phase were in aggregated form, further diminishing photoluminescence. The QDs that are conjugated with 640× DNA show the highest photoluminescence. Also, small red shifts in the peak emission up to 2-3 nm were observed in samples with lower DNA/QD ratios, such as 20 and 80 (Figure S5). As DLS is substantially more sensitive to aggregation than fluorescence spectroscopy,[53] the lack of a significant red shift in emission for QDs prepared at low [DNA]/[QD] suggests that a relatively small fraction of QDs aggregated and fluorescence emission was dominated by isolated QDs.

The intensity of photoluminescence of the 640× DNA conjugated QDs is similar to that of octadecylamine-capped-QDs at identical concentration, excitation wavelength, and excitation power, suggesting that they have similar quantum yields (Figure S14). Considering the different refractive indices of the solvents,[54] the quantum yield of the DNA conjugated QDs is about 100±16% of that for octadecylamine-capped QDs. As the nanoparticles are protected by a denser layer of DNA ligands, aggregation and surface etching, which can diminish the emission, are minimized. Our observation is consistent with previous studies showing that when QDs are fully protected with the surface ligands, they are monodispersed, and their photoluminescence is preserved. [17, 36] We also note that the intensity does not strictly increase monotonically with increasing [DNA]/[QD]. In fact, 160× DNA leads to a higher intensity than 320× DNA. While the trend remains to be fully understood, a similar trend was observed in a previous report, which suggests that certain forms of aggregation may lead to higher photoluminescence. [13]

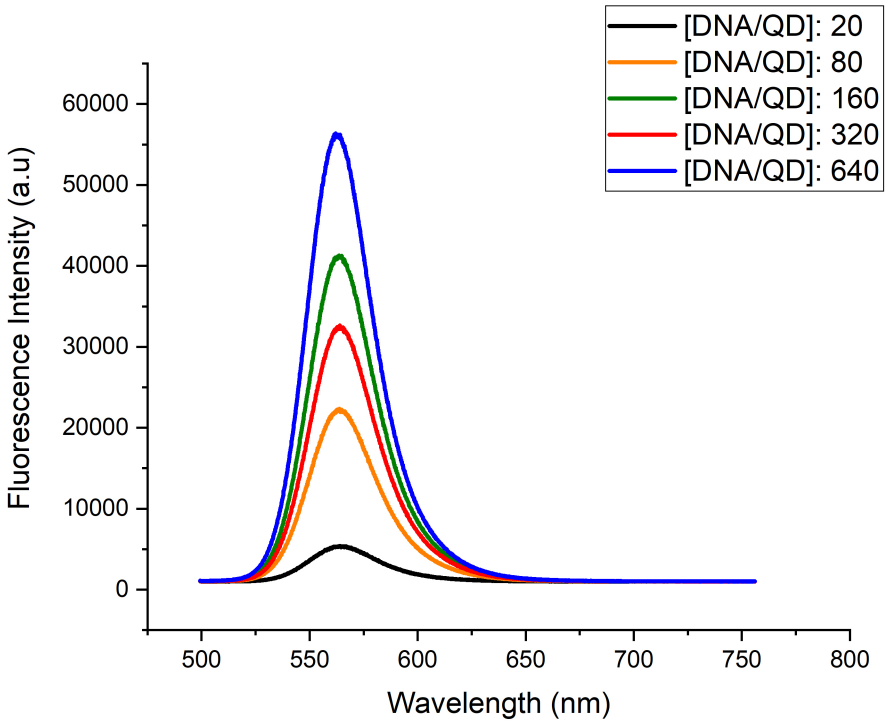

Figure 15. Fluorescence spectra of QD-DNA conjugates excited at 470 nm. The samples with different [DNA]/[QD] ratios were prepared to have the same final QD concentrations as measured by UV-Vis. NaOH was gradually added to each of these samples to achieve a final pH of 9.5-10.

2.4.3 Quantification of the DNA surface ligands

The preceding section provides indirect evidence supporting the idea that more DNA ligands are attached to the QDs as the DNA/QD molar ratio used for ligand exchange increases. Direct quantification of the surface ligands is desirable for a better understanding of the ligand exchange process and for applications that require knowledge of the ligand surface density. Therefore, we used a Cy5-modified oligonucleotide (Cy5-DNA) that shared the same sequence as the dye-free DNA ligand to perform ligand exchange or phase

transfer. After the QD-Cy5-DNA conjugates were purified, the Cy5-DNA ligands were desorbed by the addition of DTT, separated from QDs using centrifugation, and quantified with fluorimetry using a method previously developed to quantify DNA loading on nanoparticles (Experimental Section). Figure 6 confirms that as more DNA is added for ligand exchange, the average number of bound DNA ligands per QD increases. With 20× thiolated DNA molecules, on average only 1.6±0.4 DNA molecules are attached to a QD. As a significant amount of octadecylamine remains on the QDs, such QDs display low stability. The significantly lower fluorescence of the 20× thiolated DNA in Figure 3b shows that a significant fraction of the QDs were trapped within the well. Future LC-MS experiments could help quantify the loading of the hydrophobic ligands on the QDs and provide additional insight into the ligand exchange process. For the 640× DNA, the DNA loading—reaches 9.6±0.7. The trend tracks the increasing mono-dispersity and photoluminescence of these QD-DNA conjugates. The surface density of DNA on QD is calculated to be 0.062 molecules per nm^2, which is somewhat lower than but still comparable to the typical DNA loading achieved for gold nanoparticles, 0.1 molecules per nm^2. [46]

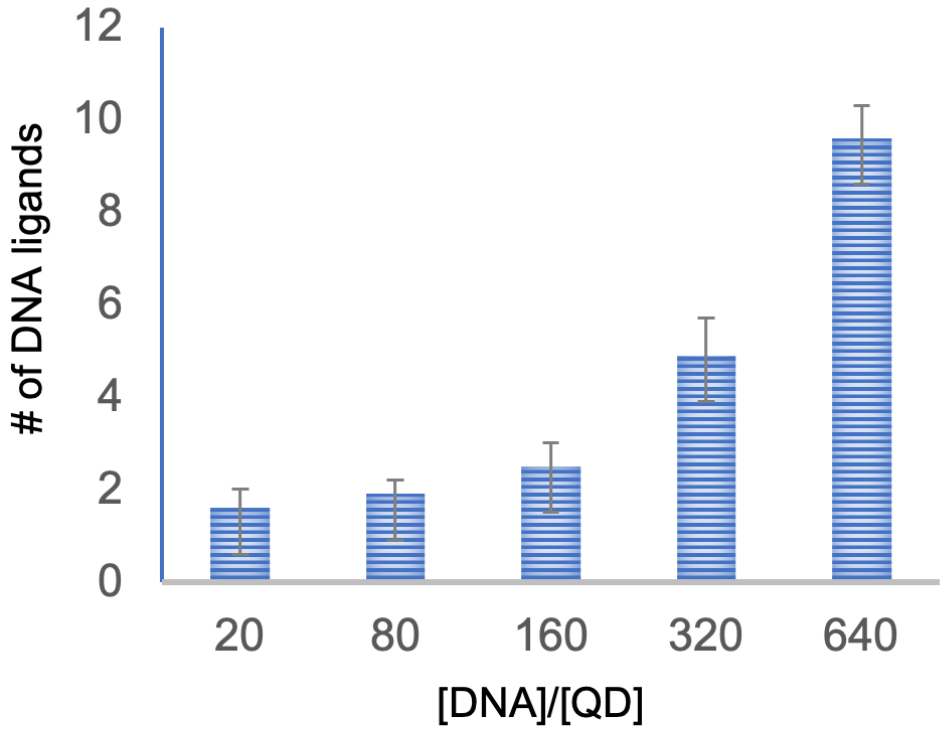

Figure 16. DNA loading as a function of [DNA]/[QD].

2.4.4 Co-assembly of QDs and gold nanoparticles on a DNA origami template

The unique photophysical properties of QDs, such as tunable emission, wide bandgaps, and narrow emission wavelength ranges, make them valuable for energy transfer studies and biosensor designs. [21, 34] Since the energy transfer efficiency is distance-dependent, it is important to precisely control the distance between the nanoparticles as well as the number of the interacting particles. DNA-nanoparticle conjugates can site-specifically bind to self-assembled templates, such as DNA origami [55, 56] and DNA bricks. [41] Captured strands on these templates can hybridize with DNA ligands on nanoparticles to arrange these nanoparticles in sophisticated arrangements with nanometer precision. While there have been a large number of studies that use DNA to direct the self-assembly of gold nanoparticles,[56, 57] fewer analogous studies for QDs have been carried out due to the difficulty in forming QD-DNA conjugates with sufficient colloidal stability under high salt conditions, small sizes, and high photoluminescence. Among those studies, many of them relied on streptavidin-biotin interactions to bind streptavidin-conjugated QDs to biotinylated DNA templates. [58, 59] Unlike those that use base pairing, methods that rely on the streptavidin-biotin interaction lack the diversity of specific interactions that are needed to organize nanoparticles of different sizes, shapes, and compositions on the same template. To evaluate the utility of our method for DNA-directed self-assembly of QDs, we used DNA origami as a template to self-assemble a heterodimer that consists of a DNA-conjugated gold nanoparticle and a DNA conjugated QD.

The schematic of the DNA-directed self-assembly method is shown in Figure 7a. The capture strands at the designed locations on the DNA origami tile can bind the DNA functionalized nanoparticles on the tile, with a predicted center-to-center distance of 22 nm (Figure S15). The self-assembly product of this experiment was then characterized with TEM at 200 kV (Figure 7d) and agarose gel electrophoresis at 65 volts with 0.5× TAE and 12 mM $MgCl_2$ (Figure 7c). For the TEM imaging, Uranyl formate at 2% was used to stain the DNA origami for better resolution (Figure 7d). The rectangular shapes shown in the image are the DNA tiles with the two nanoparticles (QD and Au) annealed to them. The smaller particles correspond to QDs, and the larger ones correspond to Au nanoparticles. The measured center-to-center distance is 20±2 nm, which is close to the predicted distance of 22 nm. 68% of the DNA origami tiles have captured a nanoparticle dimer. 31% of the tiles captured a single nanoparticle. Additional TEM images are provided in Figure S11. AFM images of tiles with a QD and tiles with a heterodimer are included in Figures S12 and S13, respectively.

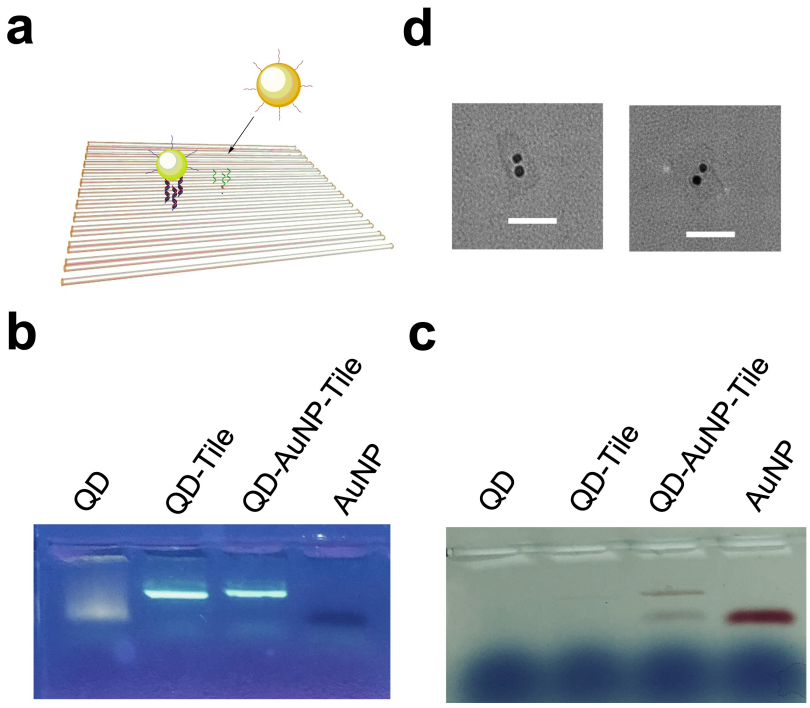

Figure 17. (a) Schematic of annealing of nanoparticles to the origami tile. Binding of Au (dark yellow) and QD (green) onto DNA origami tile. Complementary strands on QD hybridize with capture strands on DNA tile. (b) Agarose gel image of functionalized nanoparticles and annealing products under 302 nm UV light. (c) Agarose gel image under white light illumination. (d)TEM image of self-assembled Au and QD on origami tile. Scale bar is 50 nm.

In the AFM images, the QDs and AuNPs can be distinguished by their topographical heights. The QDs have an average height of 5 nm ± 2 nm, and the AuNPs have an average height of 12.2 nm ± 0.8 nm. Gel electrophoresis results in Figures 7b and 7c confirm that both the QD and the AuNP successfully bound to the DNA origami tiles. The free QD-DNA conjugates (first lane from the left) run faster compared to QD-DNA conjugates that are annealed with the tile (second lane from the left, Figure 7b), suggesting successful binding of QDs to the DNA origami tile. A picture of the same gel was taken under white light illumination to better visualize the mobility of DNA-conjugated AuNPs compared to DNA conjugated AuNPs annealed to the tile (Figure 7c). The fourth lane shows the mobility of free AuNPs, and they run faster on the gel compared to AuNPs when annealed on the tile (the third lane from the right). The AuNPs in the third lane show two bands: the band on the bottom corresponds to free excess Au nanoparticles, and the band on top corresponds to the AuNPs pinned on the DNA origami tile.

2.4.5 Application of QD-AuNP heterodimers for energy transfer studies

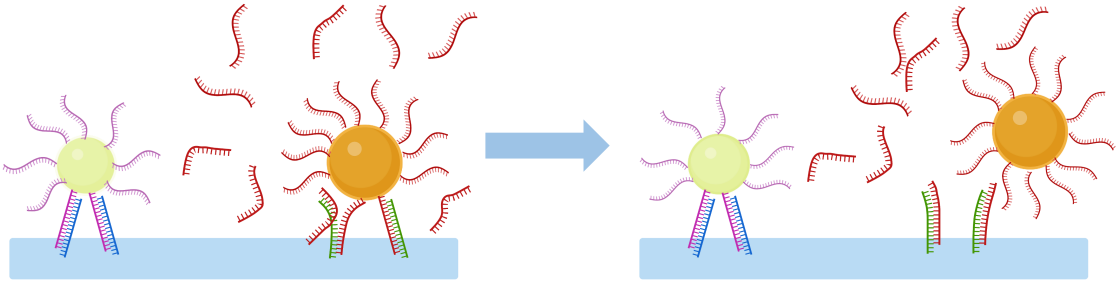

Figure 18. Schematic showing how addition of excess DNA ligand (a) causes displacement of AuNP (dark yellow) from the origami tile (b).

Energy transfer between nanoparticles in close proximity is extremely sensitive to interparticle distances. [34] The use of DNA origami as a scaffold provides the ability for site-specific binding of nanoparticles. [7, 40, 60] Here we have performed a proof-of-principle experiment that used the self-assembled heterodimers for energy transfer studies and biosensor design. We designed a simple experiment to study how the binding of AuNP to the origami and its displacement affect the PL of the QDs (Figure 8). After dimer formation, excess ligands that are complementary to the capture strands for the AuNP were added to dissociate the AuNP from the DNA origami tile and consequently increase the distance between the QD and AuNP. Fluorescence spectra before and after the displacement were measured to study the effect of energy transfer.

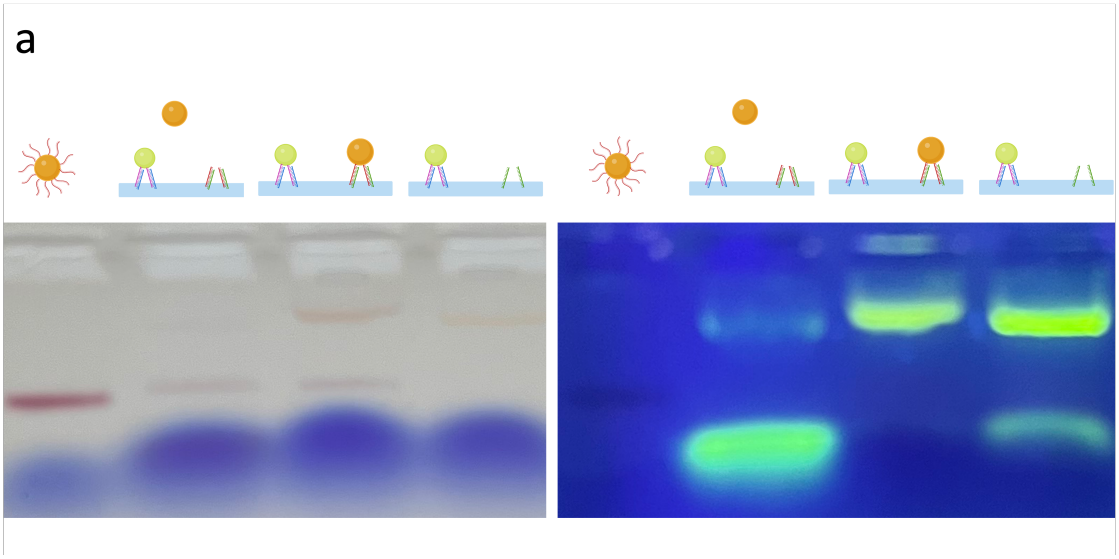

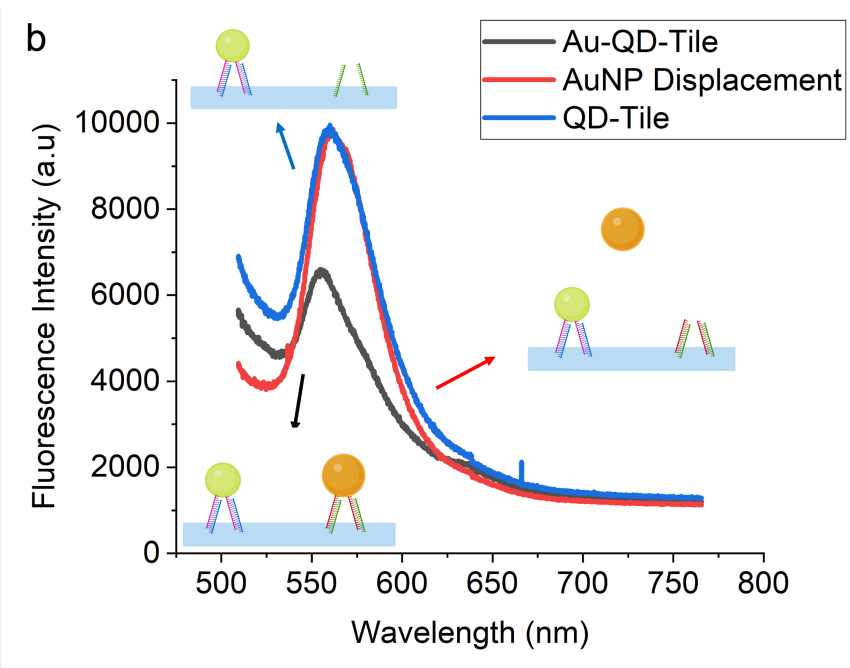

Figure 19. (a) Agarose gel (1% with 0.5× TBE/12 mM MgCl2 running buffer) left to right; DNA conjugated gold nanoparticles (AuNPs), displacement of AuNPs by adding excess ligand (AuNP displacement), Tile. (b)Quenching effect of AuNPs on QDs bound to DNA origami; PL of QD-Tile (red), Au-QD-Tile(blue) and Au-QD-Tile after addition of ligands to displace AuNPs (AuNP Displacement, dashed black).

QDs and AuNPs were annealed to the DNA origami, respectively, to form the dimer structures, which were then purified using size exclusion spin columns [51] to remove unbound nanoparticles. The gel results in Figure 9a show that the nanoparticles were successfully bound to the origami tile (AuNP-QD-tiles): the top band lines up to the band for the tiles, and the bottom band shows the presence of excess unbound AuNPs. After adding the excess ligands at a concentration of 80 mM (520 times in excess relative to the amount of the origami tiles), the top red band disappeared (AuNP displacement), and the bottom band lined up with the band for unbound AuNPs on the left, showing that the AuNP dissociated from the tile. Lastly, in order to measure the quenching effect of AuNP on QD photoluminescence, the fluorescence intensities at 560 nm of QD-Tile, AuNP-QD-Tile, and tiles after displacement of AuNPs were measured at an excitation wavelength of 470 nm (Figure 9b). A comparison of the red curve representing the tiles with a QD and the blue curve representing tiles with a heterodimer shows that when the AuNP is bound to the QD-tile, the PL at 560 nm decreases by 40%. After ligands were added to displace the gold nanoparticles (dotted curve, AuNP displacement), the PL intensity almost fully recovered (Figure 9b). Independent trials–showed that after AuNP displacement, the fluorescence intensity is enhanced by 39±5% on average (Figure S14).

The average surface-to-center distance between the AuNP and the QD increased from ~15 nm to a few hundred nanometers, which is too large to enable significant energy transfer. Therefore, these unbound AuNPs can no longer effectively quench the PL of the QDs. It should be noted that the PL near 525 nm is more complex. The QD-tiles sample has the highest PL intensity, and the other two samples have lower intensities. As the

wavelength is near the surface plasmon resonance of the AuNPs, factors contributing to the differences include direct absorption, surface quenching, and metal surface enhanced radiative decay. [61] While a more systematic study is needed to elucidate the complex trend, the results nevertheless have shown that our method produces QD-DNA conjugates with small sizes that make them suitable for energy transfer studies. And the increases in PL upon addition of DNA suggest that the heterodimer on DNA origami provides a signal transduction mechanism for detection of nucleic acids.

2.4.6 Surface functionalization of Quantum dots with bidentate dithiol-modified DNA

Functionalizing quantum dots (QDs) with dithiol DNA could be a more effective method than functionalizing with monothiol DNA for several reasons. Firstly, dithiol DNA has two thiol groups per molecule, while monothiol DNA only has one. Thiol groups can form strong bonds with the surface of QDs, allowing the DNA to anchor more firmly to the QD surface. Secondly, dithiol DNA can form stronger, more stable bonds with the QD surface than monothiol DNA, which results in more complete functionalization of the QD surface and fewer unbound or unfunctionalized QDs. The formation of two thiol bonds between the dithiol DNA and the QD surface can increase the stability of the functionalized QDs, making them less likely to degrade or detach from the surface over time. Furthermore, dithiol DNA is less susceptible to oxidation than monothiol DNA, which can cause the thiol groups to lose their ability to bind to the QD surface, leading to a decrease in the stability and functionality of the QD-DNA conjugate. HPLC (high-performance liquid chromatography) and LC-MS (liquid chromatography-mass spectrometry) are commonly used analytical techniques for characterizing dithiol-modified DNA. HPLC is a powerful tool for separating and purifying different components of a mixture, including DNA molecules with different sizes, conformations, and modifications.

Dithiol-modified DNA can be separated from unmodified DNA or other by-products using HPLC based on differences in their physicochemical properties such as hydrophobicity and molecular weight. The isolated fractions can then be analyzed by LC-MS to confirm the presence of the desired product and determine its mass and purity. LC-MS is particularly useful for detecting small amounts of modified DNA, as it can provide information on the molecular weight and composition of the molecule. The technique can also be used to identify the presence of any adducts or contaminants that may be present in the sample. Overall, HPLC and LC-MS can be used in combination to provide detailed information on the size, purity, and composition of dithiol-modified DNA, making them valuable tools for the characterization of such molecules.

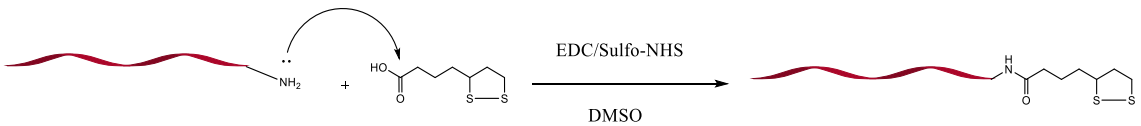

Figure 20.synthesis of the dithiol-modified DNA mechanism.

Using the method described before, we obtained an overall yield of 75%, which was calculated using a calibration curve of the HPLC peak area and the use of unreacted DNA as a control. The HPLC spectra in Figure 21 show that the unfunctionalized DNA (amino-DNA) is eluted off the column at a retention time of 21 min, while the functionalized DNA product (dithiol DNA) is eluted later at 26 min. The LC-MS of the reactant (unfunctionalized) and product (functionalized) DNAs are shown below in figure 16. The peak at 9274.2 g/mol corresponds to the functionalized DNA after the amide coupling, and the peak at 9085.9 g/mol corresponds to the unfunctionalized DNA that was characterized as a control. The peaks that show up at lower molecular weights are salt adducts and fragmented DNA peaks.

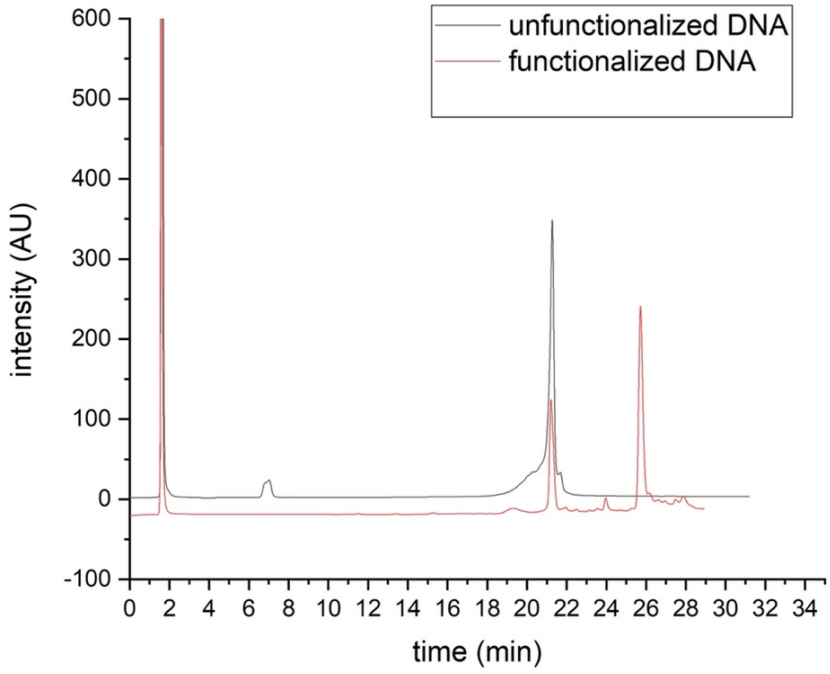

Figure 21.Reversed phase HPLC spectra of the modified DNA. Unfunctionalized DNA was ran on the column as a control (black spectra), the functionalized DNA (red spectra) shows a slight unreacted DNA (at t21) and the final product at t26.

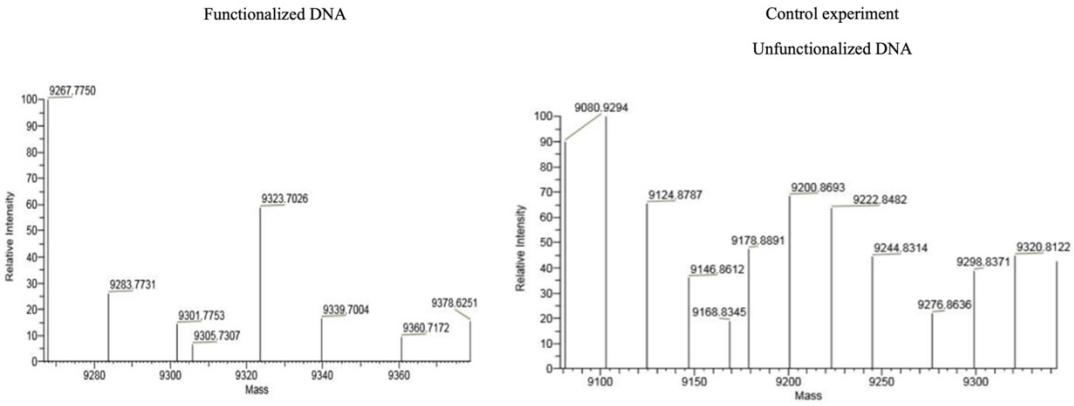

Figure 22. ESI-Mass spectrometry of functionalized DNA (9274.2g/mole) and unfunctionalized DNA as a control experiment (9085.9g/mole)

2.4.7 Cap exchange of Quantum dot nanoparticles using dithiol-modified DNA

The procedure for exchanging caps on QDs using dithiol-modified DNA is the same as the one used with monothiol-modified DNA. Figure 17.b demonstrates that the QDs were successfully transferred from the organic layer (at the bottom) to the aqueous layer (at the top). A mixture of monothiol-modified DNA-QD was made as a control. Gel electrophoresis is another method that can be used to characterize DNA-QDs after the cap exchange has been completed. Figure 17.a demonstrates that following the cap exchange, functionalized QD nanoparticles pass across a 1% agarose gel. Additionally, the band is clear and distinct, which is an indicator that the ligand exchange was effective.

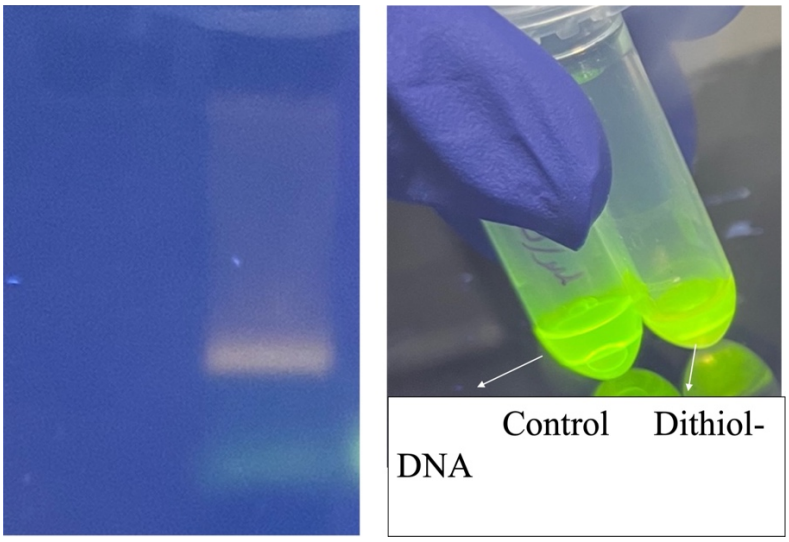

Figure 23. (a) Agarose gel (1% with 0.5× TBE/12 mM MgCl2 running buffer) of functionalized QDs with dithiol-modified QDs. (b)phase transfer of DNA-QD conjugates, with monothiol DNA (left) as a control, dithiol DNA (right).

2.5 Conclusion and Outlook

We have shown that our one-step ligand exchange method can form compact, monodisperse, and bright QD-DNA conjugates from commonly available hydrophobic quantum dots. These QD-DNA conjugates have sufficient colloidal stability to bind to a DNA origami template at prescribed separations from a gold nanoparticle, enabling investigation of energy transfer between QDs and AuNPs. This study focused on two key parameters, pH and [DNA]/[QD]. Our simple method can be extended to other QDs with different hydrophobic ligands and compositions. Multidentate ligands that bind to QDs more strongly may be used to further enhance the stability of these QD-DNA conjugates. [62, 63] Like other ligand exchange methods,[23] our method requires a relatively large excess of DNA ligands to achieve high DNA loading on the QDs. Future studies that systematically explore the effects of QD composition, size, length of DNA, reaction time, and stronger binding groups such as dithiols would provide additional insights into the ligand exchange process and increase its efficiency.

With further optimizations, our designer nanostructures may serve as a signal-on sensor for ultra-sensitive detection of nucleic acids and other biomarkers [64] as the PL signal can report the presence of nucleic acids or other biomarkers that displace the AuNPs from the DNA origami tile (Figure 7). The sensitivity may be substantially enhanced by improving the quenching efficiency of the heterodimers and introducing a toehold to accelerate strand displacement. [65] In addition to forming simple dimer structures, these QD-DNA conjugates may be assembled into superlattices as well as complex clusters with novel emergent properties. Therefore, this approach has the potential to make QDs more ubiquitous components in DNA-mediated self-assembly.

2.6 Appendix

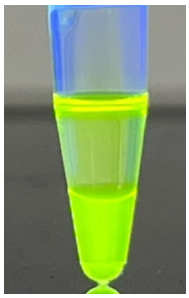

Figure S1. Ligand exchange without DMSO. The bottom phase contained CdSe/ZnS QDs dissolved in chloroform (bottom phase) and the top phase contained DNA ligands dissolved in water (top phase). Reaction conditions: [DNA]/[QD]=640 and final pH=9.5-10. The CdSe/ZnS QDs stayed within the organic phase, showing that ligand exchange/phase transfer was unsuccessful without DMSO in the reaction mixture.

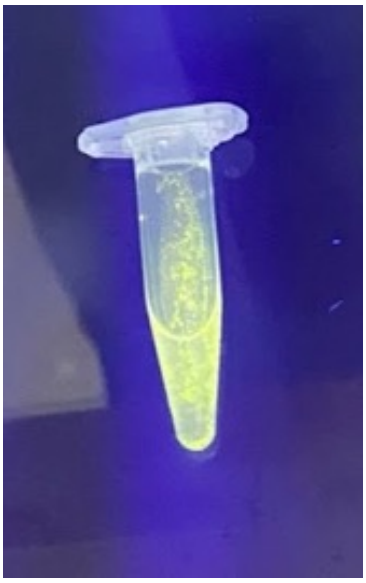

Figure S2. Ligand exchange with rapid addition of NaOH. Reaction conditions: [DNA]/[QD]=640, final pH=9.5-10. Aggregates are visible under UV light at 302 nm.

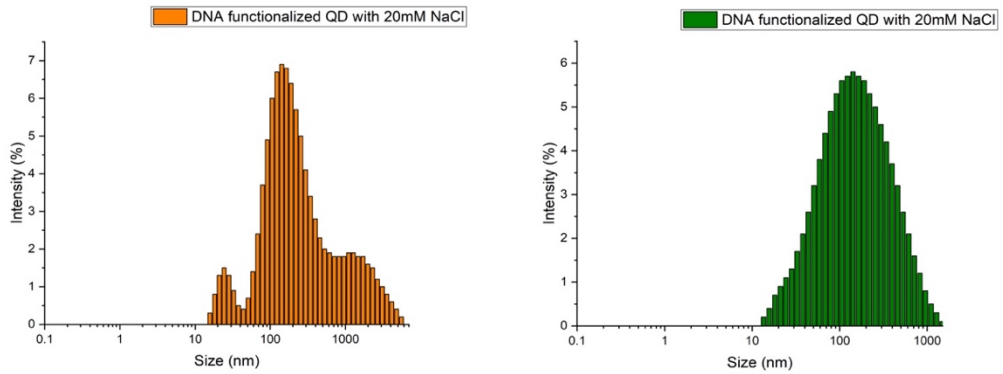

Figure S3. DLS hydrodynamic size distributions of QDs from two independent DNA conjugation trials that increased the concentration of NaCl in a step wise fashion. The concentration of NaCl was increased to a final value of 20 mM at [DNA]/[QD]=640.

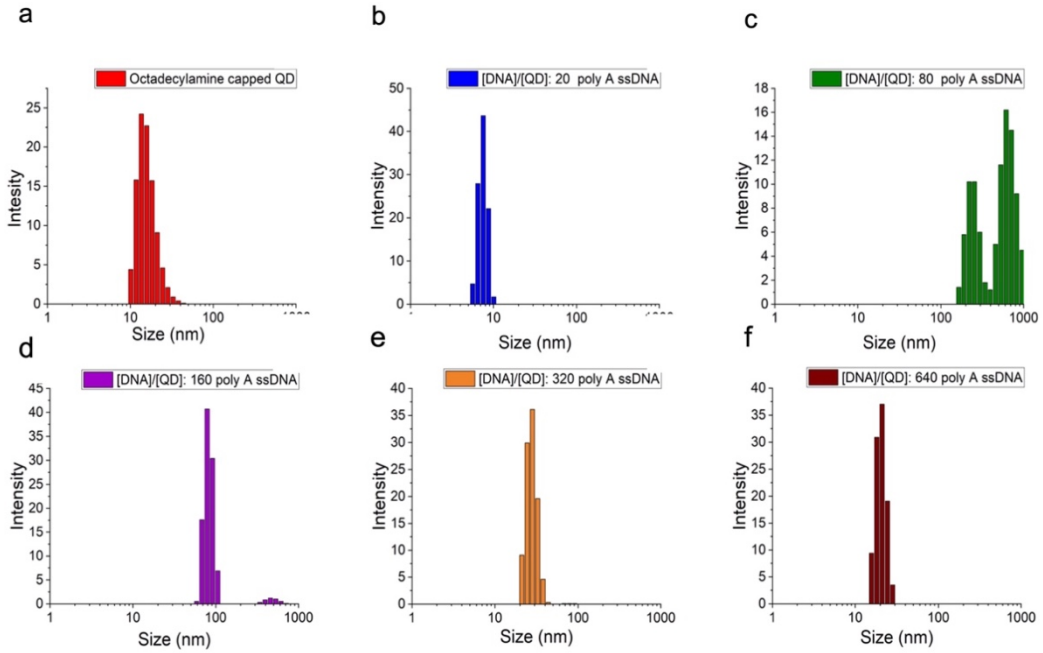

Figure S4. DLS hydrodynamic size distributions of QDs conjugated with the poly A DNA ligands (5' CA TGT TCA GCG TAA AAAA/$(CH_2)_3$SH 3') at different [DNA]/[QD]: (a) no DNA, (b) 20, (c) 80, (d) 160, (e) 320, (f) 640.

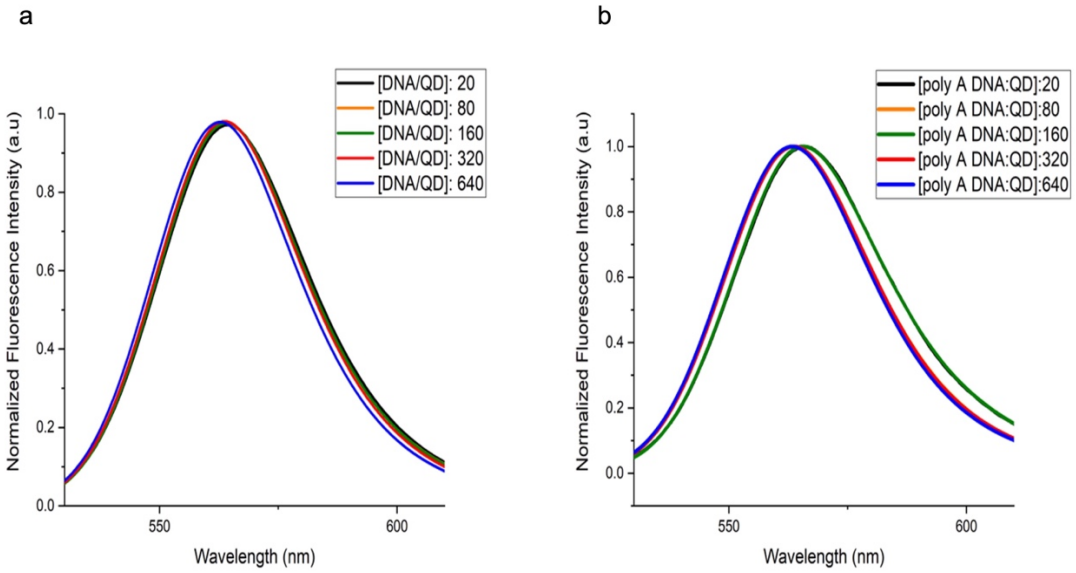

*Figure S5. Fluorescence spectra of the QD-DNA conjugates prepared with different [DNA]/[QD] ratios. (a)Spectra of QDs conjugated with regular DNA ligands (5′ CA TGT TCA GCG TAA **TTTT**/$(CH_2)_3$SH 3') showing a maximum red shift of 2.0±0.9 nm. (b)Spectra of QDs conjugated with poly A DNA (5′ CA TGT TCA GCG TAA **AAAA** /$(CH_2)_3$SH 3') showing a maximum red shift of 2.7±1.3 nm. To visualize the shift in the emission peak with respect to that of the reference ([DNA]/[QD]=640), the peak intensities were normalized. The red shift is more pronounced for lower [DNA]/[QD] and there is an overlap in the spectra of [DNA]/[QD] :20(black), 80(orange) and 160 (green) in both (a)and (b).*

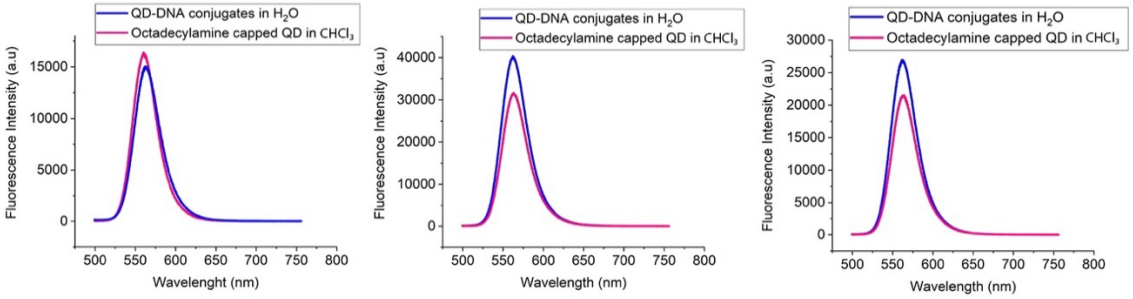

Figure S6. Fluorescence spectra of as received, hydrophobic QDs in $CHCl_3$ and DNA-conjugated QDs at [DNA]/[QD]=640 in H_2O from three independent trials. The QD concentration was 0.4μM. Excitation wavelength: 470 nm. Slit width: 5 nm. Integration time: 0.2 s.

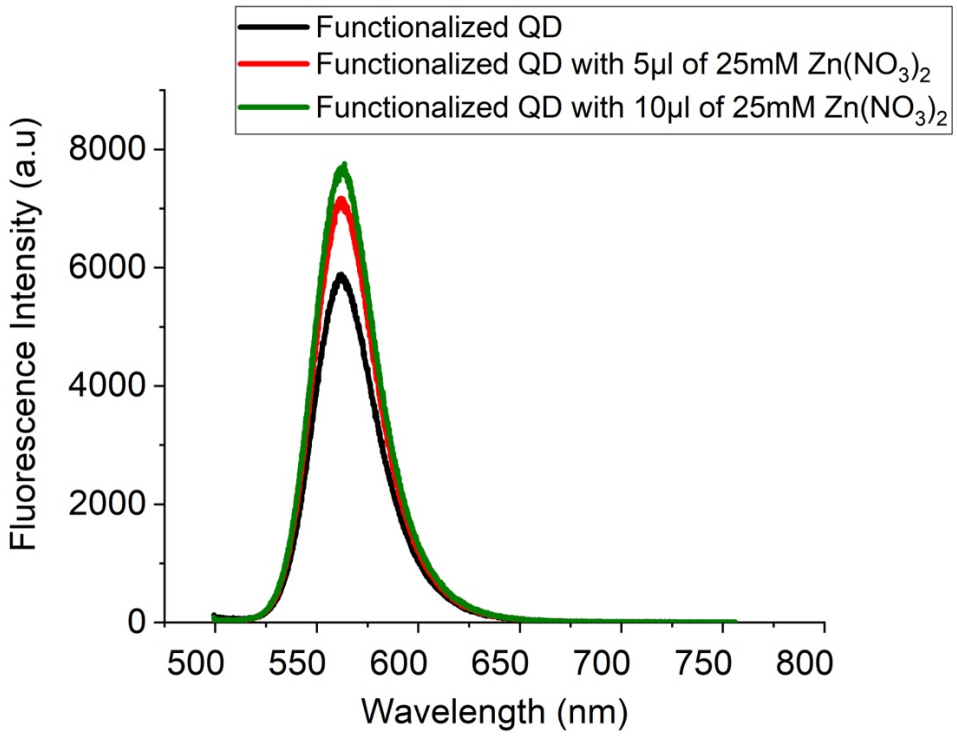

Figure S7. Fluorescence spectra of QD-DNA conjugates that were prepared with different amounts of $Zn(NO_3)_2$. The total volume of the aqueous phase was kept constant at 150 µl.

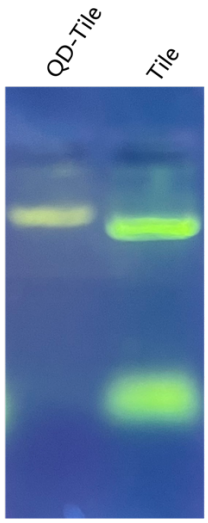

Figure S8. Agarose gel (1%) image of QD-tile annealing product (left) and DNA origami tiles (right). The QD-tile band has a lower mobility than the tile band. Moreover, the QD-tile band has a different color due to emission from the QDs. This high-resolution gel image was achieved by increasing the concentrations of the reactants by 5X and concentrating the product with a spin filter.

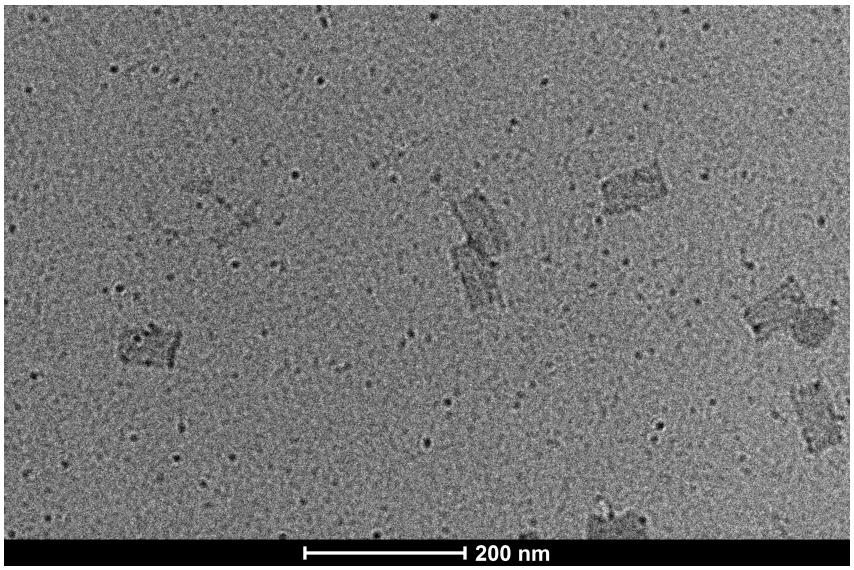

Figure S9.TEM image of the DNA origami tiles without nanoparticles using 2% Uranyl Formate stain.

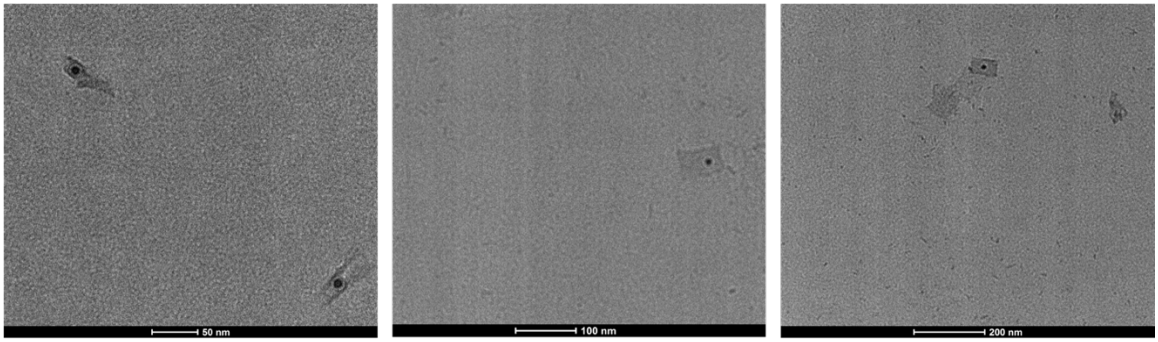

Figure S10. TEM images of QDs on DNA origami using 2% Uranyl Formate stain.

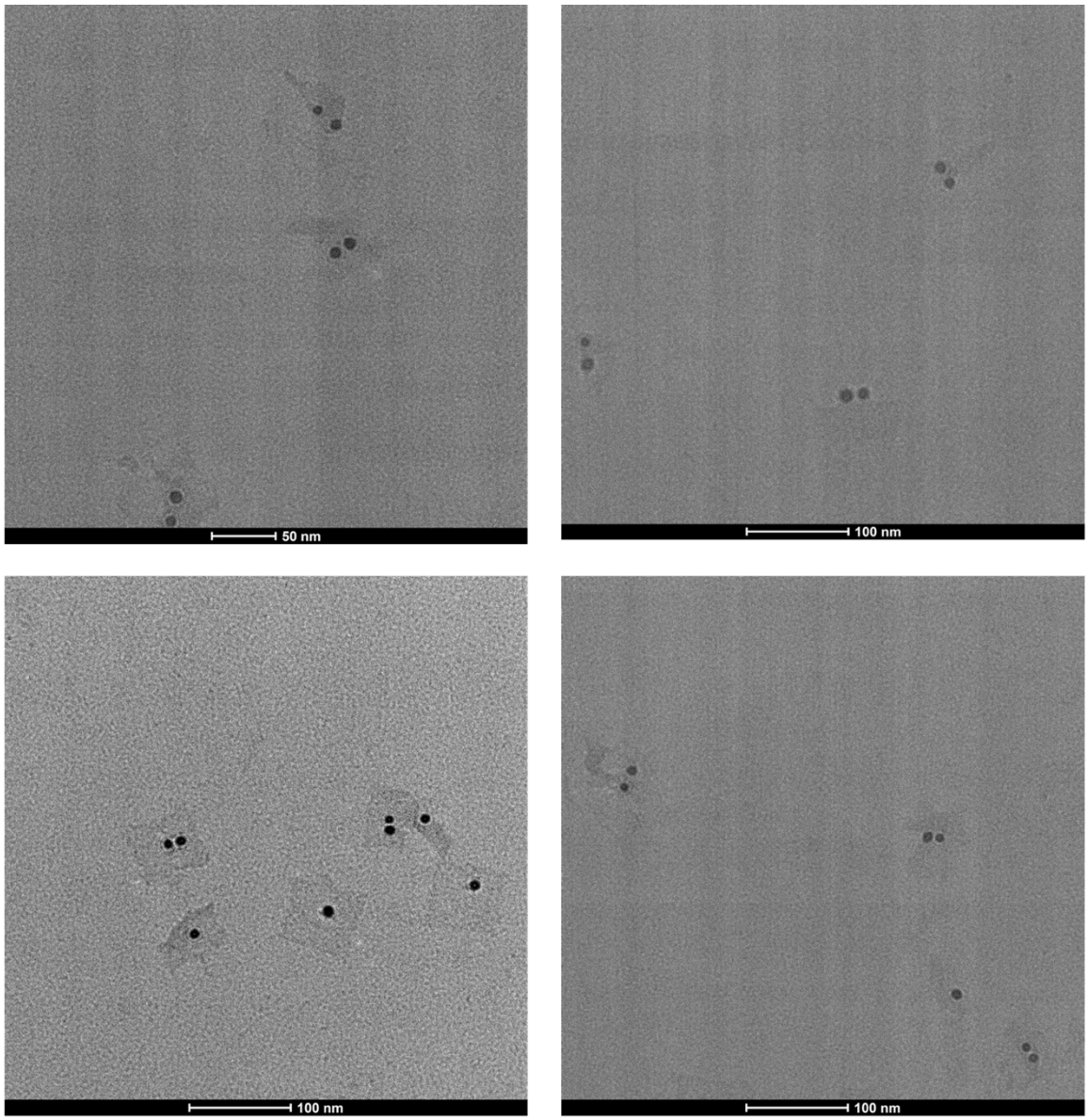

Figure S11.TEM images of AuNP-QD heterodimers on DNA origami using 2% Uranyl Formate stain. Yield of dimer formation is approximately 68%.

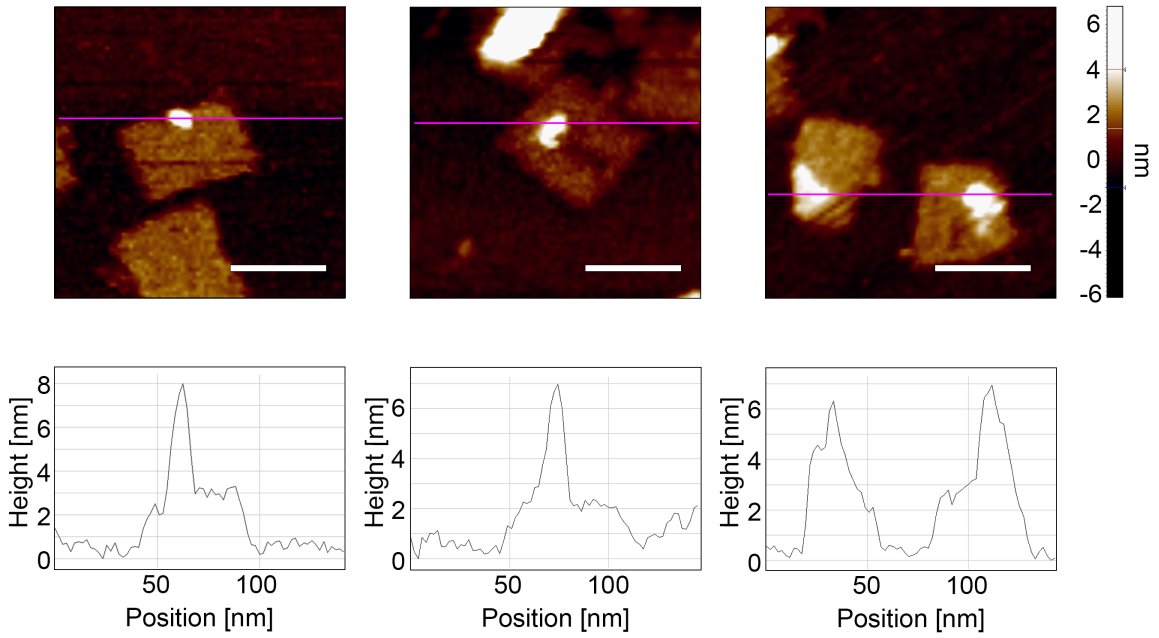

Figure S12. Representative Intermittent contact mode AFM images and cross-sectional profiles of QD-Tiles in a 5mM $NiAc_2$ and 1X Tris Acetate EDTA buffer. The average height of these QDs is 5±2 nm. Scale bar is 50 nm.

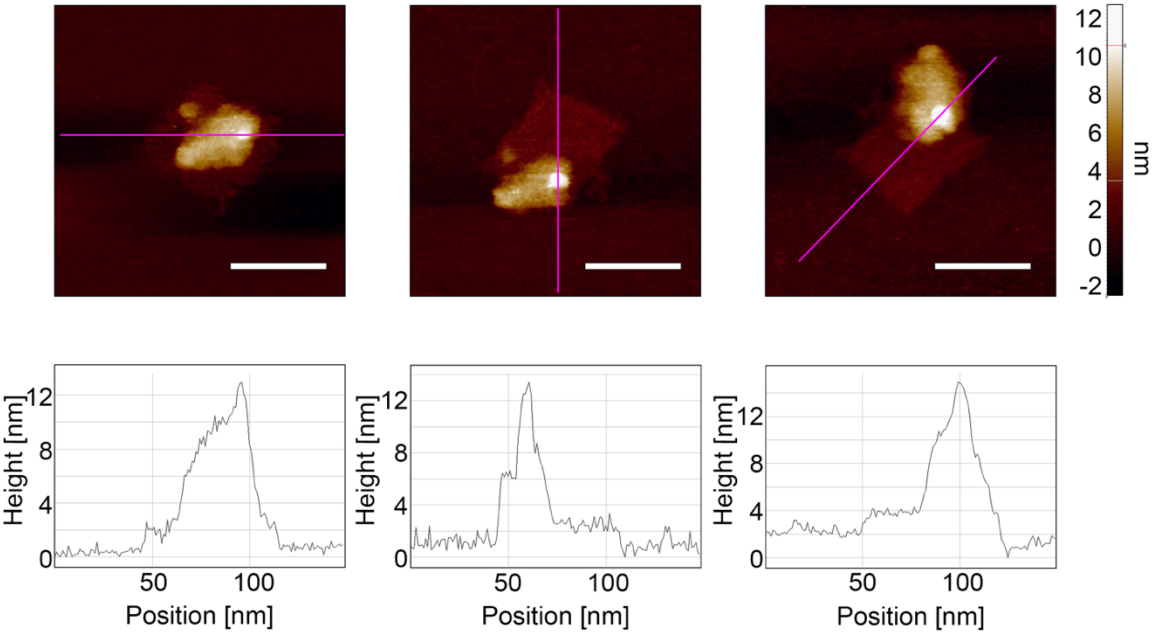

Figure S13. Intermittent contact mode AFM images of Au-QD-Tiles in a 5mM $NiAc_2$ and 1X Tris Acetate EDTA buffer. The average height of AuNP is measured to be 12.3 ±0.8 nm. Scale bar is 50 nm.

We discovered that QDs and AuNPs have different topographical heights in AFM. QDs on the tiles were resolved as protrusions that are 5±2 nm high. The AuNPs were

resolved as protrusions that are 12.3±0.8 nm high. AFM was unable to resolve features associated with QDs when a QD and an AuNP are co-assembled on the DNA origami. As the AuNPs are notably taller than QDs, the features associated with QDs are obscured by the topographical features of the AuNPs in close proximity due to the tip convolution artifact. [2]

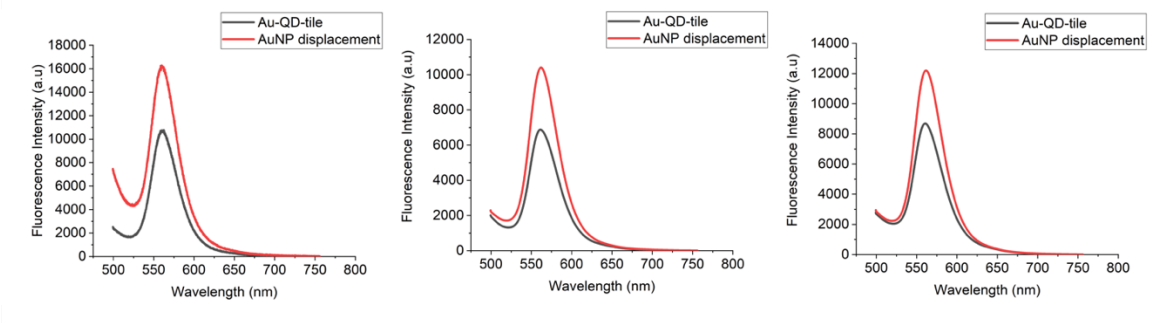

Figure S14. Fluorescence spectra of Au-QD-Tile(black) and Au-QD-Tile after addition of ligands to displace AuNPs(AuNP Displacement, red) from three independent trials. The fluorescence intensity increases by 39±5 % on average after ligand addition.

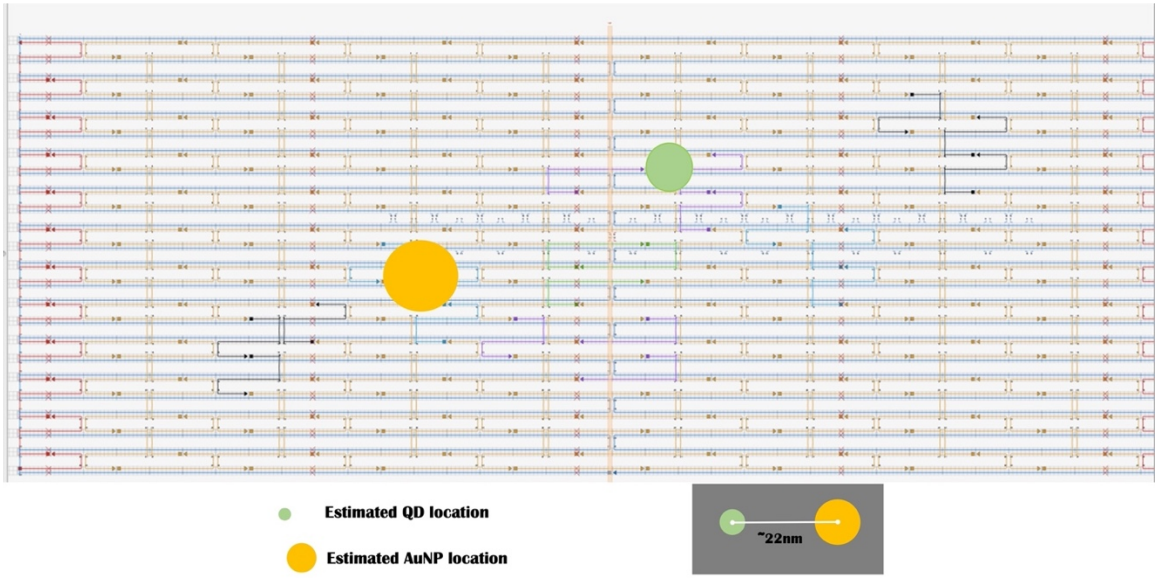

Figure S15. DNA origami design and approximate locations of AuNP and QD on the origami tile.

Sequence of capture strands: 5' to 3'

Capture Strands for QD:

TTACGCTGAACATGTTGT AGT AAC CTG ACG AGA AAC ACG TTT AAC G

TTACGCTGAACATGTTAAATCCAAAGAAAATAGCAGCCTTTGAAGGAAA
TTACGCTGAACATGTTCCGCACTCCGTAGGAATCATTACCTTTATCCC

Capture Strands for AuNP:

TAATCTGCGACTACTTAGTAGCATACAT TTCGCAAATGGTAGGTCAGG
TAATCTGCGACTACTTTGATAAATGAGTAATGTGTAGGTACTAATAGT
TAATCTGCGACTACTTAAAGATTAGTACCTTTAATTGCTCAGTTTGAC

Sequence of unmodified staples: 5' to 3'

1	GCTTAGATATTTTAGTTAATTTCAAGCCTGTT
2	AAAGTAATTATGCGTTATACAAATAAACTTTT
3	TGGCCCTGAGAGAGTTGCAGCAAGTGGGGTGC
4	AGGCTTGCATTGGGCTTGAGATGGCAACACTA
5	CATTCAACGATAGCGTCCAATACTCCTGACTA
6	AACGAGCGTAACTGAACACCCTGACAATAGCT
7	TCAAAAATTAAGAAACGATTTTTTCAGAACGA
8	GTTAATGCCCCCTGCCTATTTCGCAGGAGGT
9	GTTTCCATGAACCGAACTGACCAAGACCAGGC
10	TCATAAGGTAAACGGGTAAAATACAAGACAGC
11	CTTCTGGTTTCAGGCTGCGCAACTGAAATTGT
12	AATAACATATAAACAGCCATATTAGCGCCCAA
13	CATGGTCATGAGCTAACTCACATTTCACCGCC
14	ATCGGAACCTCCAAAAAAAAGGCTTTCAACAG
15	GACACCACAGAAACAATGAAATAGACAAAGTC
16	CAACGTAATCATTGTGAATTACCACGCCAAA
17	GGTTTAATCAATATATGTGAGTAATTAATT
18	CACCAGAGCCTCAGAGCCGCCACCGACAGCCC
19	TTCGCCAGCCGGAAACCAGGCAAAATCTAA
20	GAGGCTTGTGAATTTCTTAAACAGAGTTTTGT
21	TAGCAAGCCAAGAACGGGTATTAAGAGCCAGT
22	AGTTTTGCCGAGGCATAGTAAGAGTTTAATTT

23
TACATAAACGTCAGATGAATATACAAGGGTTAGAACCTACAGTATTAG
24 ATTGCAATAAAAGGGACATTCTGTGAGGCG
25 TATAACTATAACCTCCGGCTTAGGGGCGCGAG
26 GCCACCACCCGCCGCCAGCATTGAGAACCTAT
27 AAAGATTCTATTCATTGAATCCCCGAATGACC
28 CAATTCTGAGAATTAGCAAAATTAAAGGATAA
29 AGAAACCATAAGAACGCGAGGCGTCCAACGCT
30 TAGTATCATCTGTCCAGACGACGAGAGCATGT
31 TTATTTACTGACGCTCAATCGTCTCATACGAG
32 TGAGTAGGCACAGACAATATTTGATAGCCC
33 TATCCGCTCATAAAGTGTAAAGCCCGGTCCAC
34 CCGGAAGCACAATTCCACACAAGAAATGGA
35 CAGATAGTAGCAAACGTAGAAAAAATTATT
36 TTCCCTTTAATGGTTTGAAATAAATAAACA
37 ATCGCAAGATCAAAATCATAGGTCACAAACAT
38 TCATAGTCTGTAGCATTCCACAAGAACCAC
39 AACCAAACTCGTTTACCAGACGCCGTTTTT
40 AGCCGCCGTCAGACGATTGGCCTATAAACA
41 GGGCGATCACTCCAGCCAGCTTTCCAAAAATA
42 CCGAGGAAGCATGATTAAGACTCCCACCGACT
43 TCATAACCATAGCGAGAGGCTTTTACTTCAAA
44 CTAATGAGTAGCTGTTTCCTGTGTGTTGGGAA
45 CCGTAACACAGACGTTAGTAAATGCAGCTTGC
46 AAAGACATCAGACTGTAGCGCGATTAGCGT
47 AGTAGCATACATTTCGCAAATGGTAGGTCAGG
48 TTGCCATGCAGTCTCTGAATTTATGATACA
49 TGGAAGTTAGCATAAAGCTAAATCTACTTTTG
50 CCTGTCGTCATGCCTGCAGGTCGACTGCAAGG
51 ATTTTGCGTCATCATATTCCTGATAGTTACAA
52 TGATAAATGAGTAATGTGTAGGTACTAATAGT
53 CATTAAACCAATGAAACCATCGTCCCTCAG

54 TGAGGCAGACCCTCAGAACCGCCAAAGGCCGG
55 GCTGGTTTGCCCCAGCAGGCGAAGGAGCTAA
56 AATTGTGTATACACTAAAACACTCCGGTCGCT
57 AACAGTTGAGAAGATAAAACAGAGGGCCAACA
58 TTATAGTCCATTTTTGCGGATGGCTTGATTCC
59 GGTTTTGCTCAGTACCAGGCGGATCCCATGTA
60 AAGAACTGACGCAATAATAACGGAGAAACAAA
61 CCAGACCTTTAATTCGAGCTTCCGCCAACA
62 GTATGGGCAAGCCCAATAGGAAAAGTGCCG
63 TGGTAATAACCCTTCTGACCTGAACGAACGAA
64 CACCATCAGAAAGGCCGGAGACTTTCAATT
65 TATTAATTTCATCAATATAATCTAACGGAT
66 CGTCTTTCCTGAGTTTCGTCACCAATTAGCGG
67 GACAACTCTACTTCTGAATAATGGAGTAACAG
68 ACAGGAGGCCGATTAAAGGGATTTGGAAATAC
69 TTGAGAGAGAACCCTCATATATATACAGGC
70 TATCGCGTGGAAGCAAACTCCAACCAATAACCTGTTTAGCGGTGGCAT
71 AATAATAACTTGCGGGAGGTTTGCACCCAG
72 GGCGCCAGGGTGGTTTTTCTTTTCTCGGGAAA
73 ATAAATCAGAATATAATGCTGTAGACGGTGTC
74 TACCTTTTAATTACCTTTTTTAATTAGCGATA
75 TGTCCATCACGCAAATTAACCGTCACTTGCC
76 CCCAAAAATTAAATGTGAGCGAGTCTGCCAGT
77 ATTAGAGAAGAGGAAGCCCGAAAGGCAAAAGA
78 TTTCAGCGCTCAGAGCCACCACCCGCCCGGAA
79 AAGAGGTAGAAGCAAAGCGGATAAAATGTT
80 CGCCCACGCGCCGACAATGACAGCAAAATC
81 AGCATCACGCCAGCAGCAAATGAAAAGCGCCA
82 AGCAGCGAGTAATGCCACTACGAACCGGAACG
83 CGGAATTAGAACAAAGAAACCACCCAGCTCAT
84 CATTAGATTAACATCCAATAAATCTTTAAATG

85 GGGAGAATTCTTTCCAGAGCCTAAGGCTTATC

86 TACAACGCTAGCGTAACGATCTAACTTGATAC

87 GTCATAAAATCAGTTGAGATTTAGCAGTCAGG

88 AACATGTTCATAATTACTAGAAAATCTTCTGA

89 TACTTAGGGCACCAACCTAAAAGCTTTTGC

90 TGGAAAGCCTTTTCATAATCAAAAAAGTTTGC

91 GTATAAAAATATAAAGTACCGACTTTCCTT

92 AAAAATACAGCGTAAGAATACGTGAAGAACTCAAACTATCAAAGAGTC

93 GCATAGGCAAGAAAAATCTACGTTACAGGTAG

94 CGGGAGAAGTCTGGAGCAAACAAGCATGTCAA

95 TATAATCAGTGAGGCCACCGAGTAGGCCTTGC

96 TTGGATTAGTATTAAATCCTTTGCGGCAAATC

97 CAAGAAAAATTGCTTTGAATACCATATCAGAT

98 GTCAGTAAATATCTGGTCAGTTCCGAACGT

99 ACCAGTAACAGGAAAAACGCTCATTAGACAGG

100 CAGTGCCTTGAGTAACAGTGCCCGTTGATATT

101 GGGATCGATTGTATCGGTTTATAATTTTCT

102 GATCCCCGACTGCCCGCTTTCCAGACCAGTGA

103 GTCGGATTACCCCGGTTGATAATCAGGTCATT

104 AATAAGAGGCCAACGCTCAACAGTCAAATCCA

105 TATTCTGAAACATGAAAGTATTAAGAGGCTGA

106 TAGACTGTAATGCAGATACATATTATGCGA

107 ACCTCCCGTCCCATCCTAATTTACCAATAAAC

108 AGAGGGTATTTATCCTGAATCTTATTTAGCGA

109 ACCTGAGCAGAGGCGAATTATTCAAGTCAAAT

110 TCGAGAGGGTTGATATAAGTATATCATTTTCA

111 ATCATTCAAATCAGATATAGAATTTGCCAG

112 CAATGCCTTAATGCCGGAGAGGGTAGCAAATA

113 CGGTATTCATCAATAATCGGCTGTCAAAAGGT

114 TCAAATATTAAGACGCTGAGAAGATTAACAAT

115 ACGTTGGGTGGCTGACCTTCATCAACGGTCAA
116 CCAGCTGACGACGACAGTATCGCAGCTTTC
117 CCTCAATCTTAACACCGCCTGCAAGTCACACG
118 CCGGAATCAGCTAATGCAGAACACAAGAAA
119 GATGGGCGTTGGGTAACGCCAGGGGCCAGTGC
120 AATCGCGCAAAAGAAGATGATGAATGAGAGAC
121 ACCAGAGCAATAAATCCTCATTAAAACGGGGT
122 AAGATCGCGGTGCGGGCCTCTTCGTTCGTAAT
123 TTCATTTGACATCGGGAGAAACAACTGATTGT
124 ATTTAGACATATCAAAATTATTGATTTTCA
125 GACTCCTCAAGAGAAGGATTAGGGTACAAAC
126 ATCAACACAGGAAGATTGTATAAGCTATTT
127 CTACATTTATTGGCAGATTCACCACAGTGCCA
128 CAATTCTAAAGATTCAAAAGGGTGAATATGAT
129 TGTAATTTTCGCCATATTTAACAAAAAGCGAA
130 CCGCCACCGAGTGAGAATAGAAAGTTTTCACG
131 TTGAAAATGAGGGTAGCAACGGCTATGAGGAA
132 TACCTTTTTATGTAAATGCTGATGAGGGCTTA
133 AAATTTTTATCTACAAAGGCTATCAGAAAAGC
134 ATTGAGAAAGGCAGAGGCATTTTCACCAAGTA
135 ATAAAGGTGAAGCCCTTTTTAAGACATTAGAC
136 CTGAAAATATATTTTCATTTGGTTGGGTTA
137 TAATTGCTAAAATCAGGTCTTTACGCGGAATC
138 TCGCCTGCAAAATTAATTACATGTCAATAG
139 TGAGCCATCACCATTACCATTAGCCCCTCAGA
140 TTTTTAAAAATTTTTGTTAAATAGAAGGAG
141 TCATATGTCTCCGTGGGAACAAACTTGGTGTA
142 TTTAAATTCTGGCCTTCCTGTAGCGCCTCAGG
143 GTACAACGATTATACCAAGCGCATACCCAA
144 TTTTAAGGAACCGGATATTCATCTCCATGT
145 ATTTTCATATCGAGAACAAGCAAGACGATAAA
146 TTACAAAAAAAACAGGGAAGCGAAAGTAAG

147
GGGATAGATTTTGCTAAACAACTCCAAAAGGAGCCTTTATCACCCTC

148 CGCTGAGACTTGCTGAACCTCAAAACATTATC

149 ACTTTACAGTTATCTAAAATATCTTCGCCATT

150 ATCTTACCGGCAACATATAAAAGACCGATTGA

151 AAGAGCAGGAATAAGTTTATTTCCAGCGCC

152 CTACAATATTGAGCGCTAATATCCAATAAT

153 TTTCGAGGCAGGGAGTTAAAGGCCCGAAAGAG

154
ATTCAACCTGTTAAAATTCGCATTCCAATAGGAACGCCATCGGCACCG

155 GCCTGAGAGCCTTTATTTCAACGCAGCAATAA

156 AAAGATTAGTACCTTTAATTGCTCAGTTTGAC

157 ATTCGCGTGTAAACGTTAATATTTGTTCTAGC

158 GACGGGCAACAGCTGATTGCCCTAATTGCGT

159 TGCGCTCGGTACCGAGCTCGAACTATTACG

160 GATGGCAATTTAAAAGTTTGAGTATATCAAAC

161 CGATTAAGCATCGTAACCGTGCATAACAACCC

162 ACCAGTAGTTGGGAATTAGAGCCAACAACCAT

163 GCAAAAGACGAAATCCGCGACCTGTACCCAAAT

164 TTGAGGGGGCGAAAGGGGGATGTGCTCTAGAG

165 GGGAGGGACAGTAGCGACAGAATCTCACCGGA

166 ACCGTAATAGGTAAATATTGACGGATACATAC

167 AAGGCAACGAACGAGTAGATTTCTTTTGAT

168 CACAAACACACCACCGGAACCGCCATAGCAGC

169 CCCCCAGCGGAGATTTGTATCATCAGTGAATA

170 GGAGTGTACTGGTAATAAGTTTTAGCCAGAA

171 CGATAGTTGCATAACCGATATATTATCTTTGA

172 CAAGCTTGGCCAGCTGCATTAATGGCGTATTG

173 CAGTATGTCCGAACAAAGTTACCAACAGAGAG

174 AGGAATTACAGAGGGGGTAATAGTTGCATCAA

175 AGCCTCAGTCATTCCATATAACAGTTAGAGCT

176 TAGGTGTATCACCGTACTCAGGAGCCTCAGAA

177 CCACCAGCAAAGGAATTGAGGAAGAACAATTC

178 GAGATAGATCCAGAACAATATTACAGTGTTTT

179 CTTTAGCGAAAGGGCGACATTCAAAACGCAAA

180 AAACGTCAGGTGAATTATCACCGTTTATTACG

181 TAAAACATTAGGAGCACTAACAATTTGAGG

182 AACGGTACGCCAGAATCCTGAGACGCCAGCC

183 CCTAAATTAGAATCCTTGAAAACAGGAAACAG

184 TGAATTTACAAAGAACGCGAGATCTTACCA

185
AGGCGCAGAGAGTAATCTTGACAAAACTGGCTCATTATACGAATACCA

186 CAACTTTAACAAAGCTGCTCATTCGCCTGATA

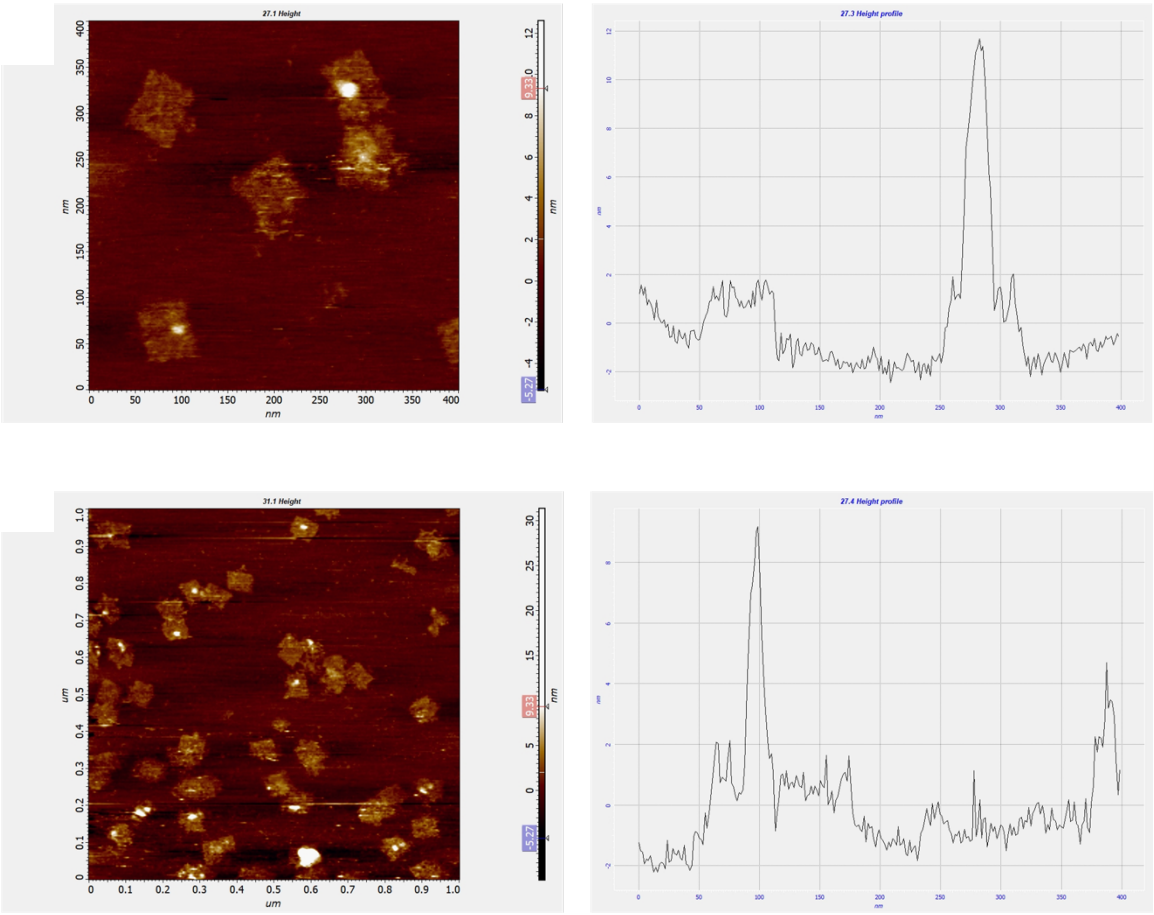

S16.AFM images of annealed QDs on Origami tile in tapping contact mode and the corresponding height profile of the structures

2.7 References

(1) Mansur, H. S. Quantum Dots and Nanocomposites. *WIREs Nanomedicine and Nanobiotechnology* **2010**, *2* (2), 113–129. https://doi.org/10.1002/wnan.78.

(2) Govorov, A. O. Spin and Energy Transfer in Nanocrystals without Tunneling. *Phys. Rev. B* **2003**, *68* (7), 075315. https://doi.org/10.1103/PhysRevB.68.075315.

(3) Raino, G.; Becker, M.; Bodnarchuk, M.; Mahrt, R.; Kovalenko, M.; Stoferle, T. Superfluorescence from Lead Halide Perovskite Quantum Dot Superlattices. *Nature*, 2018, *563*, 671-+. https://doi.org/10.1038/s41586-018-0683-0.

(4) Kagan, C.; Murray, C.; Nirmal, M.; Bawendi, M. Electronic Energy Transfer in CdSe Quantum Dot Solids. *Physical Review Letters*, 1996, *76*, 1517–1520. https://doi.org/10.1103/PhysRevLett.76.1517.

(5) J. W. M. Chon; M. Gu. Use of Quantum Dot Nanocrystals for Spectrally Encoded Optical Data Storage. In *CLEO/Pacific Rim 2003. The 5th Pacific Rim Conference on Lasers and Electro-Optics (IEEE Cat. No.03TH8671)*; 2003; Vol. 1, p 379 Vol.1. https://doi.org/10.1109/CLEOPR.2003.1274831.

(6) Lan, X.; Masala, S.; Sargent, E. Charge-Extraction Strategies for Colloidal Quantum Dot Photovoltaics. *Nature Materials*, 2014, *13*, 233–240. https://doi.org/10.1038/NMAT3816.

(7) Krovi, H. Models of Optical Quantum Computing. *Nanophotonics*, 2017, *6*, 531–541. https://doi.org/10.1515/nanoph-2016-0136.

(8) Du, K.; Ko, S.; Gallatin, G.; Yoon, H.; Liddle, J.; Berglund, A. Quantum Dot-DNA Origami Binding: A Single Particle, 3D, Real-Time Tracking Study. *Chemical Communications*, 2013, *49*, 907–909. https://doi.org/10.1039/c2cc37517f.

(9) Bui, H.; Onodera, C.; Kidwell, C.; Tan, Y.; Graugnard, E.; Kuang, W.; Lee, J.; Knowlton, W.; Yurke, B.; Hughes, W. Programmable Periodicity of Quantum Dot Arrays with DNA Origami Nanotubes. *Nano Letters*, 2010, *10*, 3367–3372. https://doi.org/10.1021/nl101079u.

(10) Huang, D.; Freeley, M.; Palma, M. DNA-Mediated Patterning of Single Quantum Dot Nanoarrays: A Reusable Platform for Single-Molecule Control. *Scientific Reports*, 2017, *7*. https://doi.org/10.1038/srep45591.

(11) Bilan, R.; Nabiev, I.; Sukhanova, A. Quantum Dot-Based Nanotools for Bioimaging, Diagnostics, and Drug Delivery. *ChemBioChem* **2016**, *17* (22), 2103–2114. https://doi.org/10.1002/cbic.201600357.

(12) Medintz, I. L.; Uyeda, H. T.; Goldman, E. R.; Mattoussi, H. Quantum Dot Bioconjugates for Imaging, Labelling and Sensing. *Nature Materials* **2005**, *4* (6), 435–446. https://doi.org/10.1038/nmat1390.

(13) Cheng, Y.; Ling, S. D.; Geng, Y.; Wang, Y.; Xu, J. Microfluidic Synthesis of Quantum Dots and Their Applications in Bio-Sensing and Bio-Imaging. *Nanoscale Adv.* **2021**, *3* (8), 2180–2195. https://doi.org/10.1039/D0NA00933D.

(14) Kho, R.; Torres-Martínez, C. L.; Mehra, R. K. A Simple Colloidal Synthesis for Gram-Quantity Production of Water-Soluble ZnS Nanocrystal Powders. *Journal of Colloid and Interface Science* **2000**, *227* (2), 561–566. https://doi.org/10.1006/jcis.2000.6894.

(15) Rogach, A.; Kershaw, S. V.; Burt, M.; Harrison, M. T.; Kornowski, A.; Eychmüller, A.; Weller, H. Colloidally Prepared HgTe Nanocrystals with Strong Room-Temperature Infrared Luminescence. *Advanced Materials* **1999**, *11* (7), 552–555. https://doi.org/10.1002/(SICI)1521-4095(199905)11:7<552::AID-ADMA552>3.0.CO;2-Q.
(16) Storhoff, J.; Elghanian, R.; Mucic, R.; Mirkin, C.; Letsinger, R. One-Pot Colorimetric Differentiation of Polynucleotides with Single Base Imperfections Using Gold Nanoparticle Probes. *Journal of the American Chemical Society*, 1998, *120*, 1959–1964. https://doi.org/10.1021/ja972332i.
(17) Zhang, Z. H.; Chin, W. S.; Vittal, J. J. Water-Soluble CdS Quantum Dots Prepared from a Refluxing Single Precursor in Aqueous Solution. *J. Phys. Chem. B* **2004**, *108* (48), 18569–18574. https://doi.org/10.1021/jp0470849.
(18) Ding, Y.; Bi, J.; Du, B.; Hu, X.; Liu, F. Aqueous Synthesis of Glutathione Capped ZnSe Nanocrystals: Synthesis and Optical Properties. *Materials Research Innovations*, 2013, *17*, 142–147. https://doi.org/10.1179/1433075X12Y.0000000040.
(19) Liu, H.; Owen, J.; Alivisatos, A. Mechanistic Study of Precursor Evolution in Colloidal Group II-VI Semiconductor Nanocrystal Synthesis. *Journal of the American Chemical Society*, 2007, *129*, 305–312. https://doi.org/10.1021/ja0656696.
(11) Murray, C. B.; Norris, D. J.; Bawendi, M. G. Synthesis and Characterization of Nearly Monodisperse CdE (E = Sulfur, Selenium, Tellurium) Semiconductor Nanocrystallites. *J. Am. Chem. Soc.* **1993**, *115* (19), 8706–8715. https://doi.org/10.1021/ja00072a025.
(21) Yin, Y.; Alivisatos, A. Colloidal Nanocrystal Synthesis and the Organic-Inorganic Interface. *Nature*, 2005, *437*, 664–670. https://doi.org/10.1038/nature04165.
(22) Hines, M.; Guyot-Sionnest, P. Synthesis and Characterization of Strongly Luminescing ZnS-Capped CdSe Nanocrystals. *Journal of Physical Chemistry*, 1996, *100*, 468–471. https://doi.org/10.1021/jp9530562.
(23) Parak, W. J.; Gerion, D.; Zanchet, D.; Woerz, A. S.; Pellegrino, T.; Micheel, C.; Williams, S. C.; Seitz, M.; Bruehl, R. E.; Bryant, Z.; Bustamante, C.; Bertozzi, C. R.; Alivisatos, A. P. Conjugation of DNA to Silanized Colloidal Semiconductor Nanocrystalline Quantum Dots. *Chem. Mater.* **2002**, *14* (5), 2113–2119. https://doi.org/10.1021/cm0107878.
(24) Zhang, C.; Macfarlane, R. J.; Young, K. L.; Choi, C. H. J.; Hao, L.; Auyeung, E.; Liu, G.; Zhou, X.; Mirkin, C. A. A General Approach to DNA-Programmable Atom Equivalents. *Nature Materials* **2013**, *12* (8), 741–746. https://doi.org/10.1038/nmat3647.
(25) Lees, E.; Nguyen, T.; Clayton, A.; Mulvaney, P.; Muir, B. The Preparation of Colloidally Stable, Water-Soluble, Biocompatible, Semiconductor Nanocrystals With a Small Hydrodynamic Diameter. *Acs Nano*, 2009, *3*, 1121–1128. https://doi.org/10.1021/nn900144n.
(26) Lin, C.; Sperling, R.; Li, J.; Yang, T.; Li, P.; Zanella, M.; Chang, W.; Parak, W. Design of an Amphiphilic Polymer for Nanoparticle Coating and Functionalization. *Small*, 2008, *4*, 334–341. https://doi.org/10.1002/smll.200700654.
(27) Uyeda, H.; Medintz, I.; Jaiswal, J.; Simon, S.; Mattoussi, H. Synthesis of Compact Multidentate Ligands to Prepare Stable Hydrophilic Quantum Dot Fluorophores.

Journal of the American Chemical Society, 2005, *127*, 3870–3878. https://doi.org/10.1021/ja044031w.

(28) Medintz, I.; Mattoussi, H. Quantum Dot-Based Resonance Energy Transfer and Its Growing Application in Biology. *Physical Chemistry Chemical Physics*, 2009, *11*, 17–45. https://doi.org/10.1039/b813919a.

(29) Clapp, A.; Medintz, I.; Mauro, J.; Fisher, B.; Bawendi, M.; Mattoussi, H. Fluorescence Resonance Energy Transfer between Quantum Dot Donors and Dye-Labeled Protein Acceptors. *Journal of the American Chemical Society*, 2004, *126*, 301–310. https://doi.org/10.1021/ja037088b.

(30) Clapp, A.; Medintz, I.; Mattoussi, H. Forster Resonance Energy Transfer Investigations Using Quantum-Dot Fluorophores. *Chemphyschem*, 2006, *7*, 47–57. https://doi.org/10.1002/cphc.200500217.

(31) Mitchell, G.; Mirkin, C.; Letsinger, R. Programmed Assembly of DNA Functionalized Quantum Dots. *Journal of the American Chemical Society*, 1999, *121*, 8122–8123. https://doi.org/10.1021/ja991662v.

(32) Sapsford, K.; Algar, W.; Berti, L.; Gemmill, K.; Casey, B.; Oh, E.; Stewart, M.; Medintz, I. Functionalizing Nanoparticles with Biological Molecules: Developing Chemistries That Facilitate Nanotechnology. *Chemical Reviews*, 2013, *113*, 1904–2074. https://doi.org/10.1021/cr300143v.

(33) Shen, H.; Jawaid, A.; Snee, P. Poly(Ethylene Glycol) Carbodiimide Coupling Reagents for the Biological and Chemical Functionalization of Water-Soluble Nanoparticles. *Acs Nano*, 2009, *3*, 915–923. https://doi.org/10.1021/nn800870r.

(34) Diaz, S.; Gillanders, F.; Jares-Erijman, E.; Jovin, T. Photoswitchable Semiconductor Nanocrystals with Self-Regulating Photochromic Forster Resonance Energy Transfer Acceptors. *Nature Communications*, 2015, *6*. https://doi.org/10.1038/ncomms7036.

(35) Toma, M.; Loget, G.; Corn, R. Flexible Teflon Nanocone Array Surfaces with Tunable Superhydrophobicity for Self-Cleaning and Aqueous Droplet Patterning. *Acs Applied Materials & Interfaces*, 2014, *6*, 11110–11117. https://doi.org/10.1021/am500735v.

(36) Macfarlane, R.; Lee, B.; Jones, M.; Harris, N.; Schatz, G.; Mirkin, C. Nanoparticle Superlattice Engineering with DNA. *Science*, 2011, *334*, 204–208. https://doi.org/10.1126/science.1210493.

(37) Samanta, A.; Zhou, Y.; Zou, S.; Yan, H.; Liu, Y. Fluorescence Quenching of Quantum Dots by Gold Nanoparticles: A Potential Long Range Spectroscopic Ruler. *Nano Letters*, 2014, *14*, 5052–5057. https://doi.org/10.1021/nl501709s.

(38) Farlow, J.; Seo, D.; Broaders, K.; Taylor, M.; Gartner, Z.; Jun, Y. Formation of Targeted Monovalent Quantum Dots by Steric Exclusion. *Nature Methods*, 2013, *10*, 1203-+. https://doi.org/10.1038/NMETH.2682.

(39) Shen, J.; Tang, Q.; Li, L.; Li, J.; Zuo, X.; Qu, X.; Pei, H.; Wang, L.; Fan, C. Valence-Engineering of Quantum Dots Using Programmable DNA Scaffolds. *Angewandte Chemie-International Edition*, 2017, *56*, 16077–16081. https://doi.org/10.1002/anie.201710309.

(40) Zhang, T.; Liedl, T. DNA-Based Assembly of Quantum Dots into Dimers and Helices. *Nanomaterials*, 2019, *9*. https://doi.org/10.3390/nano9030339.

(41) Deng, Z.; Samanta, A.; Nangreave, J.; Yan, H.; Liu, Y. Robust DNA-Functionalized Core/Shell Quantum Dots with Fluorescent Emission Spanning from UV-Vis to Near-IR and Compatible with DNA-Directed Self-Assembly. *Journal of the American Chemical Society*, 2012, *134*, 17424–17427. https://doi.org/10.1021/ja3081023.
(42) Samanta, A.; Deng, Z.; Liu, Y. Infrared Emitting Quantum Dots: DNA Conjugation and DNA Origami Directed Self-Assembly. *Nanoscale*, 2014, *6*, 4486–4490. https://doi.org/10.1039/c3nr06578b.
(43) Tikhomirov, G.; Hoogland, S.; Lee, P.; Fischer, A.; Sargent, E.; Kelley, S. DNA-Based Programming of Quantum Dot Valency, Self-Assembly and Luminescence. *Nature Nanotechnology*, 2011, *6*, 485–490. https://doi.org/10.1038/NNANO.2011.100.
(44) Zheng, J.; Constantinou, P.; Micheel, C.; Alivisatos, A.; Kiehl, R.; Seeman, N. Two-Dimensional Nanoparticle Arrays Show the Organizational Power of Robust DNA Motifs. *Nano Letters*, 2006, *6*, 1502–1504. https://doi.org/10.1021/nl060994c.
(45) Kuzyk, A.; Schreiber, R.; Fan, Z.; Pardatscher, G.; Roller, E.; Hogele, A.; Simmel, F.; Govorov, A.; Liedl, T. DNA-Based Self-Assembly of Chiral Plasmonic Nanostructures with Tailored Optical Response. *Nature*, 2012, *483*, 311–314. https://doi.org/10.1038/nature10889.
(46) Ke, Y.; Ong, L.; Sun, W.; Song, J.; Dong, M.; Shih, W.; Yin, P. DNA Brick Crystals with Prescribed Depths. *Nature Chemistry*, 2014, *6*, 994–1002. https://doi.org/10.1038/NCHEM.2083.
(47) Sharma, J.; Chhabra, R.; Cheng, A.; Brownell, J.; Liu, Y.; Yan, H. Control of Self-Assembly of DNA Tubules Through Integration of Gold Nanoparticles. *Science*, 2009, *323*, 112–116. https://doi.org/10.1126/science.1165831.
(48) Park, S.; Lazarides, A.; Storhoff, J.; Pesce, L.; Mirkin, C. The Structural Characterization of Oligonucleotide-Modified Gold Nanoparticle Networks Formed by DNA Hybridization. *Journal of Physical Chemistry B*, 2004, *108*, 12375–12380. https://doi.org/10.1021/jp040242b.
(49) Li, Z.; Cheng, E.; Huang, W.; Zhang, T.; Yang, Z.; Liu, D.; Tang, Z. Improving the Yield of Mono-DNA-Functionalized Gold Nanoparticles through Dual Steric Hindrance. *Journal of the American Chemical Society*, 2011, *133*, 15284–15287. https://doi.org/10.1021/ja205712a.
(50) Hurst, S.; Lytton-Jean, A.; Mirkin, C. Maximizing DNA Loading on a Range of Gold Nanoparticle Sizes. *Analytical Chemistry*, 2006, *78*, 8313–8318. https://doi.org/10.1021/ac0613582.
(51) Levicky, R.; Herne, T.; Tarlov, M.; Satija, S. Using Self-Assembly to Control the Structure of DNA Monolayers on Gold: A Neutron Reflectivity Study. *Journal of the American Chemical Society*, 1998, *120*, 9787–9792. https://doi.org/10.1021/ja981897r.
(52) Demers, L.; Mirkin, C.; Mucic, R.; Reynolds, R.; Letsinger, R.; Elghanian, R.; Viswanadham, G. A Fluorescence-Based Method for Determining the Surface Coverage and Hybridization Efficiency of Thiol-Capped Oligonucleotides Bound to Gold Thin Films and Nanoparticles. *Analytical Chemistry*, 2000, *72*, 5535–5541. https://doi.org/10.1021/ac0006627.

(53) Liu, J.; Lu, Y. Preparation of Aptamer-Linked Gold Nanoparticle Purple Aggregates for Colorimetric Sensing of Analytes. *Nature Protocols*, 2006, *1*, 246–252. https://doi.org/10.1038/nprot.2006.38.
(54) Hill, H.; Millstone, J.; Banholzer, M.; Mirkin, C. The Role Radius of Curvature Plays in Thiolated Oligonucleotide Loading on Gold Nanoparticles. *Acs Nano*, 2009, *3*, 418–424. https://doi.org/10.1021/nn800726e.
(55) Herdt, A.; Drawz, S.; Kang, Y.; Taton, T. DNA Dissociation and Degradation at Gold Nanoparticle Surfaces. *Colloids and Surfaces B-Biointerfaces*, 2006, *51*, 130–139. https://doi.org/10.1016/j.colsurfb.2006.06.006.
(56) Bhatt, N.; Huang, P.; Dave, N.; Liu, J. Dissociation and Degradation of Thiol-Modified DNA on Gold Nanoparticles in Aqueous and Organic Solvents. *Langmuir*, 2011, *27*, 6132–6137. https://doi.org/10.1021/la200241d.
(57) Sun, D.; Gang, O. Binary Heterogeneous Superlattices Assembled from Quantum Dots and Gold Nanoparticles with DNA. *Journal of the American Chemical Society*, 2011, *133*, 5252–5254. https://doi.org/10.1021/ja111542t.
(58) Camunas-Soler, J.; Ribezzi-Crivellari, M.; Ritort, F. Elastic Properties of Nucleic Acids by Single-Molecule Force Spectroscopy. *Annual Review of Biophysics* **2016**, *45* (1), 65–84. https://doi.org/10.1146/annurev-biophys-062215-011158.
(59) Pal, S.; Deng, Z.; Ding, B.; Yan, H.; Liu, Y. DNA-Origami-Directed Self-Assembly of Discrete Silver-Nanoparticle Architectures. *Angewandte Chemie International Edition* **2010**, *49* (15), 2700–2704. https://doi.org/10.1002/anie.201000330.
(60) Julin, S.; Nummelin, S.; Kostiainen, M. A.; Linko, V. DNA Nanostructure-Directed Assembly of Metal Nanoparticle Superlattices. *Journal of Nanoparticle Research* **2018**, *20* (5), 119. https://doi.org/10.1007/s11051-018-4225-3.
(61) Zhu, C.; Wang, M.; Dong, J.; Zhou, C.; Wang, Q. Modular Assembly of Plasmonic Nanoparticles Assisted by DNA Origami. *Langmuir* **2018**, *34* (49), 14963–14968. https://doi.org/10.1021/acs.langmuir.8b01933.
(62) Kim, J. K.; Lim, S. H.; Lee, Y.; Shin, Y. S.; Chung, C.; Yoo, J. Y.; Chang, J. K.; Corp, D. Conjugation of DNA to Streptavidin-Coated Quantum Dots for the Real-Time Imaging of Gene Transfer into Live Cells; 2004.
(63) Wang, R.; Nuckolls, C.; Wind, S. J. Assembly of Heterogeneous Functional Nanomaterials on DNA Origami Scaffolds. *Angewandte Chemie International Edition* **2012**, *51* (45), 11325–11327. https://doi.org/10.1002/anie.201206389.
(64) Ko, S. H.; Gallatin, G. M.; Liddle, J. A. Nanomanufacturing with DNA Origami: Factors Affecting the Kinetics and Yield of Quantum Dot Binding. *Advanced Functional Materials* **2012**, *22* (5), 1015–1023. https://doi.org/10.1002/adfm.201102077.
(65) Bui, H.; Onodera, C.; Kidwell, C.; Tan, Y.; Graugnard, E.; Kuang, W.; Lee, J.; Knowlton, W. B.; Yurke, B.; Hughes, W. L. Programmable Periodicity of Quantum Dot Arrays with DNA Origami Nanotubes. *Nano Lett.* **2010**, *10* (9), 3367–3372. https://doi.org/10.1021/nl101079u.
(66) Sharma, J.; Ke, Y.; Lin, C.; Chhabra, R.; Wang, Q.; Nangreave, J.; Liu, Y.; Yan, H. DNA-Tile-Directed Self-Assembly of Quantum Dots into Two-Dimensional Nanopatterns. *Angew Chem Int Ed Engl* **2008**, *47* (28), 5157–5159. https://doi.org/10.1002/anie.200801485.

(67) Shaw, A.; Benson, E.; Högberg, B. Purification of Functionalized DNA Origami Nanostructures. *ACS Nano* **2015**, *9* (5), 4968–4975. https://doi.org/10.1021/nn507035g.
(68) Lakowicz, J. R. *Principles of Fluorescence Spectroscopy*, 3rd ed.; Springer New York, NY.
(69) Wang, W.; Guo, Y.; Tiede, C.; Chen, S.; Kopytynski, M.; Kong, Y.; Kulak, A.; Tomlinson, D.; Chen, R.; McPherson, M.; Zhou, D. Ultraefficient Cap-Exchange Protocol To Compact Biofunctional Quantum Dots for Sensitive Ratiometric Biosensing and Cell Imaging. *ACS Appl. Mater. Interfaces* **2017**, *9* (18), 15232–15244. https://doi.org/10.1021/acsami.6b13807.
(70) Douglas, S.; Marblestone, A.; Teerapittayanon, S.; Vazquez, A.; Church, G.; Shih, W. Rapid Prototyping of 3D DNA-Origami Shapes with CaDNAno. *Nucleic Acids Research*, 2009, *37*, 5001–5006. https://doi.org/10.1093/nar/gkp436.
(71) Rothemund, P. Folding DNA to Create Nanoscale Shapes and Patterns. *Nature*, 2006, *440*, 297–302. https://doi.org/10.1038/nature04586.
(72) Li, F.; Zhang, H.; Dever, B.; Li, X.-F.; Le, X. C. Thermal Stability of DNA Functionalized Gold Nanoparticles. *Bioconjugate Chem.* **2013**, *24* (11), 1790–1797. https://doi.org/10.1021/bc300687z.
(73) Li, Y.; Shen, B.; Liu, L.; Xu, H.; Zhong, X. Stable Water-Soluble Quantum Dots Capped by Poly(Ethylene Glycol) Modified Dithiocarbamate. *Colloids and Surfaces A: Physicochemical and Engineering Aspects* **2012**, *410*, 144–152. https://doi.org/10.1016/j.colsurfa.2012.06.034.
(74) Hildebrandt, N.; Spillmann, C. M.; Algar, W. R.; Pons, T.; Stewart, M. H.; Oh, E.; Susumu, K.; Díaz, S. A.; Delehanty, J. B.; Medintz, I. L. Energy Transfer with Semiconductor Quantum Dot Bioconjugates: A Versatile Platform for Biosensing, Energy Harvesting, and Other Developing Applications. *Chem. Rev.* **2017**, *117* (2), 536–711. https://doi.org/10.1021/acs.chemrev.6b00030.
(75) Srinivas, N.; Ouldridge, T. E.; Sulc, P.; Schaeffer, J. M.; Yurke, B.; Louis, A. A.; Doye, J. P. K.; Winfree, E. On the Biophysics and Kinetics of Toehold-Mediated DNA Strand Displacement. *Nucleic Acids Res* **2013**, *41* (22), 10641–10658. https://doi.org/10.1093/nar/gkt801.
(76) Sharma, J.; Chhabra, R.; Andersen, C. S.; Gothelf, K. V.; Yan, H.; Liu, Y. Toward Reliable Gold Nanoparticle Patterning On Self-Assembled DNA Nanoscaffold. *J. Am. Chem. Soc.* **2008**, *130* (25), 7820–7821. https://doi.org/10.1021/ja802853r.
(77) Macfarlane Robert J.; Lee Byeongdu; Jones Matthew R.; Harris Nadine; Schatz George C.; Mirkin Chad A. Nanoparticle Superlattice Engineering with DNA. *Science* **2011**, *334* (6053), 204–208. https://doi.org/10.1126/science.1210493.

Chapter 3:

Nanoparticle-heterodimer-based DNA biosensors

3.1 Abstract

Identification of numerous biomarkers, such as tumors, genetic mutations, bacteria, and viruses, is a prerequisite for biotechnical applications and point-of-care diagnosis. Nucleic acids that contain the genetic code for all forms of life can be used as biomarkers for the detection of pathogens, infectious diseases, cancers, and hereditary diseases. As a result, different methods have been developed for the detection and analysis of nucleic acid biomarkers. [2] Even though methods such as polymerase chain reaction (PCR), fluorometric analysis, gel electrophoresis, and UV-Vis are powerful, sensitive, and robust for nucleic acid detection, they often require complicated sample preparations requiring extensive training and expensive equipment. Recent developments in DNA nanotechnology have offered various strategies and principles for detection applications. DNA nanotechnology not only provides nucleic acid detection with high sensitivity and specificity but is also amenable to programmability.

Here I show how quantum dot (QD)-Au heterodimers, self-assembled on the 2D DNA origami surface, could serve as a Förster resonance energy transfer-based DNA origami biosensor for nucleic acid detection. In order to have an efficient interparticle interaction, I designed a center-to-center distance of 20±2 nm and used a simple toehold-mediated strand displacement strategy to enhance the detection. My preliminary results show that at a 430 nM concentration of the target DNA strand, the displacement of Au nanoparticles could cause up to a 38% quantum dot fluorescence increase. The kinetic measurement further demonstrates that the displacement approaches completion in about 25 minutes. These results suggest that the detection of nucleic acids and possibly other biomarkers could be accomplished using this straightforward methodology.

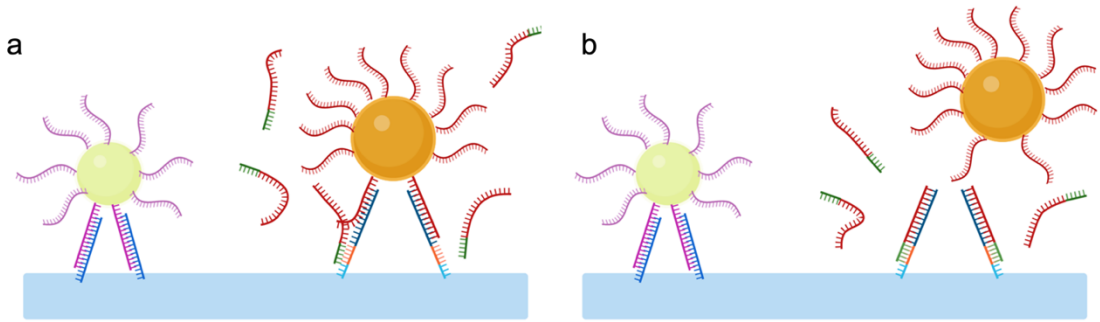

Figure 24.QD-AuNP heterodimers as a DNA biosensor. Addition of the invader strand with a toehold design could displace the AuNP which is then detected by an increase in the PL signal of Quantum dots.

3.2 Introduction

Critical factors that yield the best clinical outcomes in general public health, particularly in the present COVID-19 pandemic, include rapid diagnosis with high sensitivity and specificity for a particular biomarker and timely initiation of appropriate treatment. [3] Conventional *in vitro* detection techniques for infectious diseases such as polymerase chain reaction (PCR),[4] microarrays based on DNA chips, [5] and enzyme-linked immunosorbent assay (ELISA), [6] necessitate complex instrumentation, professionally trained personnel, complex and lengthy sample preparation, and complicated manufacturing processes. The potential for point-of-care diagnostics to match or exceed conventional standards in terms of speed, accuracy, and cost has been increased by recent advancements in biosensor technology that obviate the need for complex instrumentation and sample preparation. New biosensors include varied sensing techniques, such as optical, electrical, and mechanical transducers, as well as micro- and nanofabrication technologies. Despite the significant potential of biosensors, the translation of biosensors from research labs to clinical applications has only been possible in a few significant cases, such as the glucose sensor and recently developed COVID-19 antibody-based tests.[3] To create commercially viable biosensors, a mechanism for providing accurate quantitative measurement of a selective binding event must be developed. This mechanism entails designing a selective binding agent and incorporating it into a device. This process is challenging when taking binding activity into account, especially when dealing with complex matrices, which may cause inaccuracy and low specificity. Another challenge is achieving high sensitivity, long-term stability, rapid detection, and high reproducibility with the sensor, the former being hampered by batch-to-batch variations that occurred during the sensor's manufacturing.

A biosensor consists of a receptor (or recognition component) and a transducing component. The recognition component or receptor is typically an enzyme, antibody, aptamer, or nucleic acid that can bind to or react with the target analyte. The transducing component is typically a material that is responsible for converting the recognition event into detectable signals, such as electrical, optical, or mass signals. Rapid detection, selectivity for the target molecule, sensitivity, and the limit of detection are key factors that determine the performance of the biosensor. The main function of a recognition component is to provide rapid detection and analyte selectivity for a biosensor. To achieve high sensitivity and selectivity, the recognition element must have a high and specific affinity for the target analyte. The extent of binding in a DNA biosensor can be described by the law of mass action, which relates the concentrations of the probe and target to the concentration of the probe-target complex. [7, 8] The law of mass action is expressed mathematically as:

$$[\text{probe-target complex}] = \left(\frac{K_a[\text{probe}][\text{target}]}{1+K_a[\text{probe}]+ K_a[\text{target}]}\right) \quad (1)$$

where [probe] and [target] are the concentrations of the probe and target, and K_a is the association constant for the binding reaction between the probe and its target. This

equation shows that the extent of binding depends on the concentrations of the probe and target, as well as the value of the K_a constant. At low concentrations of either the probe or target, the binding is limited by the availability of the other component, and increasing the concentration of the limiting component can increase the amount of binding. At high concentrations of both the probe and target, the binding may become saturated and reach a maximum value. The K_a constant is an intrinsic property of the binding interaction between the probe and its target in a DNA biosensor and is independent of the concentration of the probe and target. It is determined by the rates of association (k_{on}) and dissociation (k_{off}) of the probe and target molecules and reflects the strength of the binding interaction. [8]

$$K_a = \frac{k_{on}}{k_{off}} \qquad (2)$$

Detection time is determined by the kinetics of analyte-recognition element interactions. On the other hand, the sensitivity and limit of detection of the biosensor are also determined by the binding affinity as well as the ability of the transducer materials to convert the binding events into a measurable signal that can be used to quantify the concentration of the target analyte in the sample.

In an affinity sensor, a probe molecule is used to selectively capture a target molecule, such as a protein or DNA sequence, from a complex biological sample. When the probe and target molecules bind to each other, they form a stable complex that can be detected using a signal transduction mechanism, such as fluorescence, electrochemistry, or mass spectrometry. The concentration of the target-probe complex (C_{TP}) is directly proportional to the amount of binding that occurs between the probe and target molecules and can be quantified using various analytical methods. The signal transduction factor (T_F) represents the efficiency of the signal transduction mechanism and the detection instrument used to convert the presence of the target-probe complex into a measurable signal, such as a voltage or a wavelength of light. The following equation represents the relationship between the signal intensity (I) of an affinity sensor, the concentration of the target-probe complex (C_{TP}), and the signal transduction factor (T_F), which depends on the material used for signal transduction and the instrument used to detect the signal.

$$I = C_{TP} \times T_F \qquad (3)$$

The product of C_{TP} and T_F represents the signal intensity (I) of the affinity sensor, which measures the strength of the binding interaction between the probe and target molecules as well as the sensitivity and selectivity of the signal transduction mechanism and detection instrument used. By optimizing the probe design, binding conditions, and signal transduction mechanism, the signal intensity of an affinity sensor can be maximized, leading to improved sensitivity and accuracy in detecting target molecules in complex biological samples.

The sensitivity of an affinity biosensor can be defined as the ratio of the change in signal intensity (ΔI) to the change in the concentration of the target molecule (ΔC_T).[9, 10] Mathematically, this can be expressed as:

$$\text{Sensitivity} = \Delta I / \Delta C_T \quad (4)$$

The limit of detection (LOD) is the lowest concentration of the target molecule that can be reliably detected above the noise level (s) of the sensor. A common criterion for LOD is a signal intensity that is three times higher than the noise level. Mathematically, the LOD can be expressed as:

$$\text{LOD} = 3 \times \text{noise level} / \text{sensitivity} \quad (5)$$

where the noise level is the standard deviation of the signal intensity measured in the absence of the target molecule, and the sensitivity is as defined above. This equation shows that the LOD is inversely proportional to the sensitivity of the sensor and can be improved by increasing the sensitivity or reducing the noise level of the sensor. By optimizing the probe design, binding conditions, and signal transduction mechanism, the sensitivity and LOD of an affinity biosensor can be improved, leading to more accurate and reliable detection of target molecules in complex biological samples. [9-11]

As previously indicated, there are several types of recognition components, ranging from synthetic constructs like molecularly imprinted polymers (MIPs) to naturally occurring structures like enzymes, antibodies, aptamers, and deoxyribonucleic acids (DNA).

3.2.1 Molecular recognition in DNA biosensors

DNA has a number of advantages over biosensors built with enzymes or antibodies as the recognition element, including superior specificity through Watson-Crick base pairing, ease of modification, thermal stability, and stable chemistry. [12-17] In comparison to a typical antibody-based sensor, a longer lifetime and cheaper production costs are attained when DNA is employed as the molecular recognition component. [18] By incorporating DNA as the recognition element, different types of DNA biosensors, such as aptamer-based, [19] DNAzyme-based, and [20] DNA hybridization-based biosensors (Figure 2), have been developed, and [21, 22,] depending on the type of DNA recognition element, they can detect a wide range of target molecules, including metal ions, nucleic acids, proteins, and small biological organisms. [19, 23-26]

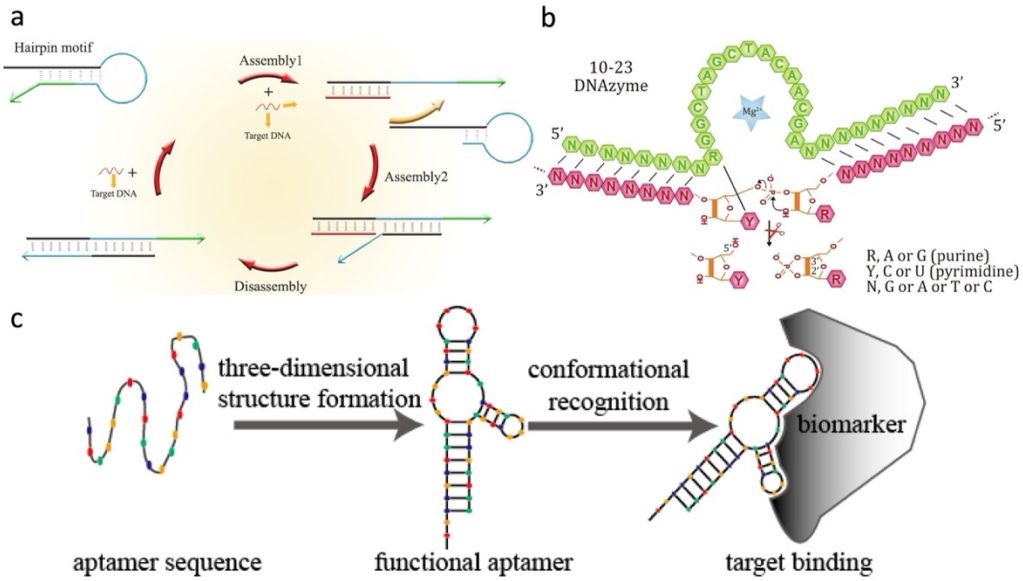

Figure 25.hybridization-based, DNAzyme-based and Aptamer-based DNA biosensors. [27-29]

Biosensors based on DNA hybridization make use of the complementary DNA binding domain to obtain analyte selectivity. An artificially created DNA fragment can be immobilized at the receptor site as a recognition component once a target sequence has been determined. [29–31] By using a special complementary recognition mechanism between the target sequence and the immobilized DNA fragment, selectivity is obtained. Recent advancements in the application of nucleic acid recognition elements include the utilization of DNA hairpins, peptide nucleic acids (PNA), and locked nucleic acids (LNA) (Figure 3).

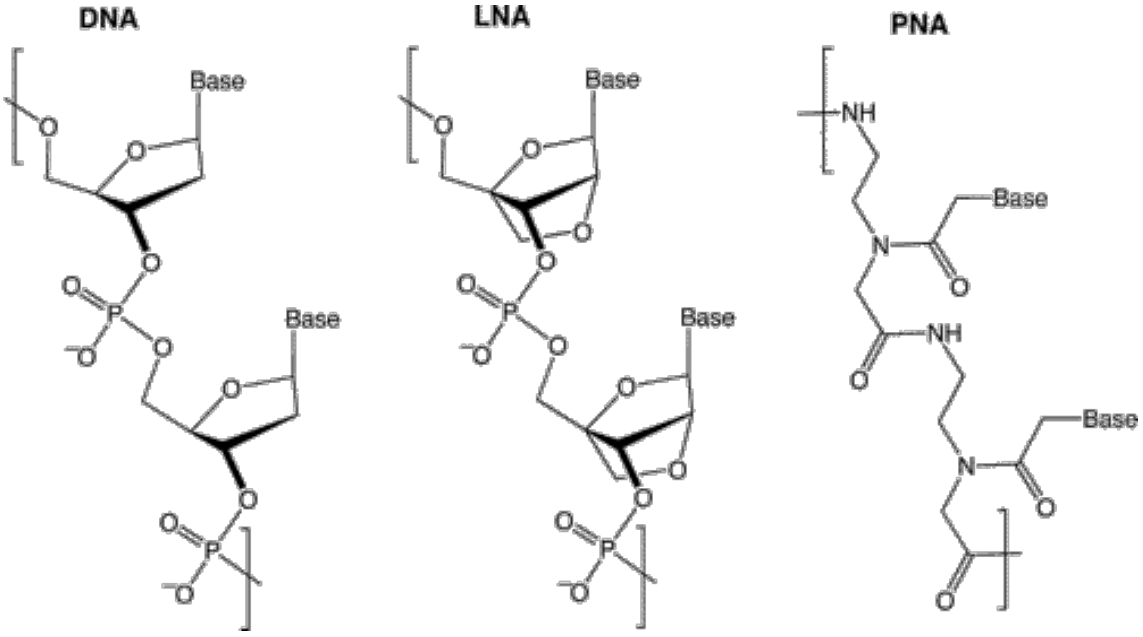

Figure 26.Molecular structure of DNA, LNA and PNA. [29]

Locked nucleic acid is made of a bicyclic furanose unit that is bound in a sugar structure that mimics RNA. The methylene bridge that joins the 2'-oxygen and 4'-carbon of the ribose ring and locks the ribose in the "3'-endo" state gives the LNA base pair a more solid structure, consequently enhancing the binding with the complementary target DNA. [30] Additionally, since LNAs have an RNA-like structure, they have enhanced binding affinity and selectivity for target sequences when compared with DNA. [31] Aside from their low background signal and great thermostability, LNA bases also show effective target hybridization and strong resistance to degradation. [32, 33] These characteristics often enable the construction of LNA-based biosensors for miRNA profiling with enhanced sensitivity and specificity. [34, 35] Despite these benefits of LNA biosensors, further development is still required to obtain hybridization kinetics and faster detection. [36]

The recognition component in a hairpin-based DNA biosensor is defined by its single-stranded DNA having self-complementary characteristics and the ability to fold into a stem loop. [37] In general, hairpins produce two major open and closed configurations. [38] The stem loop hairpin DNA probe also has a high degree of hybridization selectivity and exceptional specificity for the target molecules, including DNA and small molecules. [39] The DNA-hairpin-based probe has been shown to have a limit of detection (LOD) in the picomolar range for detecting target nucleic acid fragments. [40, 41] Peptide nucleic acid, also known as PNA, is a synthetic oligonucleotide that is made up of a repeating aminoethyl-glycine subunit bound through amide bonds. Due to their neutral charge and peptide-like backbones, PNAs are not prone to digestion by nucleases and proteases and have a higher degree of stability throughout the process of nucleic acid binding compared to DNA. [42, 43] In general, the range of applications for nucleic acid recognition components is highly restricted due to the fact that their utilization is optimized primarily for biosensor applications that specifically target nucleic acids.

Another class of DNA biosensors use aptamers as the recognition element, which entails the capability to detect a wider spectrum of analytes such as metal ions, proteins, whole cells, and small molecules. [44, 45] Aptamers are single-stranded RNA or DNA molecules that can bind to a specific target molecule with high affinity and specificity, similar to antibodies. SELEX (Systematic Evolution of Ligands by Exponential Enrichment) is a process used to identify and isolate aptamers from a large pool of random RNA or DNA sequences. The SELEX process involves several rounds of selection and amplification, where the aptamers that bind most strongly to the target molecule are enriched and amplified for further selection. This process continues until a sufficient number of aptamers with high affinity and specificity for the target have been obtained. Aptamers are approximately 100 base pairs long, with a fixed primer binding site at both ends and a 20–70 randomized base pair binding zone in the middle. In an aptamer-based DNA biosensor, the aptamer is designed to bind specifically to a target molecule, and the binding event is then used to trigger a signal output. [46, 47] This signal can be generated by a variety of mechanisms, including changes in fluorescence, color, or an electrochemical signal.

Aptamers have several advantages as recognition elements in biosensors. They have a high specificity and affinity for their target, ease of production and modification, and the ability to be easily functionalized with detection moieties. Additionally, aptamers can be designed to bind a wide range of target molecules, including small molecules, proteins, and RNA, making them suitable for a variety of applications. Aptamer-based DNA biosensors have been used in a number of applications, including medical diagnostics, environmental monitoring, and food safety testing. They have the potential to be used in point-of-care testing and in resource-limited settings due to their simple and low-cost nature. [44, 48]

Lastly, DNA biosensors could utilize a DNAzyme serving as the recognition element to detect the presence of specific target molecules. [20, 24] A DNazyme is a type of artificial nuclease created from a DNA molecule. Unlike natural nucleases, which are enzymes made from proteins, DNazymes are constructed from synthetic DNA molecules that have been engineered to have nuclease activity. DNazymes are commonly used in molecular biology research as tools for cleaving DNA molecules at specific sites, for example, to create deletions or modifications in a gene. In a DNAzyme biosensor, the DNAzyme is designed to cleave a reporter substrate (such as a fluorescent or colorimetric dye) in the presence of the target molecule. [23, 28, 49] The cleavage of the substrate results in a change in the fluorescence or color of the biosensor, which is proportional to the amount of target present in the sample. The high specificity of DNAzymes allows them to be used to detect DNA and RNA molecules. DNAzyme biosensors have numerous potential applications, including environmental monitoring, medical diagnostics, and food safety testing. [24, 28]

All three of these distinct categories of DNA-based recognition elements have their own advantages and limitations, and the choice between them often depends on the specific application and the requirements for sensitivity, specificity, and versatility. For instance, the great selectivity of hybridization-based DNA biosensors for nucleic acid targets with complementary sequence precludes their use for other types of analytes. On the other hand,

aptamer-based DNA biosensors have higher flexibility and can be easily modified to target a wide range of different molecules, including proteins, small molecules, and even live cells. In contrast to enzyme-based DNA biosensors, which may be chosen for applications requiring the degradation of the target molecule, aptamer-based biosensors may also be advantageous for uses requiring great specificity.

These DNA-based recognition elements, or probes, typically need to be immobilized onto a material such as a flat substrate or nanomaterial that can help transduce the recognition events into signals. In addition, surface immobilization allows the placement of different recognition elements in a spatial pattern, enabling the detection of multiple target molecules simultaneously and making them suitable for complex assays and large-scale screening applications. The spatial organization of recognition elements also enables the creation of multiple probe-target interaction sites, which can amplify the signal generated by each interaction and enhance the overall signal transduction. [50-52]

An emerging promising approach to incorporating these recognition elements is to anchor them on a self-assembled DNA nanostructure with spatially addressable binding sites. One of the most prominent examples of such DNA templates is DNA origami. The programmability and design flexibility of DNA origami structures allow for the creation of biosensors with a wide range of shapes, sizes, and recognition elements, enabling the detection of a wide variety of targets. Additionally, these structures can incorporate precise mechanisms for enhanced signal transduction. Overall, the ability to precisely control the arrangement of recognition elements on the DNA origami structure can significantly enhance the performance and versatility of these biosensors. The next section will provide background on self-assembled DNA templates in biosensing.

3.2.2 DNA template and DNA origami-based biosensors

As nanotechnology advances, DNA is being seen as a vital material capable of building a range of programmable structures. The capacity of DNA to fold into various shapes, along with its exceptional programmability and selectivity of DNA hybridization [33] make DNA a unique candidate for creating highly precise nanoscale structures. These shapes can act as scaffolds to spatially organize recognition elements with sub-nanometer precision for capturing target analytes and become configured for optimal target binding. These structures can serve as a blueprint for the development of a new class of e biosensors called DNA-template-based biosensors with programmable anchoring. [53, 54] The recognition element in a DNA-template-based biosensor could be anything from small molecules, enzymes, and peptides to aptamers and single-stranded DNA probes. The signal output is then initiated by the binding event between the target molecule and the recognition element. The signal can be generated by a variety of mechanisms, including changes in fluorescence, color, or an electrochemical signal.

DNA-template biosensors have several advantages, including high specificity and sensitivity, the ability to be easily functionalized with detection moieties, and the ability to be easily modified to detect a wide range of target molecules. A variety of DNA-template biosensors have been successfully made using DNA tetrahedrons, lattices, and crossover

tiles. Their versatility in size, relatively high stiffness, the ability to create custom nanoscale shapes, and the use of addressable anchoring points to position DNA probes and functional nanomaterials make them a great candidate for a biosensor design. [22, 55] Several studies using DNA tetrahedron sensors using optical methods, [56, 57] electrochemical, [58, 59] and SPR sensing [60, 61] have been published. Compared to traditional DNA biosensors that immobilize DNA probes onto a solid support, the density management of the recognition element on the sensor surface could be improved using a DNA template biosensor to improve biosensing performance. [2, 62] Additionally, the DNA templates, such as DNA tetrahedrons, are known to be more resistant to enzyme degradation, extending their lifespan in tissues and organisms. [63,64] Although a variety of DNA template-based biosensors, including DNA tiles, can be widely used in biosensors for in vitro and in vivo clinical diagnostics, the production of more complex DNA tile-based patterns necessitates a time-consuming predesign procedure and a high level of experimental operation, restricting the usage of DNA tiles in biosensors. Therefore, a more robust, effective, and widely applicable DNA assembly approach is required to make more versatile DNA template biosensors. The DNA origami technique that was invented by Paul Rothemund provides a solution to this issue [48] by enabling the construction of complex architectures. The main premise of DNA origami is to use the raster fill technique to turn folded single-strand DNA (scaffold DNA) into well-defined patterns. Through ssDNA extension or functionalization in DNA nanostructures, target molecules (specific biological receptors, functional materials, or signal-reporting molecules) can be precisely anchored to predefined locations. With the help of this arrangement capability, the distribution of biological probes on the biosensor surface can be adjusted, and new biosensors can be created.

The recognition element in DNA origami biosensors can take many different forms, much as in other biosensors, including antibodies, peptides, enzymes, small molecules, DNAzymes, functionalized aptamers, or DNA strands made specifically to bind to the target molecule. These recognition elements are often incorporated into the DNA origami structure through specific binding interactions between the recognition element and DNA sequences. The precise arrangement of recognition elements on the DNA origami structure can be carefully controlled to enhance their specificity and sensitivity toward the target molecule. [55, 65] The binding of the target molecule to the recognition element results in a change in the conformation or stability of the DNA origami structure, which can be detected by the signal output. The signal strength may be carefully controlled in a DNA origami biosensor by altering the structure's rigidity, size, and the distance between recognition elements. [66]

The signal output in a DNA-origami-based biosensor can be generated by a variety of mechanisms, including changes in optical, color, mechanical, or electrochemical signals. [22, 54, 55] For example, optical-based signal outputs can be achieved by incorporating a fluorescent molecule into the DNA origami structure and measuring changes in fluorescence intensity upon binding of the target molecule. Similarly, changes in color can be achieved by incorporating a pH-sensitive dye into the DNA origami structure and measuring changes in color as the pH changes in response to the binding of the target molecule. [67] Overall, the signal transduction mechanism in DNA-origami-based biosensors

is designed to detect changes in the physical or chemical properties of the DNA-origami structure in response to the binding of a target molecule and to generate a signal output that can be easily measured and interpreted. There are several high-performance DNA origami-based biosensors currently available, with enzyme-assisted biosensors with high catalytic activity, 3D reconfigurable plasmonic biosensors, and optical nanoantenna for single-molecule detection being only a few examples. [68-70]

Optical DNA origami biosensors, which use fluorescent or plasmonic components as the transducer to generate an optical signal, are quickly evolving into fast, sensitive, and multi-target sensing devices with significant potential for biomedical applications. [68, 71, 72] Most of the currently available fluorescent-based optical DNA origami biosensors utilize organic fluorophore dyes such as cyanine, fluorescein, or alexa, and fluorescence quenchers [73] as signal transducers and work based on turn-on (direct fluorescence emission), turn-off (fluorescence quenching), or pairwise fluorescence interactions (Förster resonance energy transfer) mechanisms. [74-76] Although these biosensors have been successfully made with sub-nanomolar limits of detection and fast response, one factor that limits their application, performance, stability, and dynamic range is the use of organic dyes with inherent low intensity and poor photostability properties. [77]

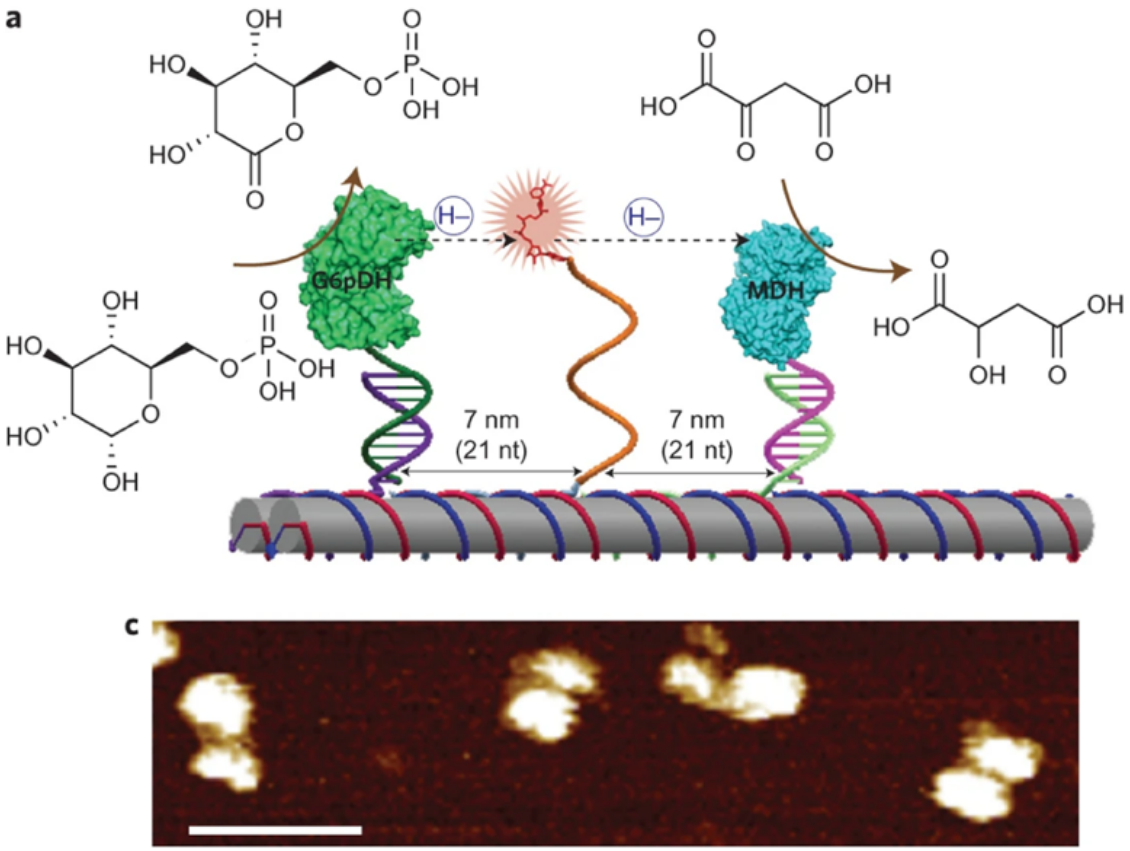

Figure 27. Diagram of the G6pDH and MDH nanostructured complex arranged on a DNA DX tile. The transfer of hydrides is facilitated by the single-stranded poly(T)20 modified by NAD+ that is sandwiched between the two enzymes. [1]

Quantum dots (QDs), on the other hand, are remarkable fluorochromes with 10–20 times higher intensity and superior photostability [78, 79] compared to organic dyes. Therefore, QDs, with their superior photophysical properties, and DNA origami, with its ability to arrange recognition elements and nanomaterials with subnanometer precision, could be an ideal combination for the next generation of optical biosensors, especially those that are based on Förster resonance energy transfer (FRET). However, to this date, there have been few demonstrations of biosensors that rely on this combination. A key barrier to making such biosensors had been the paucity of versatile, easy, and robust methods to produce DNA functionalized nanoparticles with small enough sizes such that they could be placed on DNA origami within a short distance of 10–20 nm, required for FRET. In the preceding chapter, I demonstrated that 1. compact, stable, and emissive QD-DNA conjugates can be prepared using our recently developed single-step ligand exchange method, 2. a QD-DNA conjugate and a DNA functionalized gold nanoparticle can bind to a DNA origami template to form a heterodimer with a tailored distance, and 3. significant energy transfer takes place within the heterotrimer. Here we are exploring the potential of this DNA-template heterodimer as a FRET-based DNA origami biosensor for nucleic acid detection.

In this biosensor design, the analyte is captured using a nucleic acid capture strand as a recognition element. Because the AuNP binds to the DNA origami via hybridization between its ligands and capture strands, the binding of target molecules to the capture strands displaces the AuNP. Without the quencher AuNP in proximity, the fluorescence from the QD is increased. Thus, the binding of target molecules leads to a change in the fluorescence signal. To study the feasibility of this biosensor design, we first created a FRET-compatible interparticle spacing between the AuNP and QDs of around 20 nm for effective interaction. [80] This configuration of DNA origami could result in a fluorescence transducer that relies on energy transfer between AuNP and QD. The QD fluorescence could then be converted to a quantified signal as a result of the capture or displacement of the AuNP on the origami. Secondly, to ensure that the nanoparticles bind to the origami with a high yield, we introduced three capture strands per nanoparticle for each binding site. Lastly, a signal amplification strategy called "Toehold-mediated strand displacement" (TMSD) was incorporated in this design to enhance the molecular recognition and augment the signal; this strategy will be covered in more detail in the following section.

According to our findings, the designer heterodimer was able to successfully detect the target DNA strand at a concentration of 430 nM. The displacement of Au nanoparticles was able to induce a quantum dot fluorescence rise of up to 38%. A further demonstration of this is provided by the kinetic measurement, which shows that the displacement will be nearly finished in around 25 minutes. These findings suggest that the DNA templated heterodimer may serve as a versatile platform the detection of nucleic acids and possibly other biomarkers.

3.2.3 Toehold mediated strand displacement strategy

Toeholds are the short, sticky ends of a DNA strand that are generally used to initiate strand displacement and have been found to have exceptional tunability at both the kinetic and thermodynamic phases. Strand displacement processes have been widely exploited in DNA nanotechnology for the creation of reconfigurable structures, DNA machines, and biosensors. [81-86] Strand displacement reactions provide far more design and operational flexibility than conventional nucleic acid hybridization probes, such as molecular beacons. The basic principle of toehold strand displacement is to use a short "toehold" strand to displace a longer complementary strand, thereby causing a change in the overall hybridization pattern of the DNA biosensor. The development of DNA molecular tweezers marked the introduction of toehold-mediated strand displacement. Here, the toehold served as the starting point for toehold-mediated strand displacement, which was followed by a branch migration process that mimicked a random walk. [87] This process is thermodynamically more advantageous as more base pairs are produced, and the length and order of the toehold domain dominate the kinetics of strand displacement when the hybrid domain is short. [88]

Overall, toehold strand displacement can improve the signal in DNA biosensors by amplifying the response to target molecules, leading to increased sensitivity and specificity in the detection of target molecules. [89] To further enhance the functionality of the biosensor, this strategy was incorporated into the DNA origami design to control and optimize the

interaction between the probes and target molecules, leading to increased sensitivity of the biosensor. The use of toeholds in DNA origami can also enable the creation of multiple probe-target interaction sites, which can amplify the signal generated by each interaction and enhance the overall signal transduction. This can further increase the sensitivity of the biosensor, making it capable of detecting target molecules at lower concentrations.

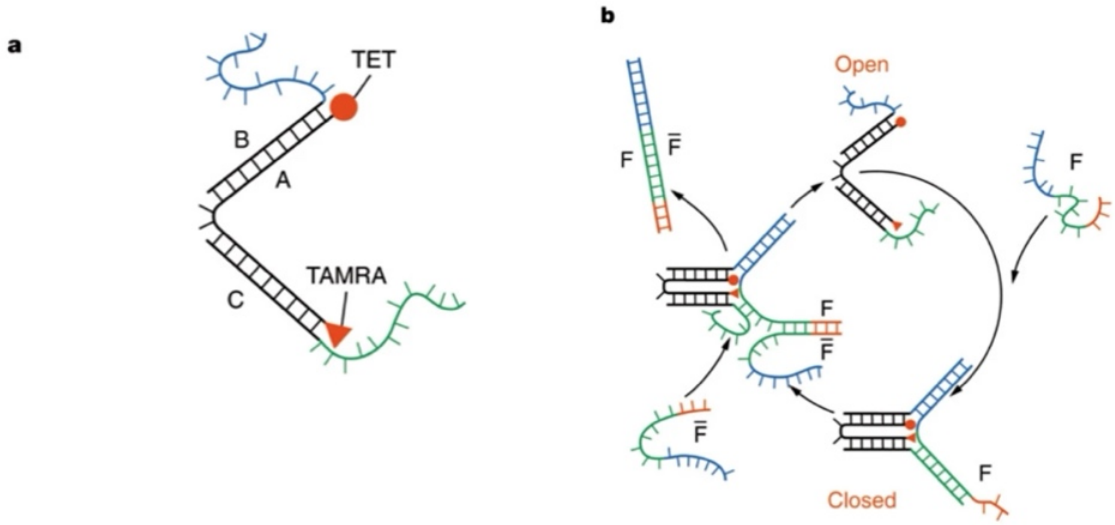

Figure 28. a) An oligonucleotide tweezer structure created by the hybridization of strands A, B, and C. b) Using the molecular tweezers to close and open them. To shut the tweezers, closing strand F forms a hybrid with the free ends of strands B and C (shown in blue and green, respectively). The tweezers can open because of hybridization with the overhang part of F (red), which enables the F strand to free F from the tweezers and create the double-stranded waste product FF. [87]

3.3 Experimental Section

3.3.1 DNA preparation

The disulfide bonds of an 18-nt (5' CA TGT TCA GCG TAA TTTT/$(CH_2)_3$SH 3') modified oligonucleotide (from IDT DNA) were cleaved by mixing 100 mM of oligonucleotides with 100 mM tris(2-carboxyethyl) phosphine (TCEP) in a 1:600 ratio and leaving them at room temperature overnight. The TCEP-reduced 18-nt DNA was purified twice with a 3 kDa Amicon Ultra-0. 5 centrifugal filter (Millipore Sigma, Burlington, MA, USA) at 14000× g for 20 minutes, and the concentration was measured with a Thermo Scientific Nanodrop spectrophotometer. Then the solution mixture was replenished with 1 ml of 100 mM TCEP. It is known that TCEP helps retain the photoluminescence by suppressing the surface etching of the quantum dots. [90] The mixture was then diluted with Millipore water to minimize the chance of aggregation.

3.3.2 Phase transfer/ligand exchange

Octadecylamine-capped CdSe/ZnS QDs in solid form (Sigma Aldrich, Product #: 748080) were first dissolved in chloroform. The concentration was then measured using the molar extinction coefficient (e: 250000 $M^{-1}cm^{-1}$) and absorbance. Previously reduced and purified 18-nt DNA (5' CA TGT TCA GCG TAA TTTT/$(CH_2)_3$SH 3') was used for surface functionalization. To find the optimal condition for this reaction, reaction mixtures with DNA/QD molar ratios of 20:1, 80:1, 160:1, 320:1, and 640:1 were prepared under the following conditions: 100 ml of the reduced DNA-TCEP mixture, 50 ml of dimethyl sulfoxide (DMSO), and 100 ml of chloroform were added to each vial, followed by the addition of the QDs (typically 2.44 mM). Due to slow evaporation during the reaction, chloroform was replenished during the phase transfer. Then 9 ml of 25 mM $Zn(NO_3)_2$ was added to the reaction to preserve the QD photoluminescence by passivating the electron surface/hole traps.[91, 92] The mixtures were vortexed for 0.5 hours before the addition of NaOH. The stepwise addition of NaOH was done at 1-hour intervals and stopped when the pH reached 9.5–10. The final concentration of NaOH at which this pH is achieved is dependent on the DNA concentration.

3.3.3 Preparation of DNA-conjugated gold nanoparticles

A salt-aging method developed by Mirkin *et al*. [93] was used to conjugate gold nanoparticles with DNA. Thiol-modified 18-nt oligonucleotides (5'-GT AGT CGC AGA TTA TTTT/$(CH_2)_3$SH 3') were treated with 100 mM TCEP in a 1:600 ratio overnight to cleave the disulfide bond and then purified with a 3 kDa Amicon Ultra-0. 5 Centrifugal Filter (Millipore Sigma, Burlington, MA, USA) twice at 14,000× g for 20 minutes. The purified concentration was measured with a NanoDrop™ spectrophotometer. The oligonucleotides were then mixed with 10 nm AuNPs at a molar ratio of 660:1. After adjusting the final concentration of SDS to 0.01% w/v, a 5 M NaCl solution was added to the mixture to gradually increase the final concentration of NaCl in the mixture to 0.3 M for 3 hrs. The mixture was then purified using a 100 kDa Amicon Ultra-0.5 Centrifugal Filter eight times at 14000× g for five minutes.

3.3.4 DNA origami formation

The DNA origami tiles used in this study were designed with Cadnano [94] and prepared using a previously published method. [95] M13mp18 DNA (New England Biolabs) in 1× TAE-Mg^{2+} buffer (10 mM Tris base, 1 mM Ethylenediamine Tetraacetic Acid (EDTA), 14 mM $MgCl_2$) was mixed with a 100-fold excess of short staple strands and thermally annealed from 95 °C to 20 °C in a thermocycler (BIO-RAD T100) at a rate of -1°C per minute. The folded DNA nanostructures were separated from excess DNA staple strands using a 50K Da Amicon Ultra-0.5 Centrifugal Filter. The filtration was performed at 3500× g for 2 minutes and 5 times. Each time, the solution was replenished with 1× TAE, and the final concentration of $MgCl_2$ was adjusted to 10 mM.

3.3.5 Self-assembly of nanoparticles on DNA origami

To bind the DNA-conjugated gold nanoparticles and QDs to the DNA origami tile, we used a 2-step sequential annealing method. In the first step, the purified tiles were mixed with the prepared QD nanoparticles and were annealed to the tiles at a 2× equimolar concentration in 1× TAE buffer and 12.5 mM $MgCl_2$. The annealing was performed in a thermocycler (Eppendorf) at a rate of 1 °C per minute. To remove unbound nanoparticles, two rounds of purification were performed using size exclusion spin columns (gel filtration purification method in SI). In the second step, purified AuNP-DNA conjugates were annealed to the previously made QD-tiles at a 2× equimolar concentration in 1× TAE buffer and 12.5 mM $MgCl_2$. The annealing was performed in a thermocycler (BIO-RAD T100) starting at 41°C and slowly decreasing to 20 °C at a rate of -1 °C per minute. The nanoparticle-DNA origami conjugates were then purified again with size exclusion spin columns twice before TEM imaging.

3.3.6 Spectroscopic characterization

Concentrations of DNA origami, thiol-modified DNA, and unfunctionalized and functionalized AuNP were determined using a NanoDropTM ND-1000 spectrophotometer (Thermo Fisher Scientific). UV-Vis spectra of unfunctionalized QDs were collected using a Perkin-Elmer Lambda 35 UV/Vis spectrophotometer with a 100 μL quartz cuvette. Fluorescence spectroscopy measurements were done using a HORIBA Instruments Inc. (FL-1000) spectrometer equipped with a thermoelectrically cooled BIUV Synapse CCD detector. Although the slit width and the integration time were varied to optimize the signals, identical slit widths and integration times were used for the same set of spectra. The fluorescence intensity of functionalized QD was measured using a 50 μL Quartz 701MF sub-micro black fluorometer cuvette (Fireflysci), and the QD-Origami and QD-Au-Origami samples were run using a HORIBA Microsense (1-5 μL) cuvette.

3.3.7 Kinetics measurements

The fluorescence kinetics over the strand displacement time were monitored with a HORIBA Instruments Inc. FL-1000 spectrometer equipped with a thermoelectrically cooled BIUV Synapse CCD detector. All kinetic experiments were performed at 25 °C in 1 × TAE 5 mM $MgCl_2$ in a HORIBA Microsense (1–5 μL) cuvette. Before the start of the reaction, the sample's temperature was allowed to stabilize for at least 300 s. Once thermally stabilized, the invader strand was added to the origami solution to start the reaction, and the fluorescence signal was measured in 5-minute increments.

3.3.8 Agarose gel electrophoresis

For DNA-functionalized nanoparticles, 0.5% agarose gels were prepared with 0.5× TBE buffer and were run for 40 minutes with 0.5× TBE buffer at 65 volts. For origami tiles and the annealed products, 1% agarose gels were prepared with 0.5× TBE and 12mM $MgCl_2$. The gels were stained with fluorescent SYBR Green I (10,000×, Invitrogen), and a blue loading dye (6× NEB) was added to the sample solutions before gel electrophoresis. The running buffer for the tiles was 0.5× TBE with 5 mM $MgCl_2$ and the gels were run for 1 hour at 65 volts.

3.3.9 Purification of nanoparticle-DNA origami conjugates with gel filtration method

The nanoparticle-DNA origami conjugates were purified using a previously reported size-exclusion spin-column-based method [96] with slight modifications. In short, the size exclusion Sepharose CL-4B resins (Sigma-Aldrich) were buffer exchanged by repetitive resuspension or pelleting in 0.5× TAE and 4 mM $MgCl_2$ six times (200 µL of crude resin was diluted to 1000 µL with 0.5× TAE and 4 mM $MgCl_2$ and spun at 800 *g* for 3 min) and the resin was adjusted to a 50% v/v slurry. The resins were then loaded into empty spin columns (from Thermo Scientific) and spun twice to fill the tube with the resin up to 80% volume. Each time, the excess buffer in the resin was removed by spinning the columns at 15 °C at 800 *g* for 1 min. The crude nanoparticle-origami tile mixture was then subsequently passed through two spin columns (spun at 800 *g* for 3 min).

3.4 Results and Discussion

3.4.1 Heterodimer-tile Design

Previous studies on AuNP-QD heterodimers have shown a long-range (~14 nm–70 nm) fluorescence quenching of QD, possibly related to increased nonradiative decay mechanisms brought on by the presence of neighboring AuNP.[80] Therefore, in order to make a fluorescent-based DNA origami biosensor, we designed a heterodimer assembly composed of a 10 nm Au nanoparticle and a 7 nm quantum dot that are placed at predetermined locations on the origami tile. The nanoparticles were pinned on the surface by using complementary DNA ligands that could hybridize with the DNA origami capture strands at predetermined locations. For each nanoparticle, three capture strands were incorporated to guarantee the binding. The location of the capture strands was mapped to yield a 20 nm center-to-center distance after the self-assembly to ensure efficient and measurable fluorescence quenching.

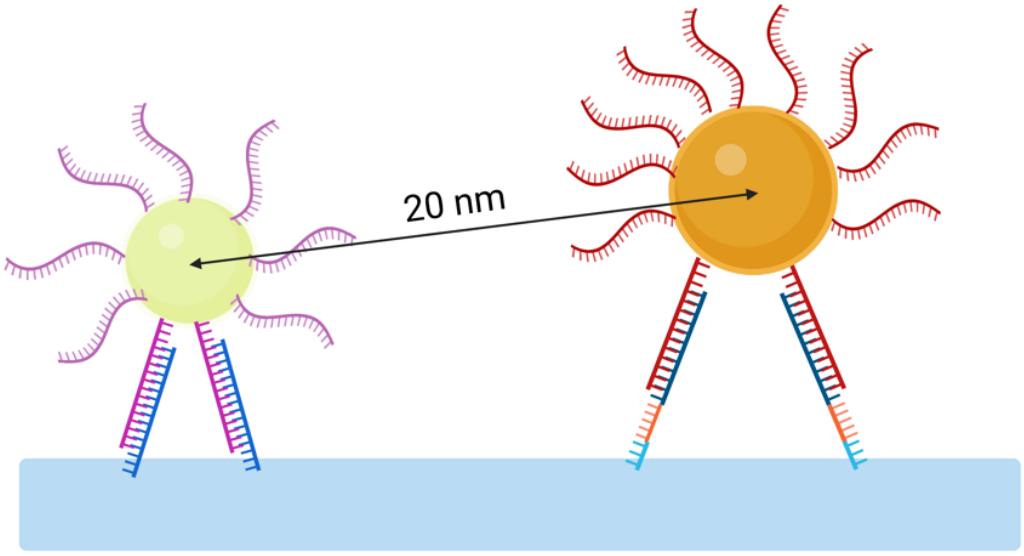

Figure 29. the heterodimer-tile design. Green and yellow nanoparticle represents the QD and AuNP respectively. For simplicity only two capture strands are depicted.

3.4.2 Toehold Design

Using a toehold in DNA origami can improve sensitivity in DNA biosensors by allowing for a more efficient and specific recognition of target molecules. [83, 85] By incorporating a toehold into the DNA origami design, the interaction between the probes and target molecules can be controlled and optimized, leading to increased sensitivity of the biosensor. For example, in a DNA biosensor for the detection of a specific target molecule, the toehold strand may be complementary to a part of the target molecule. When the target molecule binds to the toehold, it can displace a longer complementary strand, leading to an increase in fluorescence or a change in the electrophoretic mobility of the DNA biosensor. [85, 97, 98] The use of toeholds in DNA origami can also aid the creation of multiple probe-target interaction sites, which can amplify the signal generated by each interaction and enhance the overall signal transduction. This can further increase the sensitivity of the biosensor, making it capable of detecting target molecules at lower concentrations. [65, 99]

The study and implementation of nucleic acid strand-displacement processes are a focus of dynamic DNA nanotechnology. Originally studied for their possible role in recombination, strand-displacement reactions often involve a three- or four-way migration of branches. The rate of strand displacement can be tuned by more than six orders of magnitude using toeholds, single-stranded regions of DNA to which an invading strand can connect to initiate strand displacement and branch migration. [100]

The design of the toehold segments and the tactics that may be utilized to optimize the kinetics and thermodynamics of the strand displacement have been the subject of in-depth studies. These techniques include modifying the toehold segment's length, [101] adding mismatches, [102] moving the toehold segment, [97] and incorporating linear vs. double-stranded probes. In a study by Winfree *et a*l., they developed a model that showed the length of the toehold directly affects the rate of the reaction and that there is a solid connection between the kinetics and thermodynamics in toehold-mediated strand displacement reactions. [98] To accelerate the strand displacement reaction, the invading toehold must be made stronger thermodynamically, which could be done by increasing the toehold length. Therefore, quicker strand displacement reactions in the net reaction are more thermodynamically advantageous. In their study, the length of the toehold to reach the maximum rate is estimated to be 5–10 bases. [98]

Another study by the same team examined the relationship between strand displacement kinetics and toehold length using two parameters. First, the physical mechanism by which a single step of branch migration takes place is considerably slower than the fraying of a single base pair. Second, attempting branch migration imposes a thermodynamic penalty because it creates further overhang at the junction, which is not considered by nearest neighbor models of DNA. [100] By adding a toehold strand displacement mechanism to our DNA origami design, we aimed to enhance the signal and increase the sensor's sensitivity so it could work at lower concentrations. Other research, which concurs with the previous studies, has indicated that the ideal length of the toehold is 6-7.[103, 104] It is also reported that the addition of the toehold segment at the 5' end could improve the rate of displacement. Based on these reports, I added six bases to the 5' end of the capture strands on the DNA in my toehold design and examined the strand displacement efficacy using fluorescence spectroscopy. [101] To achieve this, the DNA origami was folded using the described method for the experiment. The dimer was then formed by sequentially adding QD and Au nanoparticles to the DNA origami solution, and to incorporate a toehold strand displacement strategy, the intended toehold invader strand, which included a complementary sequence to the capture strand, was then added to the reaction mixture to assess its strand displacement capabilities.

DNA Strand	Sequence (5’ to 3’)
Extended DNA staple (capture strand)	**TAATCTGCGACTAC*TGCCAA***TTTTAGTAGCATACAT TTCGCAAATGGTAGGTCAGG
Complimentary ligand of QD NP	**GTA GTC GCA GAT TA**
Invader strand	***TTG GCA* GTA GTC GCA GAT TA**

Table 1. Toehold design of the biosensor

3.4.3 Fluorimetry Characterization

To test our heterodimer’s ability to function as a biosensor with the toehold design, we first performed displacement experiments with varying toehold ligand concentrations. In our experiment, a solution of 15 nM of the heterodimer tile was mixed with the invader strand (target, or analyte) at different final concentrations: 5 μM, 10 μM, 20 μM, 40 μM, and 80 μM. The mixtures were incubated for 3 hours before fluorescence spectroscopy was carried out. To measure the response of the QD fluorescent emission to the addition of the target. To quantify the response, the percentage increase in fluorescence at 560 nm was calculated for different invader strand concentrations. Fluorescence Increase (%) was determine by using the following equation, where F_o is fluorescence intensity of the heterodimer-tile and F is fluorescence intensity after the addition of invader strands.

$$F_I = \frac{F\text{-}F_o}{F_o} \times 100$$

As expected, when 5 uM of invader strands are added to displace AuNPs from the tile, the fluorescent signal of the QDs is increased by 38% (Figure 8). Since the AuNP can quench the PL of QDs nearby, when they are removed from the origami breadboard, this quenching effect is impeded, and as a result, the fluorescence signal is increased. With the addition of the invader at higher concentrations, more AuNPs are displaced, and therefore this fluorescent signal is recovered. Our experiment also shows that after 20 μM the QD PL starts to decrease. The decrease may be caused by nonspecific interactions between excess invader strands and quantum dots, which may change the emission. This experiment was also performed with unmodified origami tiles that lacked the toehold design (Appendix). A similar trend was also observed, as the invader ligand could still displace the AuNPs without the toehold modifications; however, the overall increase for the toehold design is 34%, while for the unmodified tile, this increase is around 26%.

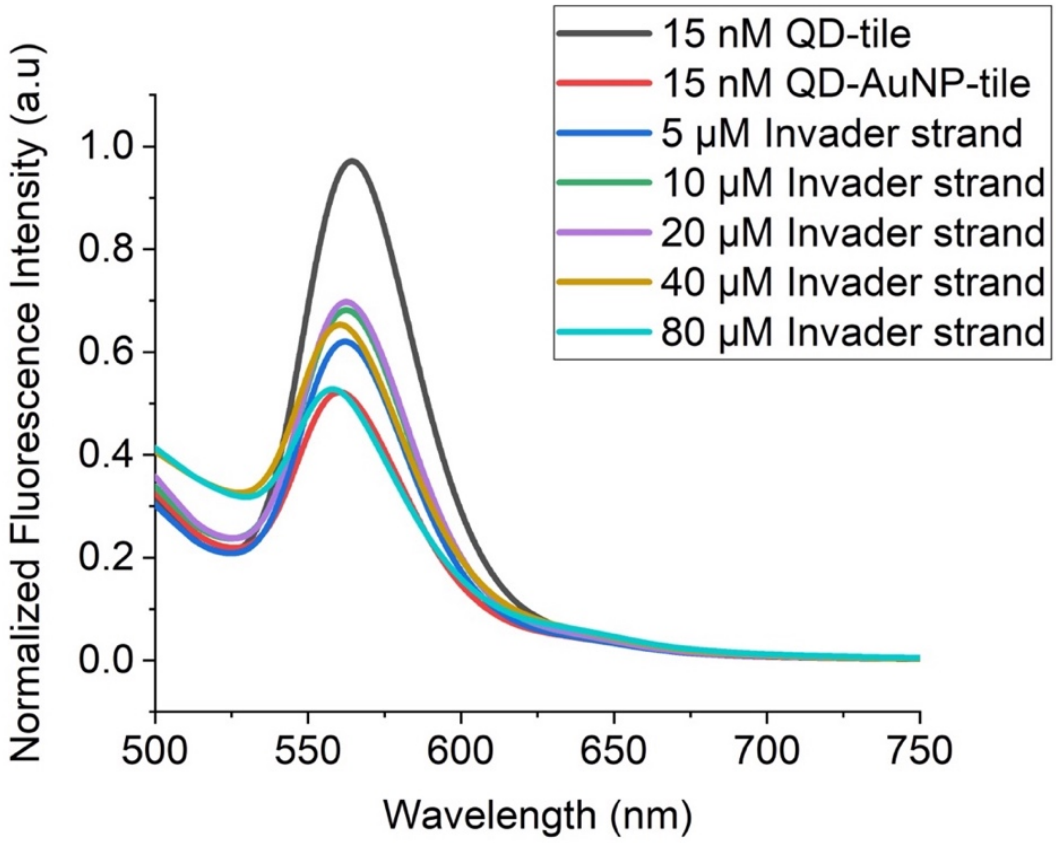

Figure 30. AuNP displacement with the addition of an invader DNA strand. The reaction mixture was incubated for 3 hours before fluorescence measurements. Fluorescence response was obtained by excitation at 470 nm, slit width of 13 nm, and integration time of 1.2 s.

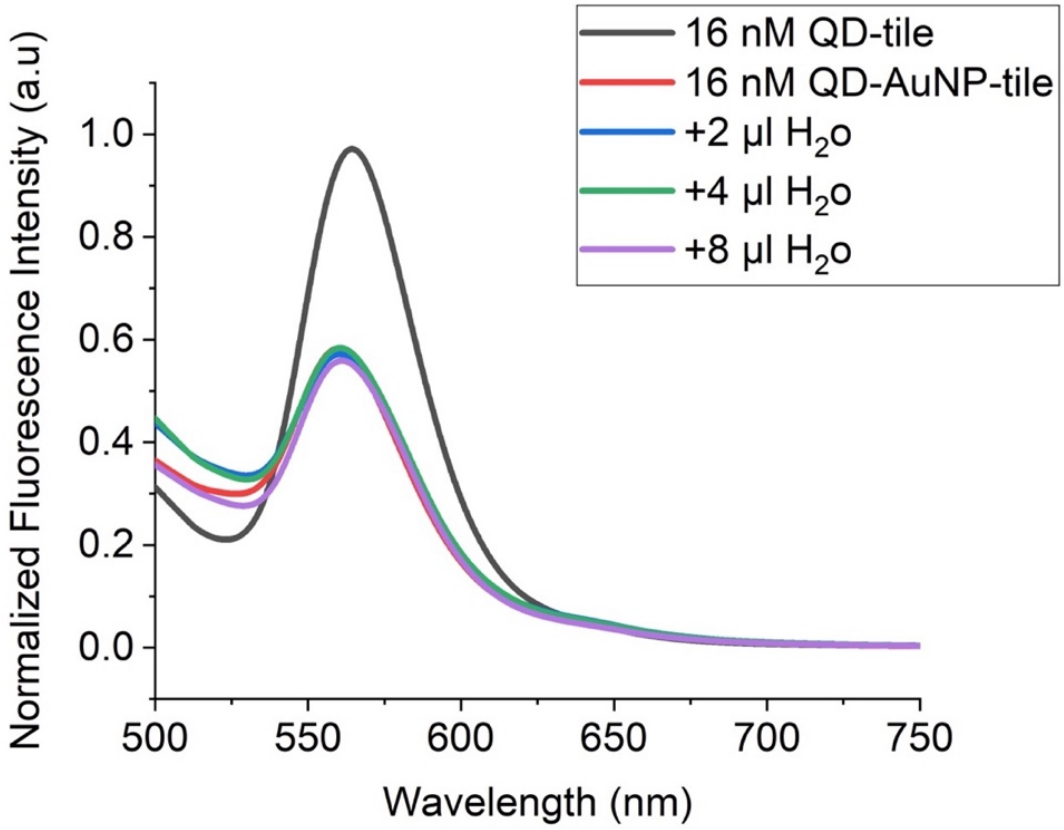

Figure 31. *control experiment: addition of water does not affect the PL signal. The reaction mixture was incubated for 3 hours before fluorescence measurements.*

As an additional control to account for the effect of the small volume change when the invader strands were added, a solution mixture of QD-AuNP-tile was prepared and mixed with three different portions of water (Figure 9). As it's shown, the addition of water didn't affect the PL signal, confirming that the displacement only occurs when the designed invader strand is added.

A key feature of the biosensor is its ability to detect analytes even at very low concentrations. Therefore, in another attempt, we measured the PL response of the heterodimer at lower concentrations of invader strands. For this experiment, the final concentration of the invader was lowered to 4.3 µM, 2 µM, and 430 nM. After the addition of the invader, the reaction mixture was incubated for 3 hours at room temperature to reach equilibrium.

The fluorescence spectra (Figure 10) show a similar trend. As the concentration of the invader strand is increased, the fluorescence increase becomes more pronounced. Even though in the current study we did not measure the limit of detection, a significant increase in fluorescence, as high as 31%, was observed at concentrations as low as 430 nM. Although the data is not sufficient for us to determine the limit of detection for our sensor, we expect it to be in the range of low tens of nanomolar as the fluorimeter is capable of reliably detecting signal changes as small as a few percent. In parallel, this experiment was

also done with the unmodified DNA origami, in which the toehold fragment was not incorporated into the capture strands (Figure S4), and even though the trend is similar to the toehold-mediated DNA displacement, in lower final concentrations (430 nM) the unmodified DNA origami fluorescence increase is only 6%, which is substantially lower than that observed with the toehold-modified origami design.

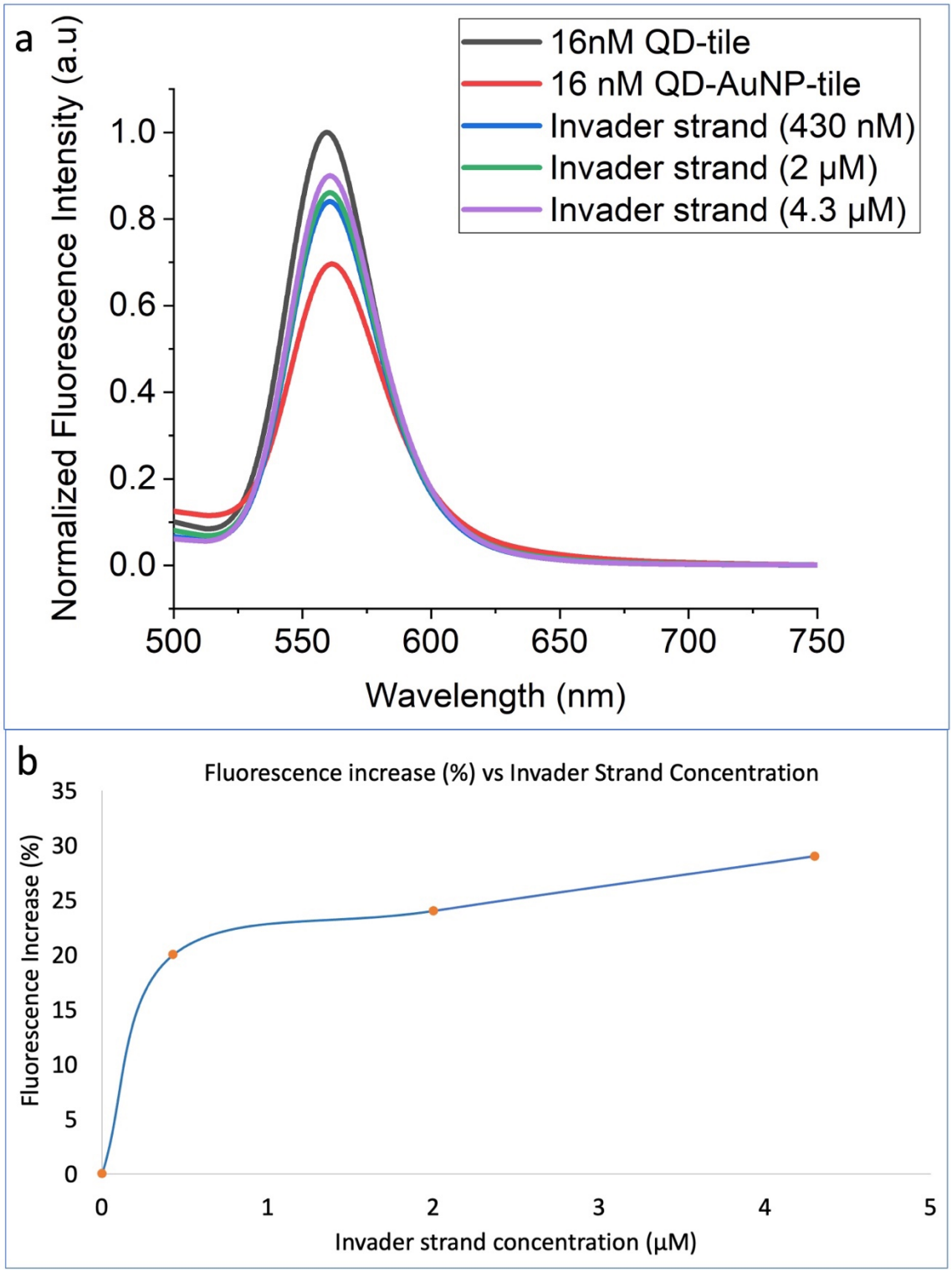

Figure 32. a) AuNP displacement with the addition of invader DNA strand at low concentrations (4. 3 µM, 2 µM, 430n M). The reaction mixture was incubated for 3 hours before fluorescence measurements) b) Fluorescence increase (%) was measured for different invader strand concentration.

3.4.4 Kinetics measurement

In the context of toeholds, kinetics measurements are important because they help determine the efficiency of the toehold-mediated strand displacement reaction. This reaction is used to detect the presence of target analytes in several biosensors. [65, 98] Knowledge of strand-displacement kinetics can be used to optimize the design of the biosensor and ensure that it operates at maximum efficiency.

The parameter settings for the fluorescence measurements were as follows: 470 nm, a slit width of 12 nm, and an integration time of 1.5 s. A 1 nm excitation slit was chosen to reduce the photobleaching of the dye molecules, while a 12 nm emission slit ensured the collection of a larger number of emitted photons. The fluorescence spectra of the strand displacement over the course of 25 minutes are shown in Figure 11. Based on these results, the fluorescence signal is increasing over time, which is the consequence of strand displacement as seen in our previous experiment. As the invader strand hybridizes with the capture strand, the AuNP quenchers are displaced from the surface, and therefore, the QD PL is enhanced. The fluorescence increase is gradually increased with time as more AuNPs get displaced. The preliminary results reveal that the signal starts to level off after 25 minutes, which suggests that the strand displacement is near completion after this point (Figure 11b). However, follow-up experiments with longer reaction times need to be performed.

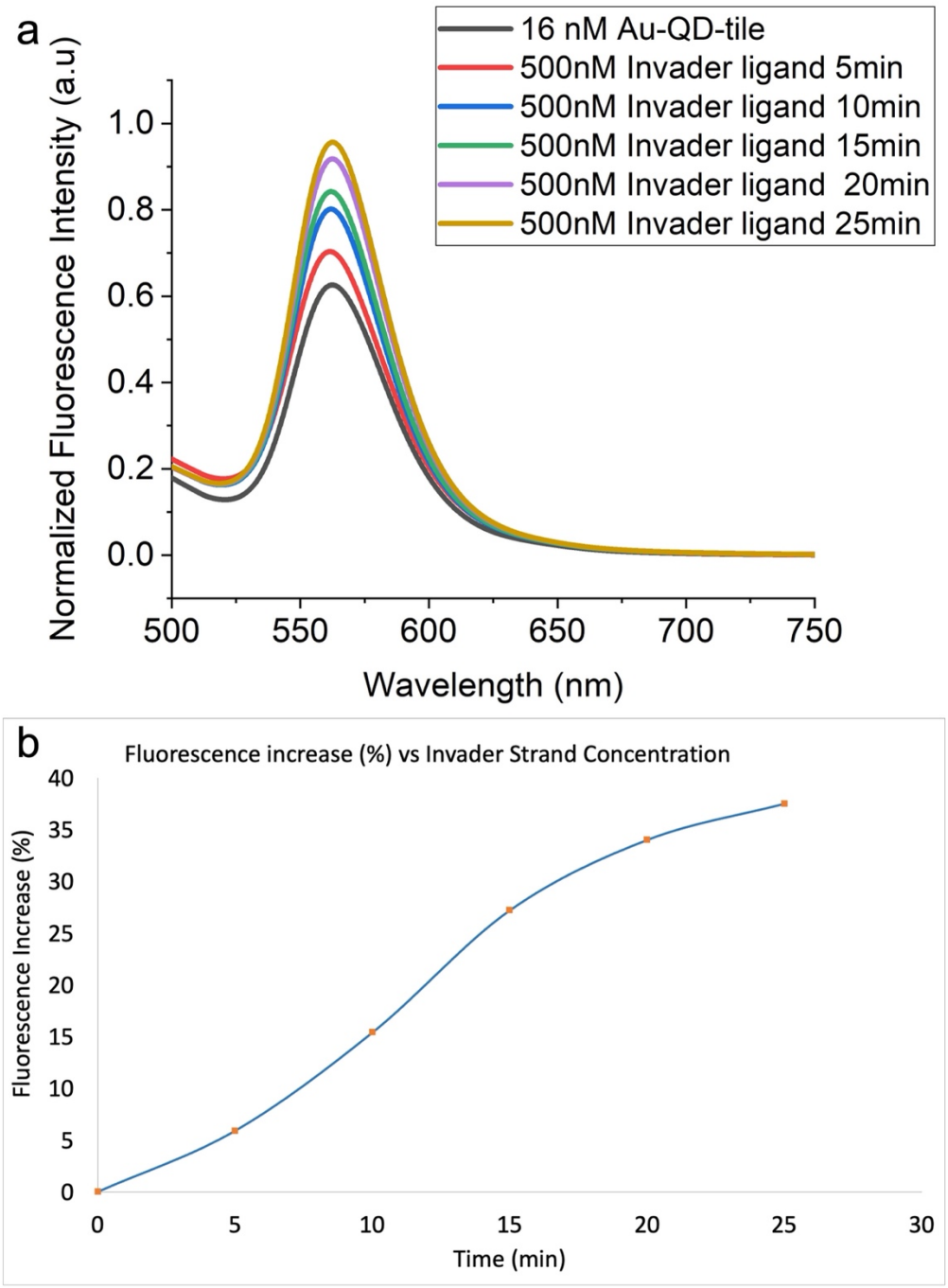

Figure 33. a) The fluorescence response of QDs after the addition of the strand was measured at excitation wavelength: 470 nm, slit width of 8 nm, and integration time of 5s. b) Fluorescence increase (%) was measured over 25 minutes.

We used the Box-Lucas model, a mathematical representation of the kinetics of a reaction, to analyze the kinetics of this model biosensor. This model is commonly used in biochemistry and biophysics to model the kinetics of enzyme-catalyzed reactions and other biochemical processes. The Box-Lucas model can be used to explain the kinetics of a pseudo-first-order reaction in the context of DNA strand displacement, where the rate of the reaction is completely determined by the concentration of one reactant. In this case, the reaction is typically modeled as a competition between the incoming strand (the displacer) and the outgoing strand (the target). In a pseudo-first-order reaction, the order of the reaction with respect to the reactant that is present in excess (and remains constant) is effectively zero, while the order of the reaction with respect to the other reactant(s) is effectively first-order. Hence, in this case, the order of the reaction with respect to the target strand is pseudo-first-order or effectively first-order. To use the Box-Lucas model for pseudo-first-order kinetics of a DNA strand displacement, we first defined the rate equation for the reaction. This equation would typically include the concentration of the incoming strand, the concentration of the outgoing strand, and the rate constant for the reaction.

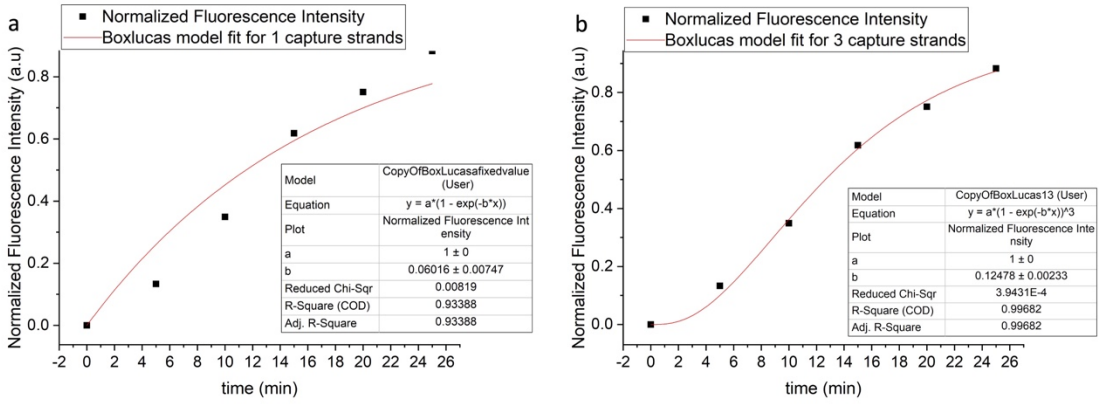

Figure 34.Box-lucas model fit for the case 1 target strand (a) vs 3 target strands (b).

The Box-Lucas model can provide valuable insights into the underlying mechanisms of the reaction, with the rate constant for the reverse reaction being higher with multiple target strands compared to one target strand, leading to a faster overall reaction rate. The concentration of the target strands should be considered when analyzing the kinetics of the reaction using the Box-Lucas model to accurately estimate the rate constant and other parameters of the reaction. In terms of the kinetics of the reaction, it follows a pseudo-first-order mechanism, with the integrated form of the rate equation for a pseudo-first-order reaction being:

$$\frac{[A]_t}{[A]_0} = e^{-kt} \qquad (6)$$

where $[A]_t$ is the concentration of the reactant at time t, $[A]_0$ is the initial concentration of the reactant, and k is the rate constant. Comparing the two equations, we can see that Y corresponds to $\frac{[A]_t}{[A]_0}$, and the term $(1 - e^{(-bx)})$ corresponds to e^{-kt}. Comparing

the two equations, we can see that Y corresponds to $\frac{[A]_t}{[A]_0}$, and the term ($1 - e^{(-bx)}$) corresponds to e^{-kt}. Therefore, the equation given represents a pseudo-first-order reaction with a rate constant of $k' = 0.060\ s^{-1}$, for one capture strand and $k' = 0.125\ s^{-1}$ for three capture strands. R-squared (R^2) can be used in this nonlinear regression to identify which of these models provides a better fit to the data. The model anticipates that the displacement of one capture strand will result in the dissociation of AuNP and the activation of the fluorescence signal. However, this is not the case, and the fact that $R^2 = 0.934$ further demonstrates that it cannot be the correct fit. In our designed biosensor in order to dissociate the AuNP, the strand displacement of three capture strands is required. To better find a model to include the number of capture strands we used binomial distribution. The Binomial distribution can be applied in the context of strand displacement kinetics to model the probability of a certain number of displacement events occurring within a population of DNA molecules. In a strand displacement reaction, a population of DNA molecules is exposed to a set of input signals that trigger the displacement of the target molecule. The number of displacement events that occur within the population can be modeled using a binomial distribution, which describes the probability of a certain number of successes (displacement events) in a fixed number of trials (DNA molecules). The binomial distribution is characterized by two parameters: the number of trials (n) and the probability of success (p) in each trial. In the context of strand displacement, the number of trials corresponds to the number of DNA molecules in the population, and the probability of success corresponds to the probability that a given molecule will undergo displacement in response to the input signals. After applying the binomial distribution to this kinetic model for three capture strands, the R^2 increased to 0.997 confirming that it better fits our experimental data. As was said earlier, in order to determine the rate constant of the second order reaction, we need to take into account the concentration of the target and convert the fluorescent signal to the molar concentration of the reactant. Following these steps, the rate constant of the reaction changes to $3.75 \times 10^6\ M^{-1}\ sec^{-1}$ and $7.81 \times 10^6\ M^{-1}\ sec^{-1}$, respectively, for one capture strand against three capture strands models. These values are commensurate with previous values found in the literature for toehold-mediated strand displacement.[105]

Understanding the kinetics of DNA strand displacement reactions is important because it can inform the design of efficient and specific DNA-based systems for various applications in biotechnology and medicine. These applications include biosensors, drug delivery systems, gene therapy, and DNA computing, among others. In biosensors, for example, the kinetics of DNA strand displacement reactions can be used to design sensors that can detect specific molecules or ions in a sample. By controlling the concentration of target strands, the sensitivity and specificity of the sensor can be optimized, resulting in a more accurate and reliable detection system. Overall, knowledge of the kinetics of DNA strand displacement processes and their dependency on target strand concentration can be useful for creating effective and targeted DNA-based systems for diverse biotechnology and medical applications.

3.5 Conclusion and Outlook

The purpose of this chapter was to show how our heterodimer design can function as a biosensor. This experiment proved that with a proper toehold mediated strand displacement strategy and a well-thought-out invader strand design the sensor could perform at concentrations as low as 430 nM and detect show a 38% fluorescence increase in QD PL signal. Given that fluorescence spectroscopy is capable of detecting much smaller signal changes, we expect that the actual limit of detection to be in the range of nM to tens of nM. The kinetics measurement further demonstrates that the displacement approaches completion in about 25 minutes which is a relatively fast response for a FRET based DNA biosensor. We found that a model based on the independent strand displacement of three capture strands can quantitatively describe the observed time dependence of fluorescence. Although this result is intriguing, more replications and testing at lower target strand concentrations are required to validate the sensor for practical application. Perhaps the fluorescence signal should be observed for a longer period for the reaction to reach equilibrium and the fluorescence signal to plateau.

Although the results are preliminary, they do showcase the promise of a highly tunable design. This biosensor design serves as a model system that allows us to systematically and rationally tune molecular recognition and signal transduction to improve the performance of the sensor. There are numerous opportunities to improve the sensor's performance. For example, it allows for the evaluation of various toehold configurations and their effects on the kinetics and thermodynamics of strand displacement. By fine-tuning the toehold design, length, mismatch, and toehold location, the molecular recognition of the sensor could be enhanced, resulting in a faster response and a reduced detection limit. Moreover, we expect that larger AuNPs (30 nm or 50 nm) can be utilized to improve the sensitivity of the sensor. As they can quench signals more efficiently compared to 10 nm AuNPs, the displacement of these larger AuNPs by target molecules will lead to a significantly larger change in fluorescence signal, improving the sensitivity of the sensor. DNA origami's programmability also allows us to readily change the distance between QD and AuNPs. According to the FRET principles, the QD fluorescence will be more quenched if the particles are positioned closer together, which will lead to a more pronounced change in fluorescence as a result of binding events. Tuning the number of capture strands could also be implemented to modify the sensor's sensitivity. Reducing the number of capture stands might facilitate displacement and necessitate fewer invaders for displacement, therefore increasing the biosensor’s sensitivity. Furthermore, due to the superior photophysical properties of QDs, this sensor does not suffer from low photostability and low intensity compared to its fluorescent dye-based counterparts. We might also potentially improve the capability of our sensor to detect proteins or other biomarkers by incorporating aptamers into our design in the future. Overall, such a model facilitates research on the kinetics and thermodynamics of strand displacement using an optical sensor.

3.6 Appendix

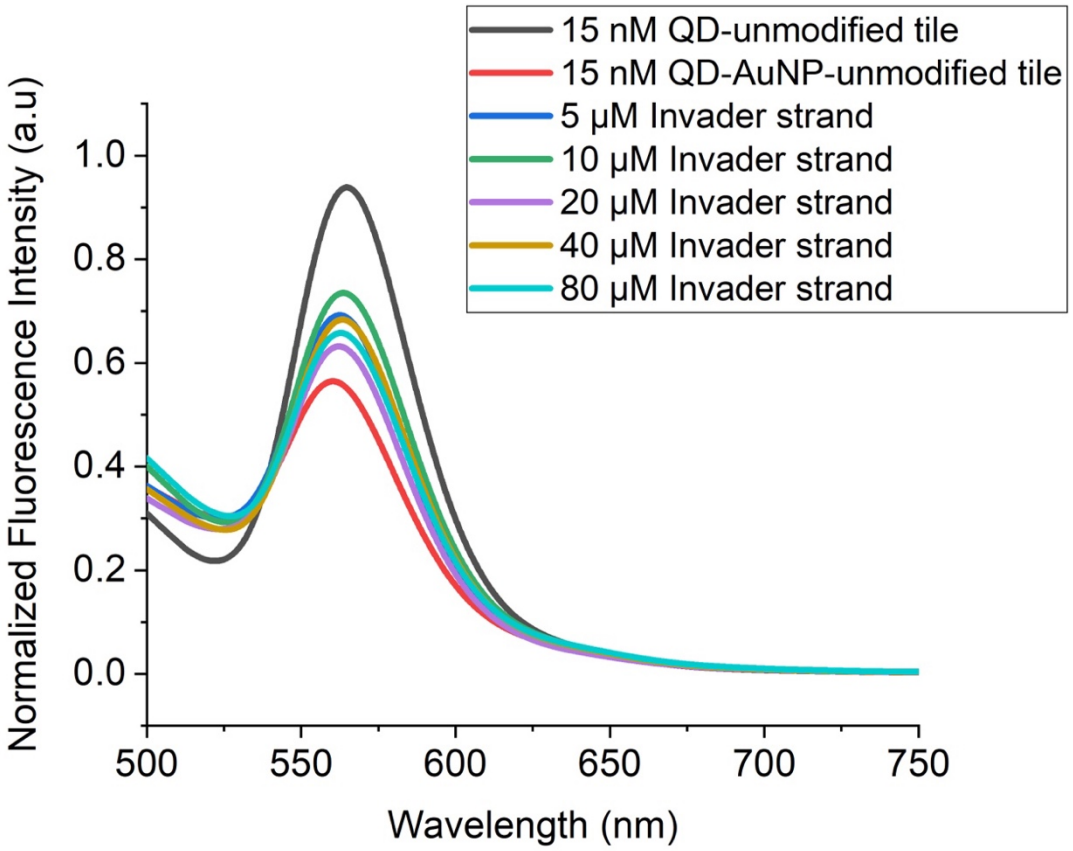

Figure S1. AuNP displacement with the addition of an invader DNA strand. The reaction mixture was incubated for 3 hours before fluorescence measurements.

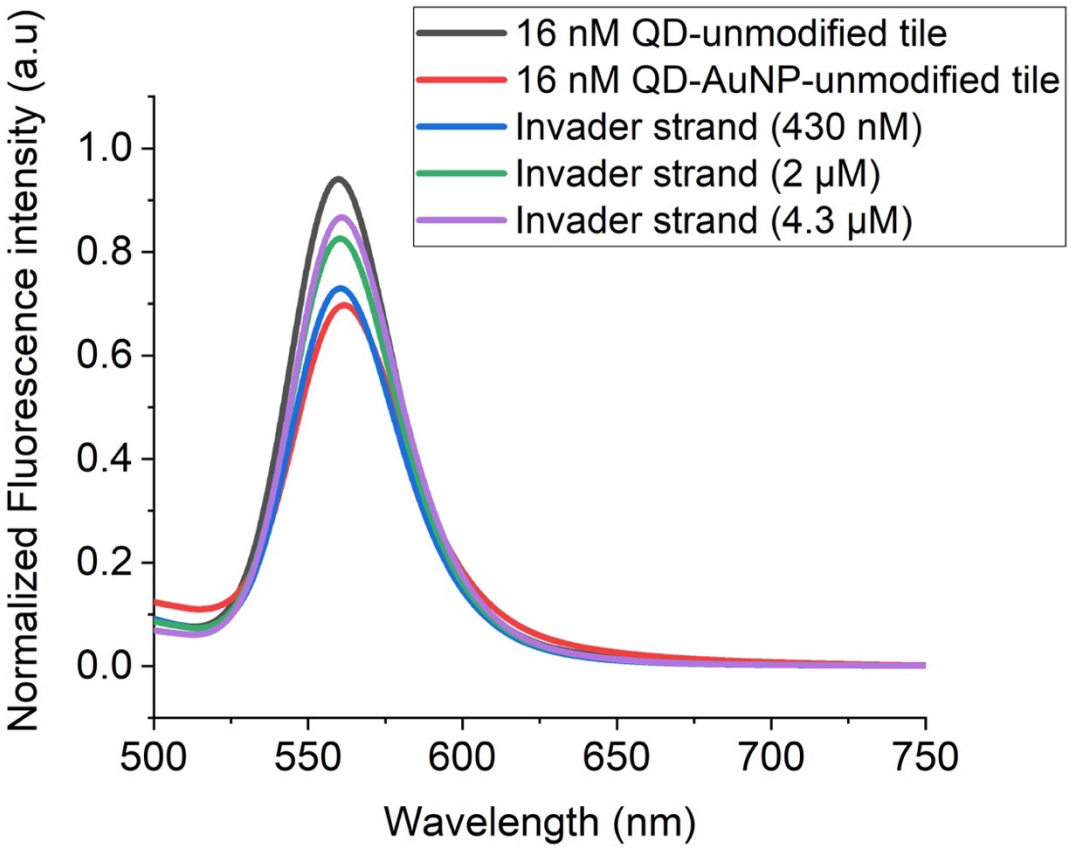

Figure S2. AuNP displacement with the addition of an invader DNA strand at lower concentrations. The reaction mixture was incubated for 3 hours before fluorescence measurements.

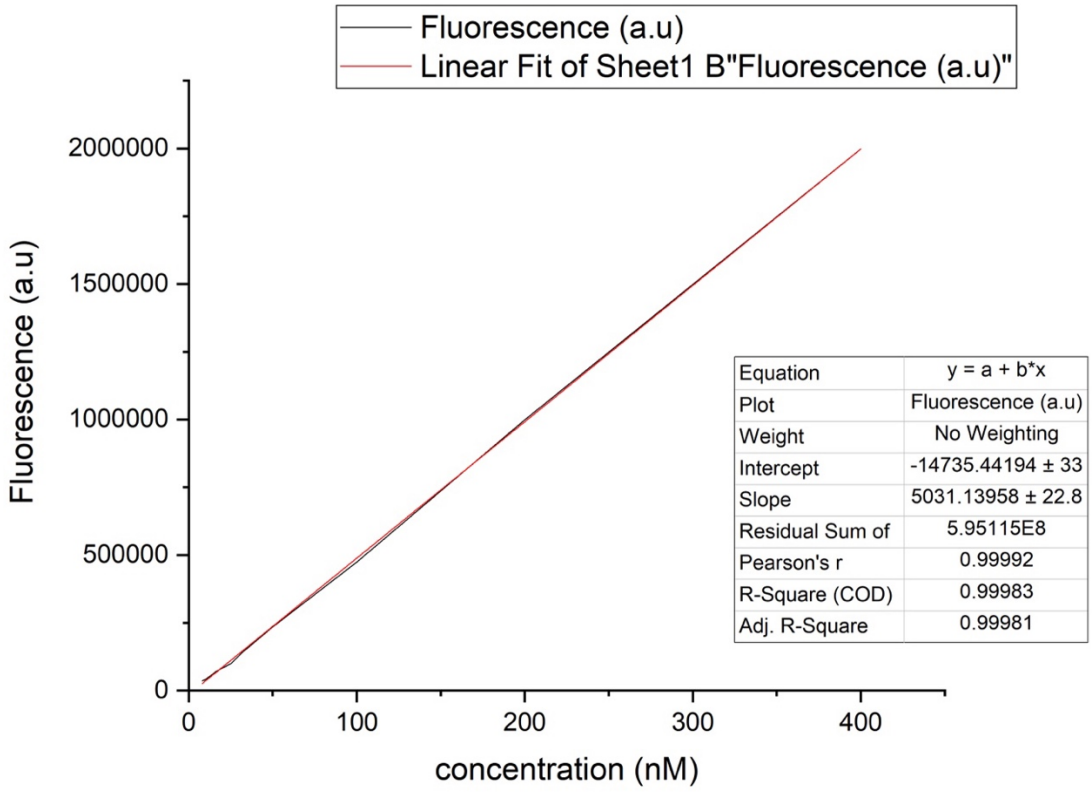

Figure S3. calibration curve to measure functionalized QD-tile nanoparticles concentration

3.7 References

(1) Fu, J.; Yang, Y. R.; Johnson-Buck, A.; Liu, M.; Liu, Y.; Walter, N. G.; Woodbury, N. W.; Yan, H. Multi-enzyme complexes on DNA scaffolds capable of substrate channelling with an artificial swinging arm. *Nature Nanotechnology* **2014**, *9* (7), 531-536

(2) Chidchob, P.; Sleiman, H. F. Recent advances in DNA nanotechnology. *Current Opinion in Chemical Biology* **2018**, *46*, 63-70

(3) Whetton, A. D.; Preston, G. W.; Abubeker, S.; Geifman, N. Proteomics and Informatics for Understanding Phases and Identifying Biomarkers in COVID-19 Disease. *Journal of Proteome Research* **2020**, *19* (11), 4219-4232

(4) Kubista, M.; Andrade, J. M.; Bengtsson, M.; Forootan, A.; Jonák, J.; Lind, K.; Sindelka, R.; Sjöback, R.; Sjögreen, B.; Strömbom, L.; et al. The real-time polymerase chain reaction. *Molecular Aspects of Medicine* **2006**, *27* (2), 95-125

(5) Tsukahara, T.; Nagasawa, H. Probe-on-carriers for oligonucleotide microarrays (DNA chips). *Science and Technology of Advanced Materials* **2004**, *5* (3), 359

(6) Lequin, R. M. Enzyme Immunoassay (EIA)/Enzyme-Linked Immunosorbent Assay (ELISA). *Clinical Chemistry* **2005**, *51* (12), 2415-2418

(7) Yazawa, K.; Furusawa, H. Probing Multiple Binding Modes of DNA Hybridization: A Comparison between Single-Molecule Observations and Ensemble Measurements. *ACS Omega* **2018**, *3* (2), 2084-2092

(8) Peterson, E. M.; Reece, E. J.; Li, W.; Harris, J. M. Super-Resolution Imaging of Competitive Unlabeled DNA Hybridization Reveals the Influence of Fluorescent Labels on Duplex Formation and Dissociation Kinetics. *J. Phys. Chem. B* **2019**, *123* (50), 10746-10756

(9) Kim, Y.; Lee, H. Balanced Detection Method Using Optical Affinity Sensors for Quick Measurement of Biomolecule Concentrations. *Analytical Chemistry* **2020**, *92* (9), 6189-6193

(10) Lynn, N. S.; Šípová, H.; Adam, P.; Homola, J. Enhancement of affinity-based biosensors: effect of sensing chamber geometry on sensitivity. *Lab on a Chip* **2013**, *13* (7), 1413-1421

(11) Sevenler, D.; Trueb, J.; Ünlü, M. S. Beating the reaction limits of biosensor sensitivity with dynamic tracking of single binding events. *Proceedings of the National Academy of Sciences* **2019**, *116* (10), 4129-4134

(12) Wijaya, A.; Hamad-Schifferli, K. Ligand Customization and DNA Functionalization of Gold Nanorods via Round-Trip Phase Transfer Ligand Exchange. *Langmuir* **2008**, *24* (18), 9966-9969

(13) Saccà, B.; Niemeyer, C. M. Functionalization of DNA nanostructures with proteins. *Chemical Society Reviews* **2011**, *40* (12), 5910-5921

(14) Li, F.; Zhang, H.; Dever, B.; Li, X.-F.; Le, X. C. Thermal Stability of DNA Functionalized Gold Nanoparticles. *Bioconjugate Chem.* **2013**, *24* (11), 1790-1797

(15) Xia, T.; Yuan, J.; Fang, X. Conformational Dynamics of an ATP-Binding DNA Aptamer: A Single-Molecule Study. *J. Phys. Chem. B* **2013**, *117* (48), 14994-15003

(16) Xue, C.; Zhang, S.; Yu, X.; Hu, S.; Lu, Y.; Wu, Z.-S. Periodically Ordered, Nuclease-Resistant DNA Nanowires Decorated with Cell-Specific Aptamers as Selective Theranostic Agents. *Angewandte Chemie International Edition* **2020**, *59* (40), 17540-17547

(17) Keum, J.-W.; Bermudez, H. Enhanced resistance of DNAnanostructures to enzymatic digestion. *Chemical Communications* **2009**, (45), 7036-7038

(18) Bhalla, N.; Jolly, P.; Formisano, N.; Estrela, P. Introduction to biosensors. *Essays Biochem* **2016**, *60* (1), 1-8

(19) Song, S.; Wang, L.; Li, J.; Fan, C.; Zhao, J. Aptamer-based biosensors. *TrAC Trends in Analytical Chemistry* **2008**, *27* (2), 108-117

(20) Gong, L.; Zhao, Z.; Lv, Y.-F.; Huan, S.-Y.; Fu, T.; Zhang, X.-B.; Shen, G.-L.; Yu, R.-Q. DNAzyme-based biosensors and nanodevices. *Chemical Communications* **2015**, *51* (6), 979-995

(21) Xie, N.; Liu, S.; Yang, X.; He, X.; Huang, J.; Wang, K. DNA tetrahedron nanostructures for biological applications: biosensors and drug delivery. *Analyst* **2017**, *142* (18), 3322-3332

(22) Loretan, M.; Domljanovic, I.; Lakatos, M.; Rüegg, C.; Acuna, G. P. DNA Origami as Emerging Technology for the Engineering of Fluorescent and Plasmonic-Based Biosensors. In *Materials*, 2020; Vol. 13.

(23) Saidur, M. R.; Aziz, A. R. A.; Basirun, W. J. Recent advances in DNA-based electrochemical biosensors for heavy metal ion detection: A review. *Biosensors and Bioelectronics* **2017**, *90*, 125-139

(24) Liang, G.; Man, Y.; Li, A.; Jin, X.; Liu, X.; Pan, L. DNAzyme-based biosensor for detection of lead ion: A review. *Microchemical Journal* **2017**, *131*, 145-153

(25) Mehlhorn, A.; Rahimi, P.; Joseph, Y. Aptamer-Based Biosensors for Antibiotic Detection: A Review. In *Biosensors*, 2018; Vol. 8.

(26) Dehghani, S.; Nosrati, R.; Yousefi, M.; Nezami, A.; Soltani, F.; Taghdisi, S. M.; Abnous, K.; Alibolandi, M.; Ramezani, M. Aptamer-based biosensors and nanosensors for the detection of vascular endothelial growth factor (VEGF): A review. *Biosensors and Bioelectronics* **2018**, *110*, 23-37

(27) Abolhasan, R.; Mehdizadeh, A.; Rashidi, M. R.; Aghebati-Maleki, L.; Yousefi, M. Application of hairpin DNA-based biosensors with various signal amplification strategies in clinical diagnosis. *Biosensors and Bioelectronics* **2019**, *129*, 164-174

(28) Huo, W.; Li, X.; Wang, B.; Zhang, H.; Zhang, J.; Yang, X.; Jin, Y. Recent advances of DNAzyme-based nanotherapeutic platform in cancer gene therapy. *Biophysics Reports* **2020**, *6* (6), 256-265

(29) Ng, P.-S.; Bergstrom, D. E. Alternative Nucleic Acid Analogues for Programmable Assembly: Hybridization of LNA to PNA. *Nano Letters* **2005**, *5* (1), 107-111

(30) Martinez, K.; Estevez, M. C.; Wu, Y.; Phillips, J. A.; Medley, C. D.; Tan, W. Locked Nucleic Acid Based Beacons for Surface Interaction Studies and Biosensor Development. *Analytical Chemistry* **2009**, *81* (9), 3448-3454

(31) Kaur, H.; Babu Br Fau - Maiti, S.; Maiti, S. Perspectives on chemistry and therapeutic applications of Locked Nucleic Acid (LNA). (0009-2665 (Print)),

(32) Kim, Y.; Sohn, D.; Tan, W. Molecular beacons in biomedical detection and clinical diagnosis. *Int J Clin Exp Pathol* **2008**, *1* (2), 105-116

(33) Yang, C. J.; Wang L Fau - Wu, Y.; Wu Y Fau - Kim, Y.; Kim Y Fau - Medley, C. D.; Medley Cd Fau - Lin, H.; Lin H Fau - Tan, W.; Tan, W. Synthesis and investigation of deoxyribonucleic acid/locked nucleic acid chimeric molecular beacons. (1362-4962 (Electronic)),

(34) Fang, S.; Lee, H. J.; Wark, A. W.; Corn, R. M. Attomole Microarray Detection of MicroRNAs by Nanoparticle-Amplified SPR Imaging Measurements of Surface Polyadenylation Reactions. *Journal of the American Chemical Society* **2006**, *128* (43), 14044-14046

(35) Castoldi, M.; Schmidt, S.; Benes, V.; Noerholm, M.; Kulozik, A. E.; Hentze, M. W.; Muckenthaler, M. U. A sensitive array for microRNA expression profiling (miChip) based on locked nucleic acids (LNA). *RNA* **2006**, *12* (5), 913-920

(36) Kidambi, S.; Chan, C.; Lee, I. Selective Depositions on Polyelectrolyte Multilayers: Self-Assembled Monolayers of m-dPEG Acid as Molecular Template. *Journal of the American Chemical Society* **2004**, *126* (14), 4697-4703

(37) Yin, P.; Choi Hm Fau - Calvert, C. R.; Calvert Cr Fau - Pierce, N. A.; Pierce, N. A. Programming biomolecular self-assembly pathways. (1476-4687 (Electronic)),

(38) Tsourkas, A.; Behlke Ma Fau - Rose, S. D.; Rose Sd Fau - Bao, G.; Bao, G. Hybridization kinetics and thermodynamics of molecular beacons. (1362-4962 (Electronic)),

(39) Riccelli, P. V.; Merante, F.; Leung, K. T.; Bortolin, S.; Zastawny, R. L.; Janeczko, R.; Benight, A. S. Hybridization of single-stranded DNA targets to immobilized complementary DNA probes: comparison of hairpin versus linear capture probes. *Nucleic acids research* **2001**, *29* (4), 996-1004

(40) Xiong, E.; Li, Z.; Zhang, X.; Zhou, J.; Yan, X.; Liu, Y.; Chen, J. Triple-Helix Molecular Switch Electrochemical Ratiometric Biosensor for Ultrasensitive Detection of Nucleic Acids. *Analytical Chemistry* **2017**, *89* (17), 8830-8835

(41) Rowe, A. A.; Chuh, K. N.; Lubin, A. A.; Miller, E. A.; Cook, B.; Hollis, D.; Plaxco, K. W. Electrochemical Biosensors Employing an Internal Electrode Attachment Site and

Achieving Reversible, High Gain Detection of Specific Nucleic Acid Sequences. *Analytical Chemistry* **2011**, *83* (24), 9462-9466

(42) Wang, J. DNA biosensors based on Peptide Nucleic Acid (PNA) recognition layers. A review1This paper was a finalist for the Biosensors & Bioelectronics Award for the most original contribution to the Congress.1. *Biosensors and Bioelectronics* **1998**, *13* (7), 757-762

(43) D'Agata, R.; Giuffrida, M. C.; Spoto, G. Peptide Nucleic Acid-Based Biosensors for Cancer Diagnosis. *Molecules* **2017**, *22* (11), 1951

(44) Gan, Z.; Roslan, M. A.-O.; Abd Shukor, M. A.-O.; Halim, M. A.-O.; Yasid, N. A.-O.; Abdullah, J. A.-O.; Md Yasin, I. A.-O.; Wasoh, H. Advances in Aptamer-Based Biosensors and Cell-Internalizing SELEX Technology for Diagnostic and Therapeutic Application. LID - 10.3390/bios12110922 [doi] LID - 922. (2079-6374 (Electronic)),

(45) Townshend, B.; Xiang, J. S.; Manzanarez, G.; Hayden, E. J.; Smolke, C. D. A multiplexed, automated evolution pipeline enables scalable discovery and characterization of biosensors. *Nature Communications* **2021**, *12* (1), 1437

(46) Mou, Q.; Xue, X.; Ma, Y.; Banik, M.; Garcia, V.; Guo, W.; Wang, J.; Song, T.; Chen, L.-Q.; Lu, Y. Efficient delivery of a DNA aptamer-based biosensor into plant cells for glucose sensing through thiol-mediated uptake. *Science Advances 8* (26), eabo0902

(47) Liu, L.; Han, Z.; An, F.; Gong, X.; Zhao, C.; Zheng, W.; Mei, L.; Zhou, Q. Aptamer-based biosensors for the diagnosis of sepsis. *Journal of Nanobiotechnology* **2021**, *19* (1), 216

(48) Wang, R. E.; Zhang, Y.; Cai, J.; Cai, W.; Gao, T. Aptamer-based fluorescent biosensors. *Curr Med Chem* **2011**, *18* (27), 4175-4184

(49) Liu, J.; Lu, Y. Improving Fluorescent DNAzyme Biosensors by Combining Inter- and Intramolecular Quenchers. *Analytical Chemistry* **2003**, *75* (23), 6666-6672

(50) Ming, T.; Chen, H.; Jiang, R.; Li, Q.; Wang, J. Plasmon-Controlled Fluorescence: Beyond the Intensity Enhancement. *The Journal of Physical Chemistry Letters* **2012**, *3* (2), 191-202

(51) Ding, S.-Y.; Yi, J.; Li, J.-F.; Ren, B.; Wu, D.-Y.; Panneerselvam, R.; Tian, Z.-Q. Nanostructure-based plasmon-enhanced Raman spectroscopy for surface analysis of materials. *Nature Reviews Materials* **2016**, *1* (6), 16021

(52) Jiang, R.; Li, B.; Fang, C.; Wang, J. Metal/Semiconductor Hybrid Nanostructures for Plasmon-Enhanced Applications. *Advanced Materials* **2014**, *26* (31), 5274-5309

(53) Fan, S.; Cheng, J.; Liu, Y.; Wang, D.; Luo, T.; Dai, B.; Zhang, C.; Cui, D.; Ke, Y.; Song, J. Proximity-Induced Pattern Operations in Reconfigurable DNA Origami Domino Array. *Journal of the American Chemical Society* **2020**, *142* (34), 14566-14573

(54) Liu, Y.; Kumar, S.; Taylor, R. E. Mix-and-match nanobiosensor design: Logical and spatial programming of biosensors using self-assembled DNA nanostructures. *WIREs Nanomedicine and Nanobiotechnology* **2018**, *10* (6), e1518

(55) Wang, S.; Zhou, Z.; Ma, N.; Yang, S.; Li, K.; Teng, C.; Ke, Y.; Tian, Y. DNA Origami-Enabled Biosensors. LID - 10.3390/s20236899 [doi] LID - 6899. (1424-8220 (Electronic)),

(56) Li, J.; Dai, J.; Jiang, S.; Xie, M.; Zhai, T.; Guo, L.; Cao, S.; Xing, S.; Qu, Z.; Zhao, Y.; et al. Encoding quantized fluorescence states with fractal DNA frameworks. *Nature Communications* **2020**, *11* (1), 2185

(57) Zhou, Z.; Sohn, Y. S.; Nechushtai, R.; Willner, I. DNA Tetrahedra Modules as Versatile Optical Sensing Platforms for Multiplexed Analysis of miRNAs, Endonucleases, and Aptamer–Ligand Complexes. *ACS Nano* **2020**, *14* (7), 9021-9031

(58) Song, P.; Shen, J.; Ye, D.; Dong, B.; Wang, F.; Pei, H.; Wang, J.; Shi, J.; Wang, L.; Xue, W.; et al. Programming bulk enzyme heterojunctions for biosensor development with tetrahedral DNA framework. *Nature Communications* **2020**, *11* (1), 838

(59) Fan, Z.; Lin, Z.; Wang, Z.; Wang, J.; Xie, M.; Zhao, J.; Zhang, K.; Huang, W. Dual-Wavelength Electrochemiluminescence Ratiometric Biosensor for NF-κB p50 Detection with Dimethylthiodiaminoterephthalate Fluorophore and Self-Assembled DNA Tetrahedron Nanostructures Probe. *ACS Applied Materials & Interfaces* **2020**, *12* (10), 11409-11418

(60) Nie, W.; Wang, Q.; Zou, L.; Zheng, Y.; Liu, X.; Yang, X.; Wang, K. Low-Fouling Surface Plasmon Resonance Sensor for Highly Sensitive Detection of MicroRNA in a Complex Matrix Based on the DNA Tetrahedron. *Analytical Chemistry* **2018**, *90* (21), 12584-12591

(61) Wang, S.; Dong, Y.; Liang, X. Development of a SPR aptasensor containing oriented aptamer for direct capture and detection of tetracycline in multiple honey samples. *Biosensors and Bioelectronics* **2018**, *109*, 1-7

(62) Li, F.; Li, Q.; Zuo, X.; Fan, C. DNA framework-engineered electrochemical biosensors. *Science China Life Sciences* **2020**, *63* (8), 1130-1141

(63) Su, J.; Wu, F.; Xia, H.; Wu, Y.; Liu, S. Accurate cancer cell identification and microRNA silencing induced therapy using tailored DNA tetrahedron nanostructures. *Chemical Science* **2020**, *11* (1), 80-86

(64) Han, X.; Jiang, Y.; Li, S.; Zhang, Y.; Ma, X.; Wu, Z.; Wu, Z.; Qi, X. Multivalent aptamer-modified tetrahedral DNA nanocage demonstrates high selectivity and safety for anti-tumor therapy. *Nanoscale* **2019**, *11* (1), 339-347

(65) Zhang, Z.; Zeng D Fau - Ma, H.; Ma H Fau - Feng, G.; Feng G Fau - Hu, J.; Hu J Fau - He, L.; He L Fau - Li, C.; Li C Fau - Fan, C.; Fan, C. A DNA-Origami chip platform for label-free SNP genotyping using toehold-mediated strand displacement. (1613-6829 (Electronic)),

(66) Bhuckory, S.; Kays, J. C.; Dennis, A. M. In Vivo Biosensing Using Resonance Energy Transfer. In *Biosensors*, 2019; Vol. 9.

(67) Williamson, P.; Ijäs, H.; Shen, B.; Corrigan, D. K.; Linko, V. Probing the Conformational States of a pH-Sensitive DNA Origami Zipper via Label-Free Electrochemical Methods. *Langmuir* **2021**, *37* (25), 7801-7809

(68) Funck, T.; Liedl, T.; Bae, W. Dual Aptamer-Functionalized 3D Plasmonic Metamolecule for Thrombin Sensing. In *Applied Sciences*, 2019; Vol. 9.

(69) Hübner, K.; Pilo-Pais, M.; Selbach, F.; Liedl, T.; Tinnefeld, P.; Stefani, F. D.; Acuna, G. P. Directing Single-Molecule Emission with DNA Origami-Assembled Optical Antennas. *Nano Letters* **2019**, *19* (9), 6629-6634

(70) Ge, Z.; Fu, J.; Liu, M.; Jiang, S.; Andreoni, A.; Zuo, X.; Liu, Y.; Yan, H.; Fan, C. Constructing Submonolayer DNA Origami Scaffold on Gold Electrode for Wiring of Redox Enzymatic Cascade Pathways. *ACS Applied Materials & Interfaces* **2019**, *11* (15), 13881-13887

(71) Funck, T.; Nicoli, F.; Kuzyk, A.; Liedl, T. Sensing Picomolar Concentrations of RNA Using Switchable Plasmonic Chirality. *Angewandte Chemie International Edition* **2018**, *57* (41), 13495-13498

(72) Daems, D.; Rutten, I.; Bath, J.; Decrop, D.; Van Gorp, H.; Ruiz, E. P.; De Feyter, S.; Turberfield, A. J.; Lammertyn, J. Controlling the Bioreceptor Spatial Distribution at the Nanoscale for Single Molecule Counting in Microwell Arrays. *ACS Sensors* **2019**, *4* (9), 2327-2335

(73) Lakowicz, J. R. *Principles of Fluorescence Spectroscopy*; Springer New York, NY, 2006, 954.

(74) Fraiji, L. K.; Hayes, D. M.; Werner, T. C. Static and dynamic fluorescence quenching experiments for the physical chemistry laboratory. *Journal of Chemical Education* **1992**, *69* (5), 424

(75) Zhang, X.; Hu, Y.; Yang, X.; Tang, Y.; Han, S.; Kang, A.; Deng, H.; Chi, Y.; Zhu, D.; Lu, Y. FÖrster resonance energy transfer (FRET)-based biosensors for biological applications. *Biosensors and Bioelectronics* **2019**, *138*, 111314

(76) Marras, A. E.; Shi, Z.; Lindell, M. G., III; Patton, R. A.; Huang, C.-M.; Zhou, L.; Su, H.-J.; Arya, G.; Castro, C. E. Cation-Activated Avidity for Rapid Reconfiguration of DNA Nanodevices. *ACS Nano* **2018**, *12* (9), 9484-9494

(77) Resch-Genger, U.; Grabolle, M.; Cavaliere-Jaricot, S.; Nitschke, R.; Nann, T. Quantum dots versus organic dyes as fluorescent labels. *Nature Methods* **2008**, *5* (9), 763-775

(78) Fu, A.; Gu W Fau - Larabell, C.; Larabell C Fau - Alivisatos, A. P.; Alivisatos, A. P. Semiconductor nanocrystals for biological imaging. (0959-4388 (Print)),

(79) Gao, X.; Yang L Fau - Petros, J. A.; Petros Ja Fau - Marshall, F. F.; Marshall Ff Fau - Simons, J. W.; Simons Jw Fau - Nie, S.; Nie, S. In vivo molecular and cellular imaging with quantum dots. (0958-1669 (Print)),

(80) Samanta, A.; Zhou, Y. D.; Zou, S. L.; Yan, H.; Liu, Y. Fluorescence Quenching of Quantum Dots by Gold Nanoparticles: A Potential Long Range Spectroscopic Ruler. *Nano Letters* **2014**, *14* (9), 5052-5057

(81) He, K.; Li, Y.; Xiang, B.; Zhao, P.; Hu, Y.; Huang, Y.; Li, W.; Nie, Z.; Yao, S. A universal platform for building molecular logic circuits based on a reconfigurable three-dimensional DNA nanostructure. *Chemical Science* **2015**, *6* (6), 3556-3564

(82) Zhang, Y.; Pan, V.; Li, X.; Yang, X.; Li, H.; Wang, P.; Ke, Y. Dynamic DNA Structures. *Small* **2019**, *15* (26), 1900228

(83) Yao, D.; Li, H.; Guo, Y.; Zhou, X.; Xiao, S.; Liang, H. A pH-responsive DNA nanomachine-controlled catalytic assembly of gold nanoparticles. *Chemical Communications* **2016**, *52* (48), 7556-7559

(84) Cox, A. J.; Bengtson, H. N.; Rohde, K. H.; Kolpashchikov, D. M. DNA nanotechnology for nucleic acid analysis: multifunctional molecular DNA machine for RNA detection. *Chemical Communications* **2016**, *52* (99), 14318-14321

(85) Monserud, J. H.; Macri, K. M.; Schwartz, D. K. Toehold-Mediated Displacement of an Adenosine-Binding Aptamer from a DNA Duplex by its Ligand. *Angewandte Chemie International Edition* **2016**, *55* (44), 13710-13713

(86) Kang, D.; White, R. J.; Xia, F.; Zuo, X.; Vallée-Bélisle, A.; Plaxco, K. W. DNA biomolecular-electronic encoder and decoder devices constructed by multiplex biosensors. *NPG Asia Materials* **2012**, *4* (1), e1-e1

(87) Yurke, B.; Turberfield, A. J.; Mills, A. P.; Simmel, F. C.; Neumann, J. L. A DNA-fuelled molecular machine made of DNA. *Nature* **2000**, *406* (6796), 605-608

(88) Seelig, G.; Soloveichik D Fau - Zhang, D. Y.; Zhang Dy Fau - Winfree, E.; Winfree, E. Enzyme-free nucleic acid logic circuits. (1095-9203 (Electronic)),

(89) Yang, X.; Tang, Y.; Traynor, S. M.; Li, F. Regulation of DNA Strand Displacement Using an Allosteric DNA Toehold. *Journal of the American Chemical Society* **2016**, *138* (42), 14076-14082

(90) Wang, W.; Guo, Y.; Tiede, C.; Chen, S.; Kopytynski, M.; Kong, Y.; Kulak, A.; Tomlinson, D.; Chen, R.; McPherson, M.; et al. Ultraefficient Cap-Exchange Protocol To Compact Biofunctional Quantum Dots for Sensitive Ratiometric Biosensing and Cell Imaging. *ACS Applied Materials & Interfaces* **2017**, *9* (18), 15232-15244

(91) Medintz, I. L.; Mattoussi, H. Quantum dot-based resonance energy transfer and its growing application in biology. *Physical Chemistry Chemical Physics* **2009**, *11* (1), 17-45

(92) Clapp, A.; Medintz, I.; Mauro, J.; Fisher, B.; Bawendi, M.; Mattoussi, H. Fluorescence resonance energy transfer between quantum dot donors and dye-labeled protein acceptors. *Journal of the American Chemical Society* **2004**, *126* (1), 301-310

(93) Hurst, S.; Lytton-Jean, A.; Mirkin, C. Maximizing DNA loading on a range of gold nanoparticle sizes. *Analytical Chemistry* **2006**, *78* (24), 8313-8318

(94) Douglas, S. M.; Marblestone, A. H.; Teerapittayanon, S.; Vazquez, A.; Church, G. M.; Shih, W. M. Rapid prototyping of 3D DNA-origami shapes with caDNAno. *Nucleic Acids Research* **2009**, *37* (15), 5001-5006

(95) Rothemund, P. Folding DNA to create nanoscale shapes and patterns. *Nature* **2006**, *440* (7082), 297-302

(96) Shaw, A.; Benson, E.; Högberg, B. Purification of Functionalized DNA Origami Nanostructures. *ACS Nano* **2015**, *9* (5), 4968-4975

(97) Tang, W.; Zhong, W.; Tan, Y.; Wang, G. A.; Li, F.; Liu, Y. DNA Strand Displacement Reaction: A Powerful Tool for Discriminating Single Nucleotide Variants. (2364-8961 (Electronic)),

(98) Zhang, D. Y.; Winfree, E. Control of DNA Strand Displacement Kinetics Using Toehold Exchange. *Journal of the American Chemical Society* **2009**, *131* (47), 17303-17314

(99) Tang, W.; Zhong, W.; Tan, Y.; Wang, G. A.; Li, F.; Liu, Y. DNA Strand Displacement Reaction: A Powerful Tool for Discriminating Single Nucleotide Variants. *Topics in Current Chemistry* **2020**, *378* (1), 10

(100) Srinivas, N.; Ouldridge Te Fau - Sulc, P.; Sulc P Fau - Schaeffer, J. M.; Schaeffer Jm Fau - Yurke, B.; Yurke B Fau - Louis, A. A.; Louis Aa Fau - Doye, J. P. K.; Doye Jp Fau - Winfree, E.; Winfree, E. On the biophysics and kinetics of toehold-mediated DNA strand displacement. (1362-4962 (Electronic)),

(101) Šulc, P.; Ouldridge, T. E.; Romano, F.; Doye, J. P.; Louis, A. A. Modelling toehold-mediated RNA strand displacement. (1542-0086 (Electronic)),

(102) Haley, N. A.-O.; Ouldridge, T. A.-O.; Mullor Ruiz, I.; Geraldini, A.; Louis, A. A.; Bath, J.; Turberfield, A. A.-O. Design of hidden thermodynamic driving for non-equilibrium systems via mismatch elimination during DNA strand displacement. (2041-1723 (Electronic)),

(103) Amodio, A.; Del Grosso, E.; Troina, A.; Placidi, E.; Ricci, F. Remote Electronic Control of DNA-Based Reactions and Nanostructure Assembly. *Nano Letters* **2018**, *18* (5), 2918-2923

(104) Ranallo, S.; Sorrentino, D.; Ricci, F. Orthogonal regulation of DNA nanostructure self-assembly and disassembly using antibodies. *Nature Communications* **2019**, *10* (1), 5509

(105) Zhang, D. Y.; Winfree, E. Control of DNA Strand Displacement Kinetics Using Toehold Exchange. *Journal of the American Chemical Society* **2009**, *131* (47), 17303-17314

Chapter 4:

Designer Assemblies of Magnetic Nanoparticles on DNA Templates

4.1 Abstract

In order to create novel phases of magnetic nanoparticles (MNPs) that can enable collective phenomena for applications like data processing and information storage, this research project aims to achieve this by using DNA. As magnetic nanostructures in proximity interact, they exhibit a variety of collective behaviors, such as super spin glass,[1] super-ferromagnetism,[2] spin ice,[3] and spin-wave propagation. [4] For example, a two-dimensional array of interacting ferromagnetic nanostructures show a long-range correlation of spins with exotic phase transitions at different temperatures. It should be noted that many of these phases are composed of larger ferromagnetic structures. [5] It is not yet possible to enable analogous phases that are composed of superparamagnetic nanoparticles, which are small enough (5-25 nm for Fe_3O_4) to allow the magnetization to randomly flip directions. These structures are not amenable to traditional lithographic techniques. Providing a facile method to control particle interactions by assembling MNPs on substrates capable of forming a wide range of geometries as well as interparticle spacings can open a new window to the emergence of new physics by accessing magnetic phases that are not accessible through conventional assembly methods. Self-assembly of MNPs can also provide a new route to channel spin wave propagation, which is one of the current challenges of applying spin-waves for information processing. To precisely control the geometry and the interparticle distance of assembled particles, I use DNA ligands with special designs that can connect functionalized magnetic nanoparticles through hybridization (Figure 1). A DNA lattice has been successfully used to assemble gold nanoparticles in three dimensions. [6-8] However, only a couple of attempts have been reported for MNPs due to the lack of means to functionalize MNPs with DNA. The first step to making a 3D lattice of MNPs is to synthesize monodispersed particles with a narrow size distribution within the superparamagnetic range. The desired size for our purpose is ~15 nm, in which Fe_3O_4 is superparamagnetic and facilitates further self-assembly procedures. Here I designed a method to functionalize the surface of the MNPs with DNA. The strong affinity between gold and sulfur in our thiol modified-DNA allowed us to functionalize the particles by adding a thin gold shell to the magnetic core. My designed model is a useful tool for studying the interaction and repulsion forces in superlattice structures, as well as the collective magneto plasmonic behavior of these nanoparticles that are bound by geometrical frustration.

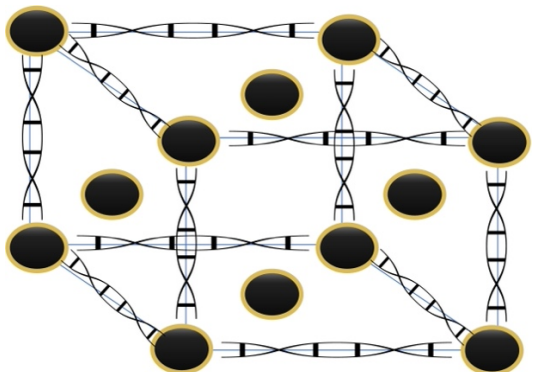

Figure 35. DNA assisted self-assembly of gold coated magnetic nanoparticles into a superlattice.

4.2 Introduction

The interactions between magnetic dipoles in magnetic nanostructures give rise to a variety of complex collective behaviors, one of which is known as spin ice. In spin ice, magnetic dipoles arrange themselves in a tetrahedral geometry, forming "spinons," and leading to the emergence of magnetic monopoles. To study and control these interactions, artificial spins have been created using advanced nanofabrication techniques. These enable researchers to engineer and manipulate magnetic interactions, leading to the discovery of novel collective behaviors and potential applications in spintronics and quantum computing.

In recent years, a significant number of experiments have been conducted to explore the unusual physics of spin ice models. These investigations have utilized a variety of methods, including lithographically patterned two-dimensional arrays of ferromagnetic permalloys, [9] colloidal system, [10] and Nano-disks. [11] These techniques have allowed for the creation of different geometries and the direct control of collective dynamics, leading to the realization of exotic phases that are not found in nature. To understand spin-ice models, we must first discuss the concept of frustration. In physical systems, "frustration" refers to the inability of the system to minimize the energy of all interactions simultaneously, leading to a large degeneracy of low-energy states and non-zero entropy at absolute zero. Geometrical frustration can be illustrated by considering the spins on a triangular lattice with antiferromagnetic interactions (Figure 2). The spins prefer to align antiparallel, but once two spins are aligned, the third spin cannot simultaneously satisfy its favorable antiparallel alignment with each of the nearest neighbor spins. The spin in question is thus "frustrated" since it cannot determine which way to point.

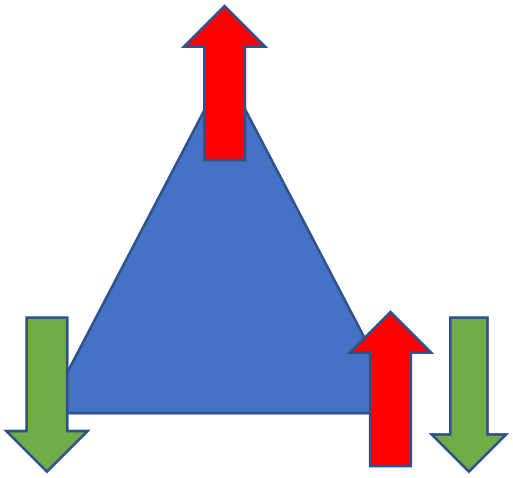

Figure 36. Geometrical frustration

Two-dimensional arrays of ferromagnetic materials are well-known tools to experimentally model Ising spin [12] systems. Artificial spin ice (ASI) refers to an array of engineered magnetic nanostructures that mimic the behavior of natural spin ice. These arrays can be designed to exhibit spin-ice-like behavior to study the fundamental properties

of spin-ice systems. They are typically composed of an array of nanomagnets that are patterned into a two-dimensional lattice or a three-dimensional structure.[5, 11-15] The nanomagnets in an artificial spin ice array interact with each other through dipole-dipole interactions, which can be engineered to create magnetic frustration and emergent magnetic monopoles, similar to the behavior seen in natural spin ice materials. However, the geometry and size of the nanomagnets can be precisely controlled, allowing for the creation of different types of spin ice states and the manipulation of magnetic monopole dynamics. Since the first generation of fabricated ferromagnetic permalloy artificial spin ice in 2006,[15] many theoretical and experimental models have been developed to mimic the spin ice behavior in bulk spin ices such as $HoTi_2O_7$ and Dy_2TiO_7,[16-19] and uncover the nature of their exotic behavior. These models have revealed remarkable phenomena, such as the collective freezing of spins into low-energy states and the presence of magnetic monopoles,[10] spin charges,[11] and Coulombic phases,[20, 21] all of which are caused by geometrical frustration in the system. In such models, by designing the lattice geometry and controlling the strength of dipolar interaction within the system, researchers have been able to lift the degeneracy of the ground state and realize exotic phases in physics, *e.g.* charge-ordered state (spin liquid) experimentally (Figure 3). [13, 22]

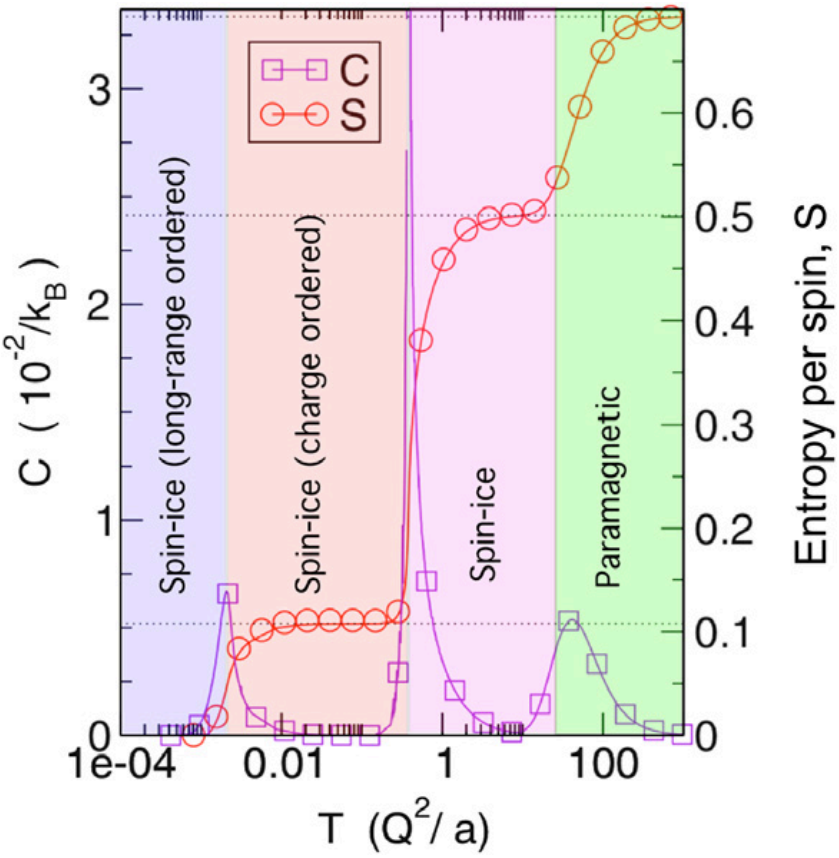

Figure 37. phase transitions in Kagome Spin Ice model.[8]

Accessing lower energy states with ASIs is still difficult due to the large amount of thermal energy (~10^5 K) needed to break through the energy barrier within the common size range (200-800nm) of magnetic domains created using lithography techniques.[3, 23,24] Recently, a few studies have tried to achieve this by decreasing the thickness of nanopatterns and working in a thermally active state.[25] Even though this represents major progress, new models need to be introduced to fully understand the dynamics of spin collective behavior and reach inaccessible lower energy states that may have rich many-body physics. Using smaller components (10–100 nm) referred to as "superparamagnetic nanoparticles" and arranging them in a way that induces geometrical frustration could be another way to achieve analogous lower energy phases.

4.2.1 Superparamagnetic nanoparticles

The use of superparamagnetic particles could provide a novel platform for the investigation of geometrical frustration and the exploration of the dynamic of spin configuration at lower energy levels. Superparamagnetic nanoparticles are a class of nanoparticles that exhibit unique magnetic properties due to their small size and shape. These nanoparticles typically have diameters ranging from 1 nm to 10 0nm, and their magnetic behavior is strongly influenced by thermal fluctuations. In superparamagnetic nanoparticles, the magnetic moments of individual atoms or ions are strongly coupled, resulting in a net magnetic moment for the particle. However, at room temperature or above, thermal energy can cause the magnetic moments to randomly flip directions, leading to a loss of net magnetic moments. This phenomenon is known as superparamagnetism (Figure 4).

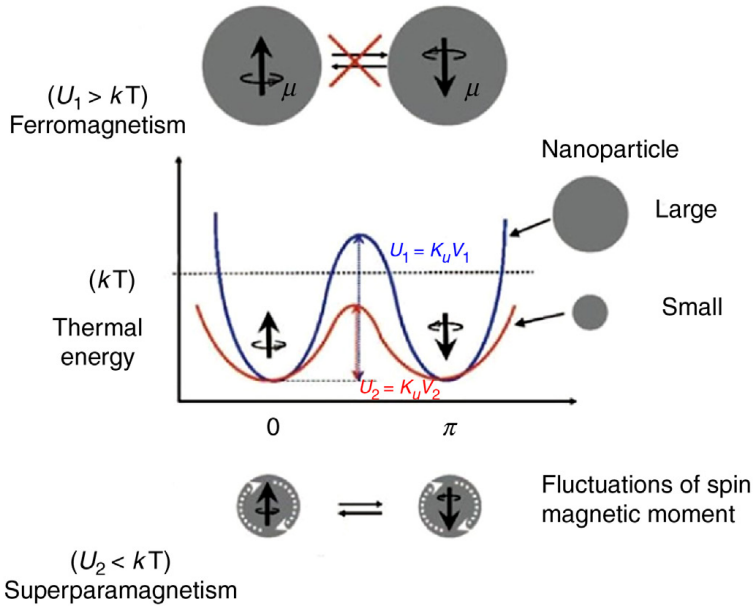

Figure 38.Superparamagnetism and the effect of size of the particle in magnetization reversal energy barrier.

As a direct consequence of their small size, superparamagnetic particles allow the magnetization to randomly flip directions, making them distinct from their ferromagnetic counterparts and a novel system to study collective magnetic behavior. Due to their small sizes, these structures are not amenable to traditional lithographic techniques. Moreover, lithographic techniques, which are fundamentally 2D in nature, are not compatible with 3D architectures. An alternative to these top-down lithographic approaches that can address these limitations are bottom-up approaches that organize colloidal magnetic nanoparticles into superlattices. Previous studies on the self-assembly of superparamagnetic nanoparticles have included the formation of 2D monolayers through the Langmuir Blodget technique, solvent evaporation,[26, 27] dispersion in a granular polymer,[28] magnetic field-assisted assembly,[29] or template-assisted self-assembly in which a porous membrane or a chemical structure, such as a molecule, that is used to anchor the nanoparticles in place serves as a template. These methods have produced interesting collective phases such as spin glass and super-ferromagnetism. However, unlike lithographically produced phases, these self-assembled systems have very limited control over the geometrical arrangement. As a result, the vast majority of possible interesting magnetic phases, such as spin ice, remain inaccessible with such assemblies.[27,28,29]

In this context, a facile bottom-up method capable of forming a wide range of geometries as well as interparticle spacings can open a new window to the emergence of new physics by accessing magnetic phases that are inaccessible through conventional assembly methods. The smaller size of these particles can address some of the current problems in spin ice model studies: For example, the small size facilitates exploring the effect of thermal fluctuation and changes the energy landscape by minimizing the energy barrier. This new platform may allow the introduction of defect at will and enable the study of the dynamics of spin reconfiguration. DNA-directed self-assembly of nanoparticles by

a bottom-up method could potentially address some of these problems by providing a simple and efficient method for self-assembling nanoparticles with a high degree of control and specificity. This process involves using complementary DNA strands to direct the assembly of nanoparticles, which enables researchers to precisely control their position, orientation, and connectivity. As a result, complex structures with well-defined geometries and properties can be formed.[29-31] While this technique has been widely used to assemble various metallic and semiconductor nanoparticles, not until recently had any attempts been made to self-assemble magnetic nanoparticles through DNA-directed self-assembly.[32, 33] In the sections that follow, I will delve further into these intricate magnetic systems, as well as review recent attempts to self-assemble magnetic nanoparticles using DNA-directed self-assembly, and finally present my plan for resolving some of the problems that are currently associated with these systems.

4.2.2 Crystallization of magnetic nanoparticles

DNA hybridization between DNA-functionalized nanoparticles provides a powerful strategy to regulate superlattice crystallization behavior. This allows access to complex three-dimensional structures with over 30 distinct lattice symmetries. The inherent electrical characteristics of the basic atomic building blocks determine the structure of atomic crystalline solids in nature. As a result, tremendous efforts have been made in order to comprehend these features and build principles that allow one to understand the thermodynamically favorable crystal forms, with limited success. For example, Pauling's principles for ionic solids allow one to understand crystallization behavior but not to create crystal architecture because the options are intrinsically linked to the identities of the elemental building blocks (such as cations and anions).[34, 35] Similarly, the shapes of colloidal crystals for nanoscale systems are controlled by the sort of bonding interactions caused by diverse surface ligands, but unlike atoms, their bonding behavior can be dissociated from the particle's compositional identity. Previous reports have demonstrated that DNA-NPs can be compared to programmable atom equivalents (PAEs), which have bonding properties that coincide with the oligonucleotide sequence.[31, 36, 37] When compared to atomic systems, the crystallization behavior of PAEs is identical to that of ionic crystals, where DNA hybridization interactions can cause particle attraction similar to charge attraction between cations and anions in ionic crystals. Over a broad design space, one can apply the general premise that the structure with the greatest number of hybridization (attractive) interactions will be the most thermodynamically favorable structure.[7, 38]

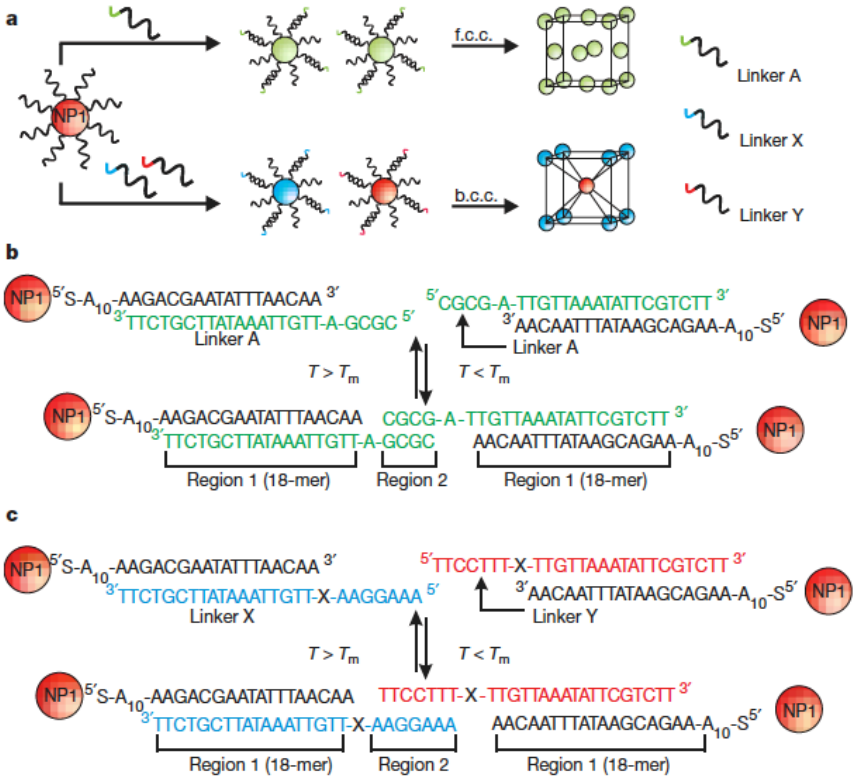

Figure 39. crystallization of AuNPs in fcc and bcc superlattices by careful design of different DNA linkers.[30]

As previously stated, many studies have focused on the DNA-assisted self-assembly of gold nanoparticles in 3D superlattice structures; however, until recently, the self-assembly of magnetic nanoparticles in superlattice structures and the effect of magnetic dipole-dipole interaction on the crystallization of the nanoparticle, with and without the application of a magnetic field, were unknown. The first study on this matter was published by Mirkin Group in 2020.[29] In their study, they functionalized spherical iron oxide magnetic nanoparticles of 10 nm, 20 nm, and 25 nm in size with an azide-bearing capping polymer, N3-PMAO, to covalently attach dibenzocyclooctyl (DBCO)-terminated DNA to the azide on the magnetic nanoparticles. Then, through a thermal annealing from 65ºC to room temperature, they crystallized the nanoparticles in the presence and absence of a magnetic field. And the crystal structures were further characterized with SEM imaging and SAXS measurement (Figure 6).

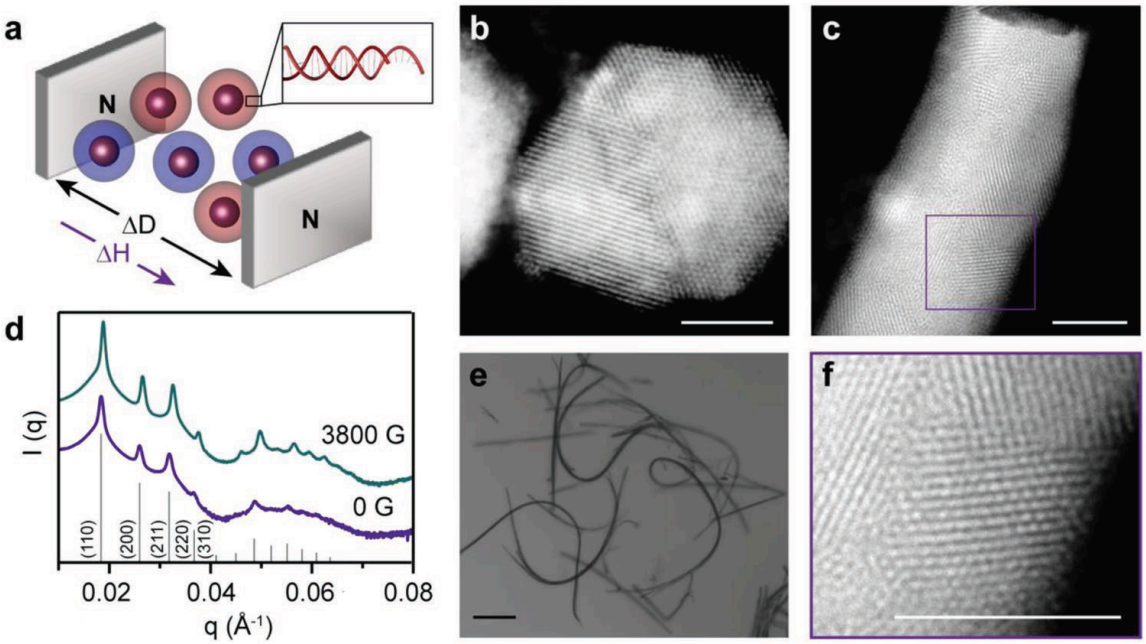

Figure 40.a)Schematic depicting the assembly of Fe_3O_4 nanoparticles DNA functionalized in within a magnetic field. STEM of b) bcc superlattice without of a magnetic field of 20 nm Fe3O4 c-e) bcc crystal formed with the same particles in the presence of a 3800 G magnetic field d) Representative 1D SAXS patterns reveal that the bcc crystal is formed during slow cooling crystallization when no field (0 G) and a field of 3800 G are applied.

The study showed that an applied magnetic field can control the anisotropic growth of iron oxide magnetic nanoparticle crystals. By using experiments and computations, they developed a method for forming elongated structures by combining short-range DNA hybridization interactions with long-range magnetic dipole-dipole coupling interactions.

In another study by the same group,[39] they used the same functionalization protocol to crystallize cubic iron oxide magnetic nanoparticles to adjust the face-to-face interaction between the nanoparticles and study the effect of intrinsic magnetic anisotropy on the intraparticle interactions and slow cooling crystallization. Their results revealed that utilizing DNA as a ligand permits cubic Fe_3O_4 NPs to form with symmetry and orientation that non-specific, oleate ligands cannot achieve. They also found that, even when the lattice symmetry and interparticle spacing are modified, the NP core impacts orientation across all length scales. Although they were unable to determine how magnetic dipole coupling produces such a result, their work established the foundation for the structural characterization and material synthesis required to investigate other shapes and symmetries in magnetic NP nanoparticle crystallization, as well as their effects on crystallographic alignment in magnetic fields. Despite the ability to form these ordered structures from magnetic nanoparticles, the surface functionalization requires coating the nanoparticles with a polymer and then conjugating DNA to the polymer. This complex process is challenging to implement and the polymer shell reduces the dipolar coupling between magnetic NPs.

Here using the well-established Au-S surface chemistry, we are conjugating thiolated DNA to magnetic nanoparticles coated with a 1-2 nm thick gold shell. By utilizing the direct linkage self-assembly techniques, careful control over reaction parameters including salt concentration and controlled thermal annealing we crystalize superparamagnetic nanoparticles into a fcc superlattice. Our findings demonstrate that using our novel method 3D ordered structures could be formed by controlling the annealing temperature and salt concentration. silica encapsulation also eventually generates rigid, stable structures which could be characterized with Scanning electron microscopy. Our research opens up new avenues for studying magnetic interactions and how different lattice symmetries may be modulated by dipole-dipole interactions between nanoparticles. It also facilitates magneto plasmonic studies, allowing one to tune the magnetic and plasmonic interactions by varying the gold shell thickness, the length of the DNA ligand, and the application of a magnetic field.[40-42]

4.3 Experiment and Methods

4.3.1 Synthesis of magnetic nanoparticles

The thermal decomposition approach was used to synthesize Fe_3O_4 MNPs.[43] First, 35 mL of diphenyl ether solution containing 0.3 M of 1-hexadecanol, 0.3 M of oleic acid, and 0.3 M of oleylamine were heated to 200 °C with vigorous stirring in an inert environment. After reaching that temperature, 10 mL of a 0.15 M solution of [$Fe(acac)_3$] in diphenyl ether was promptly added, and the mixture was then heated to reflux at 265ºC for 2 hours with stirring to allow nucleation to occur. The reaction mixture was then cooled to room temperature and stirred for 18 hours. The black nanomaterial that resulted was subsequently precipitated by adding 50 mL of ethanol to the reaction liquid and magnetically separated. Finally, the precipitate was washed three times with ethanol and redispersed in 5 mL of anhydrous toluene.

4.3.2 Reagents

Iron (III) acetylacetonate ([$Fe(acac)_3$], 97%), diphenyl ether (99%), hydrogen

Tetrachloroaurate (III) trihydrate (HAuCl4·3H2O, ≥99.9%), oleylamine (70%), oleic acid (90%), 1-hexadecanol (95%), Ultrapure water was used throughout this work, purified with a Milli-Q system.

4.3.3 Synthesis and surface coating of iron oxide magnetic nanoparticles

The Fe_3O_4:$HAuCl_4$ (1:4) molar ratio was used to prepare the core-shell gold-coated iron oxide MNPs. In brief, 1.25 mL of anhydrous toluene colloidal dispersion of Fe_3O_4 MNPs was diluted with 20 mL of anhydrous toluene and heated to 100°C in an inert environment. Then, under vigorous stirring, a solution of $HAuCl_4.3H_2O$ (0.1956 g) and

oleylamine (4.89 mL) in anhydrous toluene (20 mL) was gently added dropwise. The reaction mixture was agitated for 1 hour at 100 °C, resulting in a dark purple color. The system was then cooled to room temperature before 50 mL of ethanol was added to precipitate the resultant nanomaterial. Finally, the gold-coated Fe_3O_4 MNPs were magnetically separated, washed with ethanol multiple times, and redispersed in 10 mL of anhydrous toluene, yielding dark purple dispersions. TEM and DLS were used to characterize the functionalized particles.

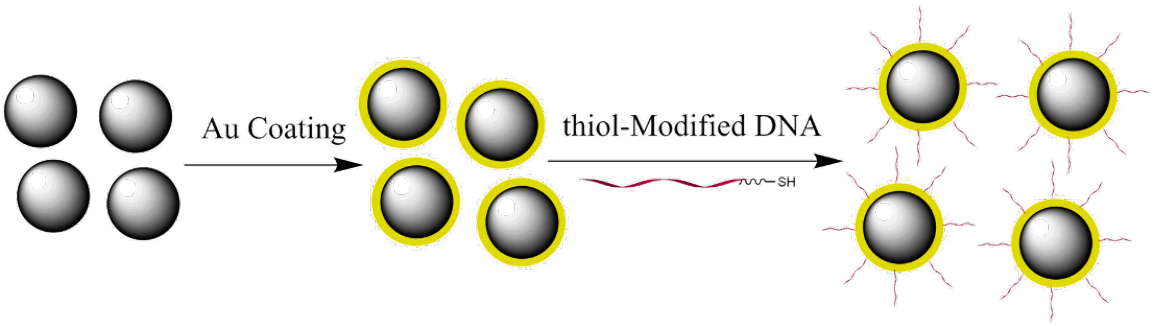

Figure 41. schematic showing the synthesis, gold coating, and DNA functionalization process.

4.3.4 Preparation of the DNA ligand

The disulfide bonds of 28-nt $^{5'}$(AAG AAT TTA TAA GCA GAA)-A_{10}-$C_3SH)^3$ modified oligonucleotides (from IDT DNA) were cleaved by mixing 100 µM of oligonucleotides with 100 mM tris(2-carboxyethyl) phosphine (TCEP) in a 1:600 ratio and leaving them at room temperature overnight. The TCEP-reduced 28-nt DNA was purified with a 3K Da Amicon Ultra-0.5 Centrifugal Filter (Millipore Sigma, Burlington, MA, USA) two times at 14000× g for 20 minutes, and the concentration was measured with a Thermo Scientific Nanodrop spectrophotometer.

4.3.5 Functionalization of Iron oxide magnetic nanoparticles with DNA

The salt-aging method developed by Mirkin *et al.* [44] was used to conjugate gold nanoparticles with DNA. Inspired by this method, since the magnetic nanoparticles are gold-coated, we used a similar strategy to functionalize the iron oxide nanoparticles with DNA. Thiol-modified oligonucleotides of 28 nt. 5' (AAG AAT TTA TAA GCA GAA)-A_{10}-C_3SH) 3' were treated with TCEP (600X) overnight to cleave the disulfide bond and purified with a 3K Da Amicon Ultra-0.5 Centrifugal Filter (Millipore Sigma, Burlington, MA, USA) two times at 14000×g for 20 minutes, and the concentration was measured with a NanoDrop^{TM} spectrophotometer. Then the oligonucleotides were mixed with 10 nm AuNPs at a molar ratio of 3000:1. After the addition of 1 µl 10% (w/v) SDS, a 5 M NaCl solution was added to the mixture to gradually increase the final concentration of NaCl in the mixture to 0.3 M over 3 hours. The mixture was then purified using a 100K Da Amicon Ultra-0.5 Centrifugal Filter eight times at 14000×g for five minutes.

4.3.6 Design of the DNA ligands for fcc superlattice

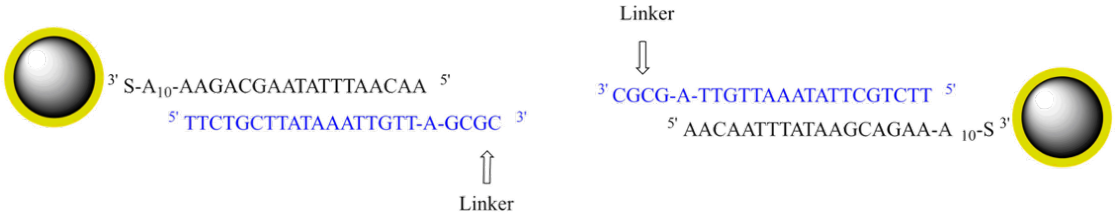

Figure 42. the design of the DNA ligand and the linker to make fcc superlattice.

4.3.7 Silica Encapsulation

Developed by Chad Mirkin and his research group, the silica encapsulation of gold nanoparticle superlattice structures is a process in which the superlattice structure is encapsulated within a silica shell through a sol-gel process. [7, 45] In this process, a solution of silica precursor molecules is mixed with the superlattice structure and allowed to polymerize, forming a solid silica shell around the gold nanoparticles. The precursor molecules typically used in the process are organosilanes, such as tetraethylorthosilicate (TEOS), which are hydrolyzed in the presence of water and an acid catalyst to form reactive silanol groups. These silanol groups then condense with one another to form silica chains, which eventually cross-link to form a solid, three-dimensional silica network. During the sol-gel process, the superlattice structure is dispersed in the silica precursor solution, and the nanoparticles become embedded in the growing silica network as it forms around them. The DNA strands on the surface of the gold nanoparticles act as templates for the silica polymerization, helping to direct the growth of the silica shell around the superlattice structure. Overall, the silica encapsulation of gold nanoparticle superlattice structures is a complex, multistep process that requires careful control over the reaction conditions to ensure the formation of a stable, functional material. However, the resulting structures have a wide range of potential applications in fields such as nanotechnology, material science, and biomedicine.

In short, this process is as follows: after the formation of nanocrystals through thermal cooling, the precipitated particles were separated from the supernatant, and they were then resuspended in 2.5 mM phosphate buffer (pH = 7.4) and 0.5 M NaCl in a volume of 1 ml. The samples were agitated at 600 rpm for 20 min with 2 µL of N-trimethoxysilylpropyl-N, N, N-trimethylammonium chloride (50 percent in methanol, Gelest, Inc.). The mixture was then agitated at 600 rpm for the remainder of the night at room temperature before 4 µL of Tetraethyl Orthosilicate (Sigma-Aldrich) was added. After a final resuspension in water and three centrifugations (10 s, 10000 rpm), the samples were put onto carbon-coated TEM grids (Ted Pella, Inc.). [46]

4.3.8 SEM imaging

Scanning electron microscopy (SEM) imaging of the superlattices was carried out using a Zeiss Gemini SEM 500 scanning electron microscope operating at 3 kV. Typically, 4-5 μl of the sample was deposited onto a plasma-treated silicon wafer, let dry overnight at room temperature, and imaged the next day.

4.3.9 DLS measurements

All dynamic light scattering (DLS) experiments were performed using the ZETASIZER NANO Series S90 (Malvern Panalytical). Measurements were done using a 50 μL microvolume quartz cuvette and a 632.8 nm laser with a 90^{o} scattering angle at room temperature.

4.3.10 X-Ray Photoelectron Spectrometry (XPS)

X-Ray Photoelectron Spectrometry was done using a Nexus X-Ray Photoelectron Spectrometer equipped with a monochromated, micro-focused, low-power Al Ka X-ray source and a 180°, double-focusing, hemispherical analyzer with a 128-channel detector. For sample preparation, 20 μL of the colloidal solution of the nanoparticles was drop-casted on a glass slide and dried over night at room temperature.

4.3.11 SAXS Measurements

Synchrotron small-angle X-ray scattering (SAXS) measurements were performed at SLAC National Accelerator Laboratory with beam line 1-5 and the Dectris Pilatus 1M (SAXS) detector. The investigations took place at an X-ray wavelength of 1.24 (10 keV). Two sets of slits were utilized to collimate and define the beam, and a silver behenate standard was employed to calibrate the sample angle. To position the samples in the beam's path, 1.5mm quartz capillaries (made by Charles Supper Company, Inc.) were aliquoted. A CCD area detector was used to measure the scattered radiation, and exposure times to the sample ranged from 0.1 to 1 second. The 1D SAXS diffraction patterns were calculated from the 2D scattering patterns, which were azimuthally averaged at each reflection peak. The scattering intensity, I(q), against the scattering, q, was plotted using the formula $q = (4 \sin\theta)/\lambda$ where θ is half of the scattering angle and λ is the wavelength of X-ray radiation and half of the scattering angle. The capillary, buffer, and DNA scatter orders of magnitude lower than the Au and Fe_3O_4 nanoparticles, hence the latter were all regarded as insignificant for the total SAXS data.

4.3.12 Crystallization of magnetic nanoparticles

The method developed was based on previous methods for the formation of AuNP superlattices, with modifications. [7, 45] Excess DNA was removed from DNA-functionalized

MNPs using three rounds of centrifugation, with each round followed by supernatant removal and redispersal of the resultant DNA MNPs pellet in 0.01 % SDS. After the final centrifugation and supernatant removal, nanoparticles were redistributed in 2.5 mM phosphate buffered saline (PBS), 0.5 M NaCl, and 0.1 % SDS. The concentrations of NaCl and PBS are then adjusted to the desired values (described in the following section) before adding the linker to ensure that the nanoparticles are stable and do not precipitate. Then, at room temperature, the MNP solutions were mixed with DNA linkers with a self-complementary sticky end (5'GCGC3'). In most cases, DNA linkers were introduced in a 50:1 ratio to the number of DNA strands covalently connected to MNPs. After mixing the DNA linkers, the solution mixture was allowed to settle at 25 °C for 30 minutes to achieve maximum aggregation. To promote the formation of double-stranded DNA helices consisting of the DNA linker and the corresponding sequence, the solution was heated to 70 °C and then slowly cooled back to 25 °C at a cooling rate of 0.1°C every 10 minutes. A 96-well thermal cycler was used for all slow-cooling experiments. The entire slow cooling process usually takes about 3 days to finish.

4.4 Results and Discussion

4.4.1 Iron oxide nanoparticle synthesis

Thermal decomposition was used to successfully create the magnetic iron oxide nanoparticles. This synthesis approach offers a flexible platform for the production of oxide-based nanoparticles, particularly iron oxide nanoparticles, by thermally decomposing organometallic precursors in organic solvents with surfactant capping agents in an inert atmosphere. The size, polydispersity, and shape of the nanoparticles can be controlled by altering the ratio between the capping reagent or surfactant, the kind and quantity of the organic solvent, as well as the temperature. For instance, some researchers have indicated that the smaller the particle, the higher the ratio of the surfactant and solvent to the precursor. [47] The reason for this is that in the thermal decomposition reaction synthesis of Fe_3O_4 nanoparticles, a decrease in solvent volume causes early saturation of the oxide-based nuclei, allowing more reactants to participate in the growth process, which results in larger particles. When the solvent volume is larger, more nuclei are required to accomplish saturation at the expense of the iron salt precursor, resulting in smaller Fe_3O_4 nanoparticles. A similar idea can be used to explain the surfactant effect. In high surfactant/metal ratios, more surfactant is equivalent to a larger volume of solvent, and more nuclei are required to reach saturation, resulting in small nanoparticles. Larger particle sizes are also a result of higher temperatures. [43, 48] The TEM image of the monodispersed nanoparticles is shown in Figure 9a. The hydrodynamic size of the nanoparticles is illustrated in Figure 8b, both measurements consistently show a mean particle size of ~10 nm, despite a relatively small DLS aggregation peak near 70 nm.

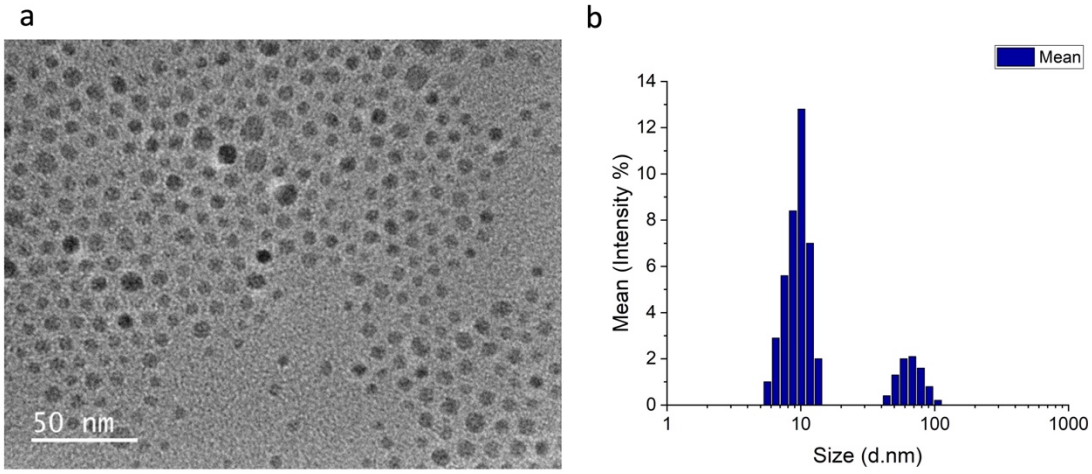

Figure 43a. a) TEM image of iron oxide magnetic nanoparticles. The average size according to TEM is around 11 nm in diameter. Characterization is done with TEM JEM 2010 imaging. B) dynamic light scattering of iron oxide nanoparticles.

4.4.2 Gold coating of magnetic nanoparticles

At neutral pH, Fe_3O_4 NPs have a low surface charge and a high surface area to volume ratio, which often causes aggregation. Iron oxide (Fe_3O_4) nanoparticles are commonly produced by thermal decomposition methods. In the presence of oleic acid and oleylamine, the iron precursor is effectively reduced with 1,2-hexadecanediol to produce small, monodispersed Fe_3O_4 nanoparticles. Gold coating of iron oxide nanoparticles is also done through a thermally active hetero-interparticle coalescence method by using oleylamine and oleic acid as capping agents. [49] The control of several factors, including the rate of reaction temperature increase, reaction time, and precise reaction temperature control, is essential for the successful synthesis of core-shell nanoparticles. Based on previous studies, temperature is expected to play a key role in both the partial desorption of the Fe_3O_4 nanoparticle stabilizing agents and the ability of the reduced gold precursor to directly coat the exposed iron oxide nanoparticles. The partial desorption of the capping agents only occurs at a specific temperature, and if the temperature is increased too fast, the Fe_3O_4 NP surface cannot act as a nucleation site for gold coating, and Au nanoparticles may begin to form instead. Therefore, for a successful coating, the temperature must be raised slowly in 10 ^oC/min increments until it reaches 180-190 ^oC. [50, 51] The solution must be maintained at this temperature for another one and a half hours for complete shell formation. Studies have also shown that the shell thickness could be controlled by careful adjustment of the Au:Fe_3O_4 ratio.[52] The gold coating of iron oxide nanoparticles was done by reduction of an Au precursor ($HAuCl_4$) at a 1:4 ratio, which was used to fully coat the surface of the MNPs. The nanoparticles were then purified three times using a rare earth magnet and redispersed in anhydrous toluene.

The SEM image of gold-coated nanoparticles is shown in Figure 10. The average size of the nanoparticles is increased by ~3 nm, leading to an overall size of 13.4±1.7 nm. To make sure these particles are not gold nanoparticles generated during the gold coating, a STEM-EDX measurement was performed.

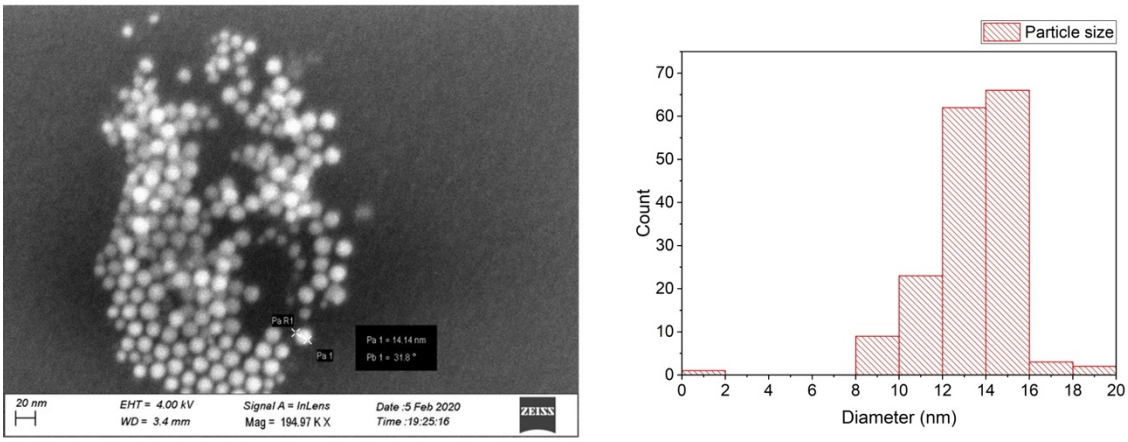

Figure 44. SEM micrograph of Fe_3O_4@Au at 3kv, the size of the particles is 13.4±1.7 nm.

Scanning transmission electron microscopy (STEM-EDX) energy dispersive X-ray analysis on discrete particles (Figure 11) reveals the colocalization of Au, oxygen, and Fe signals as well as the smooth and nearly spherical morphology. Therefore, these results showed that gold was successfully coated onto the Fe_3O_4 nanoparticles.

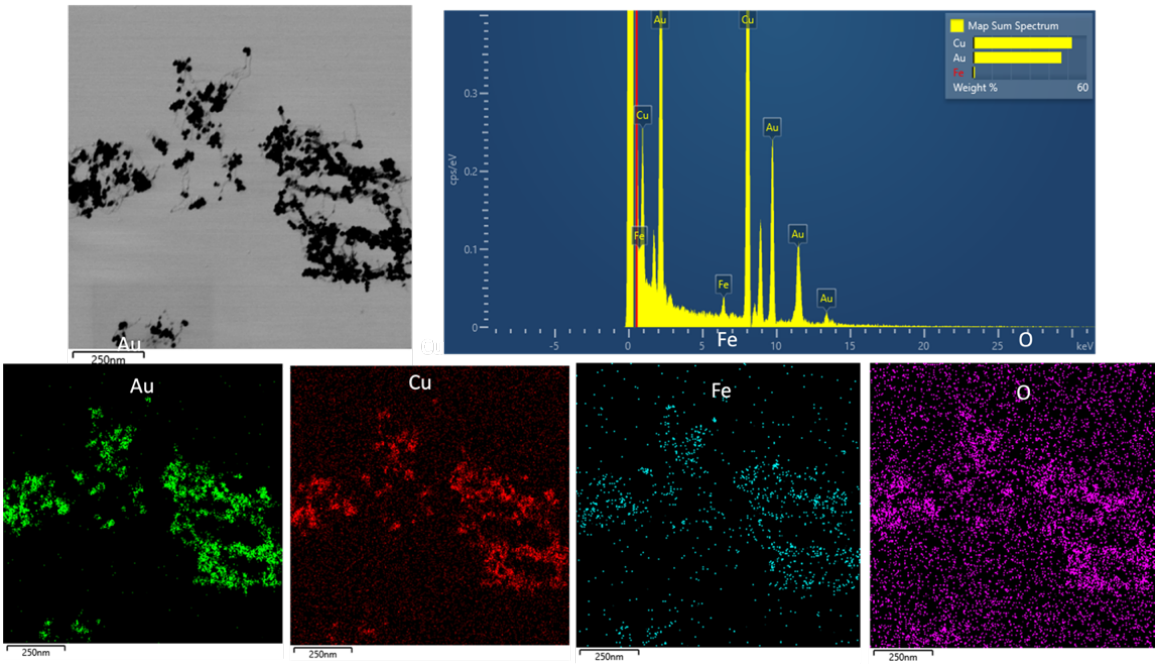

Figure 45. Scanning transmission electron microscopy (STEM-EDX) energy dispersive X-ray analysis on gold-coated MNPs. The elemental analysis shows the presence of Au, Fe, and oxygen.

The gold-coated MNPs were then functionalized with DNA in a one-step phase transfer ligand exchange shown in Figure 12. For this phase transfer reaction, thiol-modified DNA ligands in water with 0.01% SDS were mixed with Au@Fe_3O_4 magnetic nanoparticles in toluene and shaken overnight to reach maximum DNA loading. Unfortunately, lack of access to ICP makes it impossible to find the precise concentration of synthesized Au@Fe_3O_4 and therefore adjust the DNA:MNP ratio to get monodispersed nanoparticles. Gold-coated nanoparticles purchased from Nanopartz were used for superlattice formation.

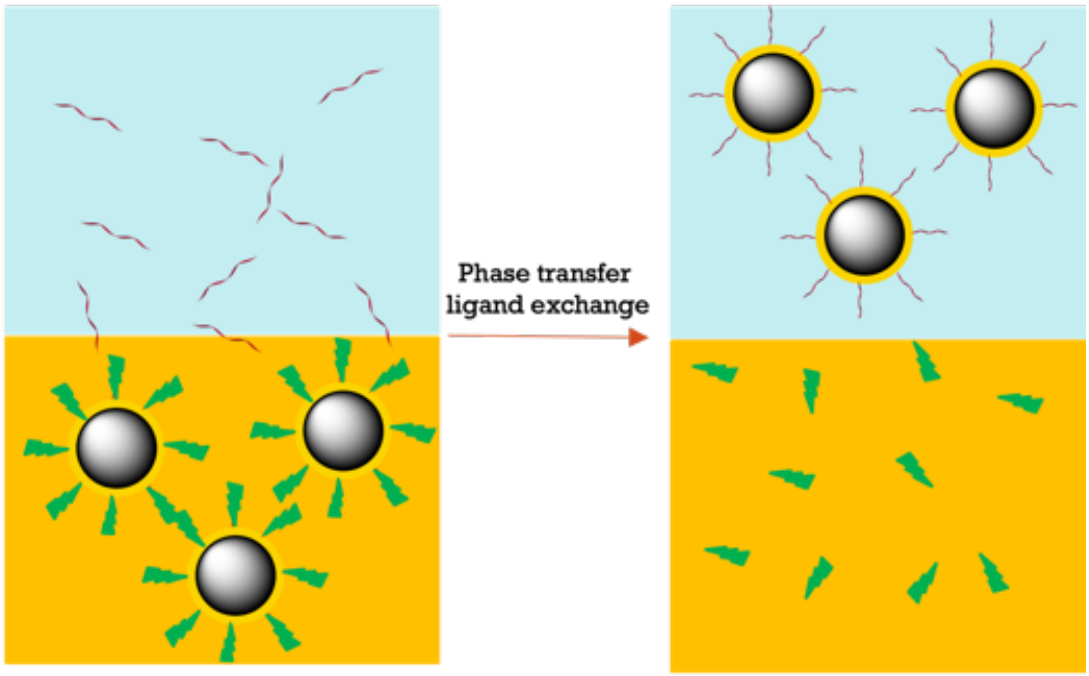

Figure 46. Schematic of DNA functionalization of gold-coated magnetic nanoparticles by phase transfer ligand exchange.

XPS analyses of the 10 nm iron oxide nanoparticles and the 13 nm gold-coated iron oxide nanoparticles are shown in Figure 13. The oxygen 1S peak was observed at around 530 eV, which could be attributed to the core iron oxide nanoparticles. Spin orbital doublets Au 4f $^{5/2}$ and Au 4f $^{7/2}$ appeared for the gold-coated particles with signals at binding energy values of 83.35 and 84.95 eV, which are known oxidation values of gold in the ground state. The bands at 710.0 eV and 724 eV, respectively, were attributed to the Fe $2P^{3/2}$ and $2P^{1/2}$ states, which correspond to the bulk iron ground state.

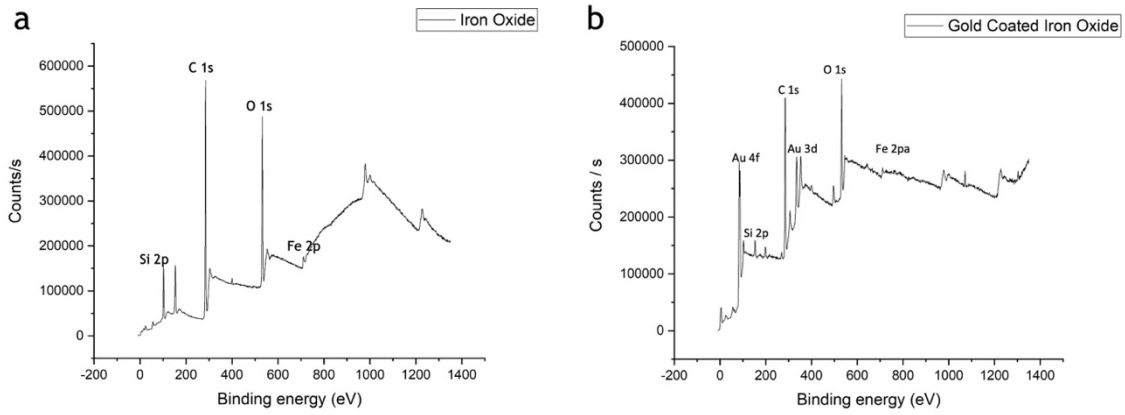

Figure 47.XPS measurement of iron oxide (a) and gold coated iron oxide (b).

4.4.3 DNA directed crystallization of gold-coated magnetic nanoparticles

4.4.3.1 The effect of temperature

The starting temperature of the slow cooling crystallization and the rate of cooling were initially chosen based on previous reports on the crystallization of AuNPs.[30, 37, 45, 46, 53] In these studies, first the Au nanoparticles are precipitated through DNA-assisted self-assembly, then through a thermal denaturation, the aggregates are gradually heated from room temperature while monitoring the absorbance at 520 nm at a rate of 0.25 degrees per minute. The absorbance peak at 520 nm indicates that particles are dispersed in the solution, and the temperature at which this transition takes place is the superlattice's melting point. Based on these studies, I tested temperatures in a range of 52-65^{o}C. The products of the thermal anneal were then imaged using SEM. At these temperatures, no ordered structures were observed (Figure 13). This disagreement with the literature shows that the T_m of these structures was above 65 ^{o}C, which could possibly be due to magnetic attraction between these particles, raising the melting temperature. Also, the tested particles were about 20 nm in size, making the magnetic interaction stronger compared to the smaller nanoparticles studied in these reports. Therefore, the temperature was eventually raised to 70^{o}C, at which superlattice crystals were observed (Figure 14.b).

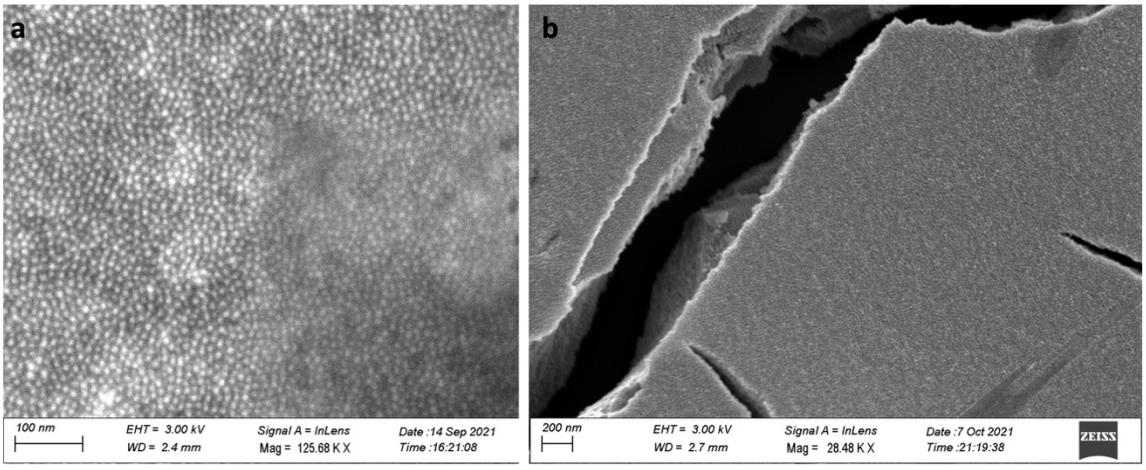

Figure 48.a) product of thermal anneal from 52^{o}C to room temperature. b) product of thermal anneal from 65^{o}C to room temperature.

4.4.3.2 The effect of salt

According to the Schildkraut-Lifson equation,[54] the salt content controls nucleic acid hybridization. Due to the negatively charged nucleic acid backbones, the addition of cations modulates the interaction between the DNA strands, reduces the inter-strand repulsion, and therefore facilitates DNA hybridization.[53, 54] Previous reports on the crystallization of Au nanoparticles have reported the use of 0.5 M NaCl or 0.5M PBS; however, these conditions did not apply to the gold-coated magnetic nanoparticles, and complete precipitation of the particles was not observed under these conditions, possibly

due to the additional magnetic interactions involved in our crystallization. Therefore, I tested a variety of different salt conditions. Figure 13 shows the aggregation of nanoparticles after the addition of the DNA linker strand. The nanoparticles are dissolved in a solution containing different amounts of salt: N1: 1.57 M NaCl, P1: 0.15 M PBS, and P2: 0.093 M PBS. Before the addition of salt, all three solutions are stable. After the addition of DNA linker in 50× excess, they start to aggregate and precipitates form in the bottom of tubes. After a few rounds of centrifugation and removal of excess DNA, followed by redispersal in a solution containing 2.5 mM phosphate buffered saline (PBS), 0.5 M NaCl, precipitates are still present in all three solutions, even though the N1 solution shows a slight sign of dissociation, suggesting that the presence of PBS could be necessary to form more robust aggregates.

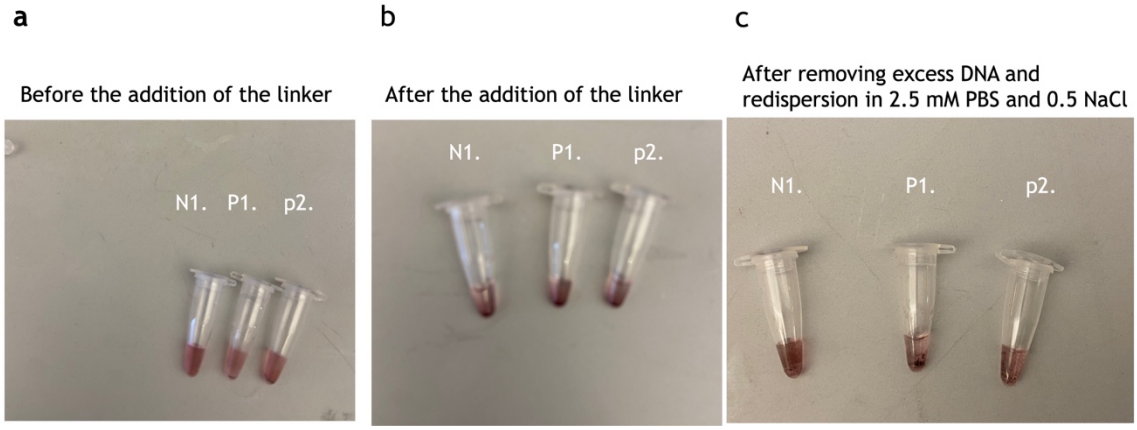

Figure 49. Aggregation of MNPs as a result of hybridization between the DNA linkers and ligands. a) before the addition of linker nanoparticles are stable in solution. b) after the addition of linker nanoparticles precipitate. c) the aggregates are more stable in solutions containing phosphate buffer.

Even though aggregation takes place at a variety of different salt concentrations (Table 1), unfortunately this aggregation doesn't always lead to ordered crystal structure. Table 1 shows the variety of conditions that were tested. Only the conditions in which 0.066 M PBS and 1 M NaCl were used led to superlattice formation. The SEM of these conditions is shown in Figure 16. At lower salt concentrations, even though aggregation and local order (Figure 16 a and c) are observed, the aggregation of the nanoparticles does not lead to ordered structures, possibly because the electrostatic repulsion between the DNAs is insufficiently screened, making the ordered lattice too unstable to form. On the other hand, too high a salt concentration may reduce the repulsive forces too much, causing the nanoparticles to aggregate irreversibly. Additionally, this experiment demonstrates that NaCl has a greater ability to modify the interparticle forces necessary for crystallization. Overall, these preliminary results suggest a complex interplay between a variety of forces, including electrostatic, van der Waals, base pairing, and magnetic dipole-dipole interactions, is responsible for the formation of superlattices. They also suggest that a delicate balance between various attractive and repulsive forces is needed for the ordering process.

Table 2.Different salt conditions for MNPs crystallization.

Salt	a	b	c	d & e
PBS	0.0066 M	0.0066M	0.066M	0.066M
NaCl	1M	0.65M	0.65M	1M

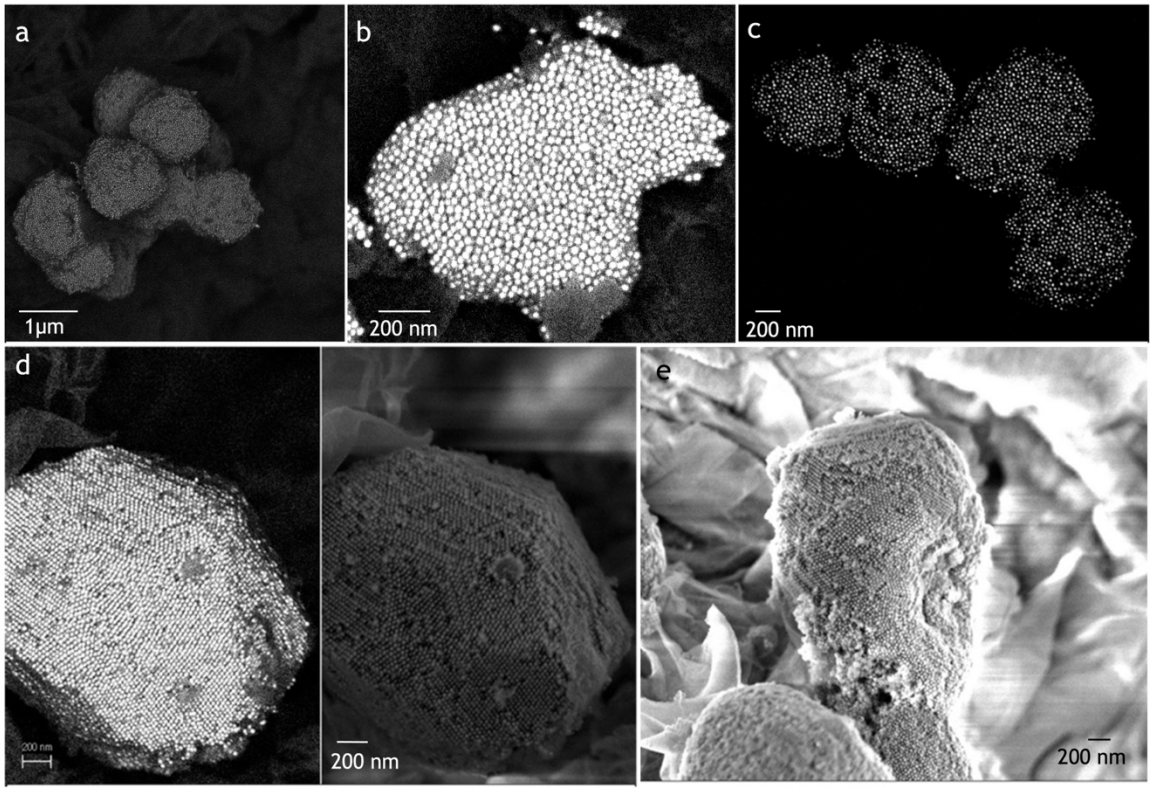

Figure 50.crystallization of MNPs under different salt conditions slow cooling from 70ºC to room temperature at the rate of 0.1 ºC/10 min. a) NaCl 1 M, PBS: 0.0066 M, b) NaCl 0.65 M, PBS: 0.066 M, c) PBS: 0.0066 M, d and e) NaCl 1 M, PBS: 0.066 M.

In order to better characterize the crystal structures, we also performed FFT and image analyses using ImageJ (Figure 17). In the case of a FCC superlattice image, we would expect to see a pattern of bright spots arranged in a specific pattern that corresponds to the diffraction pattern of the superlattice, which is a characteristic of its crystal structure. The diffraction pattern of a FCC lattice has a characteristic cubic symmetry, with spots arranged in a series of concentric rings around the center of the pattern. The rings correspond to the planes of atoms in the lattice that are oriented perpendicular to the direction of the incident beam. The spots on each ring are arranged in a specific pattern, which is related to the spacing between the planes of atoms in the lattice. For the (111) plane of an FCC lattice, the diffraction pattern consists of six sharp spots, which are surrounded by additional spots arranged in a circular pattern.

Figure 17.a depicts the FFT of a few ordered domains; despite the image's low resolution, which makes analysis difficult, the pattern resembles the diffraction pattern of

a FCC lattice. These analyses reveal that the superlattice patterns exhibit, on average, lattice fringes of 22.6 ±1.2 nm and a nearest neighbor distance of 25.5±1.3 which is close to the predicted values of 29.52 nm. [55]

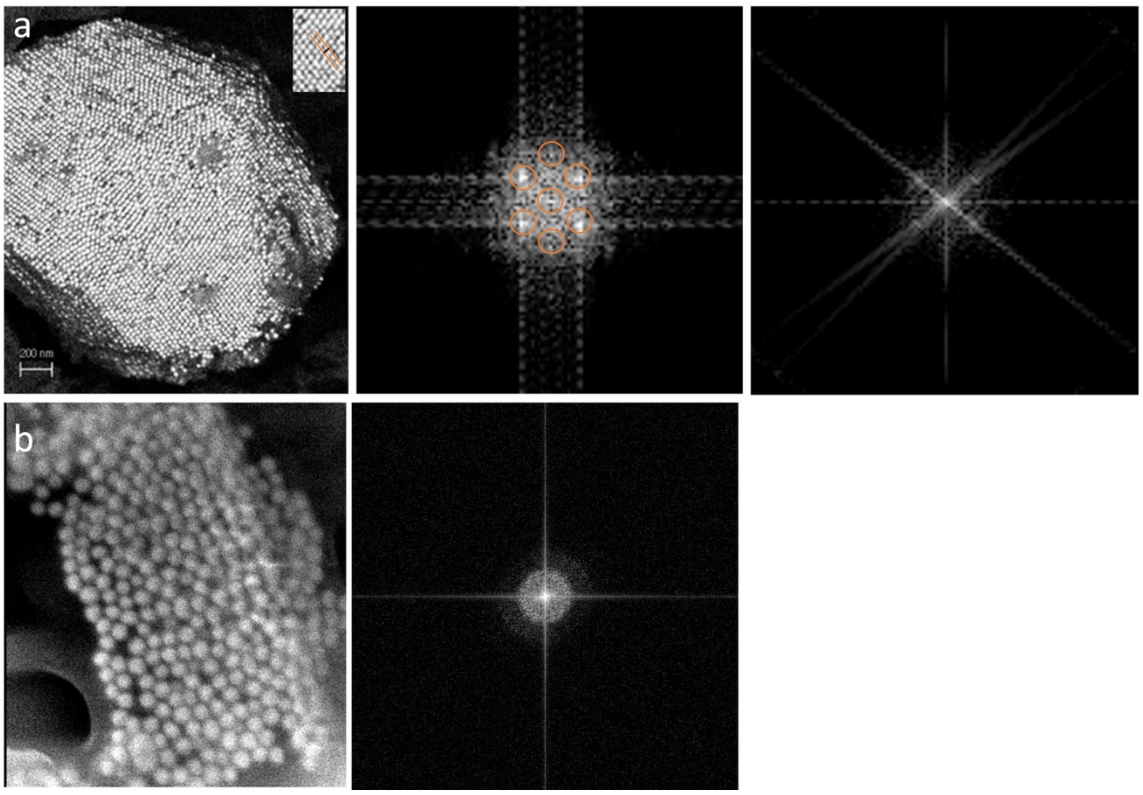

Figure 51.Fast Fourier transform image analysis of a) superlattices b) irregular aggregates using ImageJ shows lattice spacing of 29.4±2.5 nm.

4.4.4 SAXS measurement

The SAXS measurement of gold coated magnetic nanoparticles from 70ºC to 25ºC and crystalized at NaCl 1 M, PBS: 0.066 M is shown in (Figure 16.b). The diffraction peaks are similar to those in the SAXS data of previously reported crystalized 20 nm gold nanoparticle in FCC superlattice (Figure 16.a).

A face-centered cubic (FCC) lattice is a type of crystal lattice that consists of a cube with a lattice point at each corner and an additional lattice point at the center of each face of the cube. When X-rays are scattered by an FCC lattice, the resulting pattern typically exhibits several peaks. Specifically, an FCC lattice gives four Bragg peaks in the small-angle X-ray scattering (SAXS) pattern. These peaks correspond to the (111), (200), (220), and (311) planes of the FCC lattice. The (111) peak is the strongest and appears at the highest scattering angle, while the (200), (220), and (311) peaks are weaker and appear at lower scattering angles. As shown in Table 2, the experiment shows three peaks that correspond to d_{111}, $d_{220,}$ and d_{311}. The peak corresponding to d_{200} seems to be missing in our results, which could be due to a variety of factors such as the low resolution of the instrument, sample structure, experimental conditions, or X-ray beam quality. In SAXS

experiments, the peaks in the scattering intensity versus scattering vector (I vs. q) plot correspond to the positions of the Bragg reflections, which are characteristic of the repeating units of the crystal lattice. The distance between the peaks in the I vs. q plot is proportional to the lattice spacing of the crystal.

Miller indices (hkl)	q (A^o)	d (A^o)
(111)	0.02	314.15
(220)	0.03	209.44
(331)	0.05	125.67

Table 3.summary of diffraction peaks and calculated lattice spacing.

To determine the exact lattice spacing, we can use the Braggs law equation (2), which relates the interplanar spacing (d) of a crystal to the wavelength (λ) and scattering angle (θ) of X-rays. By using basic geometry and the wave properties of X-rays, we can then obtain equation (4), where q is the scattering vector and d is the lattice spacing. The scattering vector (q) is defined as the difference between the wave vectors of the incident and scattered X-rays. For a crystal lattice with planes separated by distance d, the incident X-ray wave is diffracted by the planes to produce a scattered wave that interferes constructively only if the path difference between the two waves is an integer multiple of the wavelength λ. This condition can be expressed as:

$$2d \sin\theta = n\lambda \quad (2)$$

By measuring the position of the peaks in the I vs. q plot and converting the values of q to real space distances using this equation, we can obtain the interplanar spacing of the crystal. Interplanar spacing (d_{hkl}) is the distance between the planes of atoms in a crystal structure. It can be calculated from the positions of the Bragg peaks in the X-ray diffraction pattern and is related to the Miller indices of the crystal planes that give rise to the peaks.

$$d = \lambda/(2 \sin\theta) \quad (3)$$

Using the wave vector $k = 2\pi / \lambda$ and the definition of the scattering vector $q = (k'-k)$, where k' is the scattered wave vector and k is the incident wave vector, we can write:

$$q = 2k \sin\theta \quad (4)$$

$$q = 2\pi/d \quad (5)$$

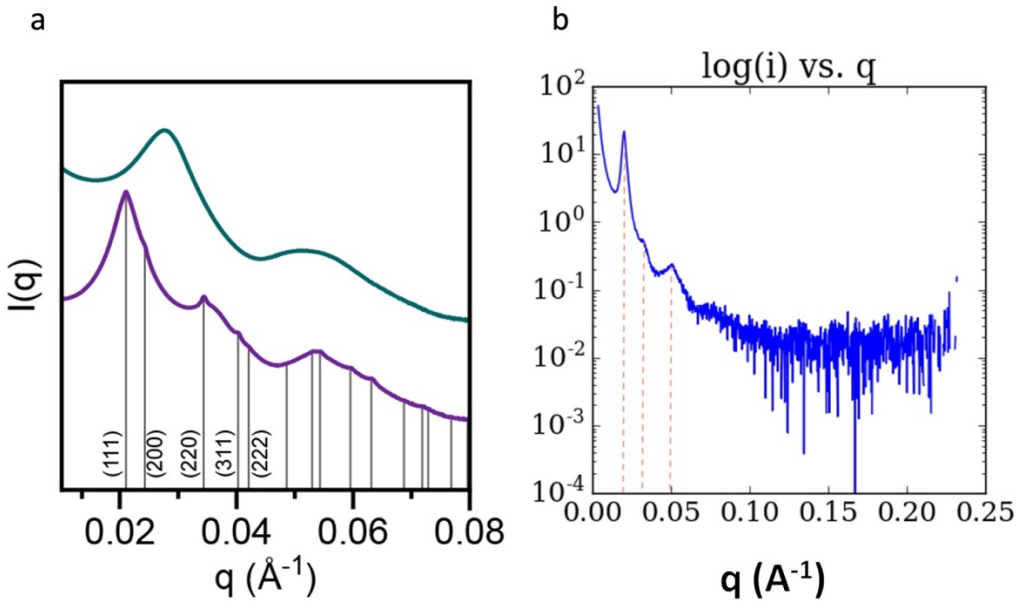

Figure 52.a) fcc superlattice of 20 nm gold nanoparticles.[56] b) fcc superlattice of 20 nm gold coated iron oxide nanoparticle.

Also, for a face-centered cubic (FCC) lattice, the interplanar spacing (d-spacing) between (hkl) planes can be related to the lattice parameter (a) using the following equation:

$$d_{hkl} = a/\sqrt{(h^2+k^2+l^2)} \quad (5)$$

where h, k, and l are the Miller indices that define the (hkl) planes of interest. The Miller indices are integers that represent the orientation and spacing of the crystal lattice planes and are related to the diffraction angles and the interplanar spacing. Based on our experimental data for (111), plane q is about 0.02 (A^{-1}), therefore the lattice spacing (d_{111}) would be around 314.15 Aº. Consequently the lattice parameter is estimated to be around 568.22±34.09Aº

We can also measure the inter-particle distance (b), which is the distance between neighboring particles or molecules in a sample. It is related to the lattice constant in a crystal structure by the equation (5).

$$b = a / \sqrt{2} \quad (6)$$

Using the above equation, the interparticle distance would be 401.85±34.09Aº which is slightly longer than the estimated value of 295.2 Aº based on the size of the nanoparticles, the length of the DNA ligand, and the SEM results. This discrepancy between the SAXS and SEM results could be because SEM results may be affected by the sample preparation process, such as drying or annealing, which can cause shrinkage or distortion of the lattice. SAXS measurements, on the other hand, are performed on the superlattice in solution, which allows for the preservation of the lattice structure in its native environment.

4.5 Summary and Outlook

By utilizing DNA-assisted self-assembly to organize gold-coated magnetic nanoparticles for the first time, this study opens a new window to explore spin ice behavior in thermally active systems and even their magneto-plasmonic collective behaviors. The small size of the particles would change the energy landscape of this system compared to EBL-fabricated artificial spin ices and may result in minimizing the energy barrier and realizing lower-energy states of matter in which exotic behaviors like spin-charge formation, spin liquid phase, etc. may emerge.

Despite the lack of tools to precisely quantify the T_m of our fabricated 3D nanostructures, which is required information for making single crystals, I was able to make an FCC superlattice of 20 nm gold coated magnetic nanoparticles in this study. Using this architecture and the careful design of the DNA linkers and ligands, we can create different superlattices in the future, as well as introduce defects such as nonmagnetic or binary nanoparticles into the system and investigate how defects alter collective behavior and magnetic phases. As these particles are different than their ferromagnetic counterparts, this study may lead to the realization of new phases and states of matter that have not been observed before.

The discussed method also enables tailoring the extent of frustration by carefully designing the lattice spacing or symmetry of the superlattice, which is difficult to achieve using conventional 2D or 3D patterning methods. Future works could also tailor other experimental techniques, such as magnetic susceptibility measurements, magnetization measurements, and neutron scattering, to provide information about the magnetic properties of these self-assembled nanoparticles, such as the magnetic moment distribution and the magnetic anisotropy. The exploration of these novel phenomena could lead to new applications in nanomagnetism, such as information storage and processing.

4.6 References

(1) Mydosh, J. A. Spin glasses: redux: an updated experimental/materials survey. *Reports on Progress in Physics* **2015**, *78* (5), 052501

(2) Tay, Z. A.-O.; Savliwala, S. A.-O.; Hensley, D. W.; Fung, K. A.-O.; Colson, C.; Fellows, B. A.-O.; Zhou, X.; Huynh, Q. A.-O.; Lu, Y.; Zheng, B.; et al. Superferromagnetic Nanoparticles Enable Order-of-Magnitude Resolution & Sensitivity Gain in Magnetic Particle Imaging. (2366-9608 (Electronic)),

(3) Kapaklis, V.; Arnalds, U. B.; Farhan, A.; Chopdekar, R. V.; Balan, A.; Scholl, A.; Heyderman, L. J.; Hjörvarsson, B. Thermal fluctuations in artificial spin ice. *Nature Nanotechnology* **2014**, *9* (7), 514-519

(4) Wiedwald, U.; Gräfe, J.; Lebecki, K. M.; Skripnik, M.; Haering, F.; Schütz, G.; Ziemann, P.; Goering, E.; Nowak, U. Magnetic switching of nanoscale antidot lattices. (2190-4286 (Print)),

(5) Skjærvø, S. H.; Marrows, C. H.; Stamps, R. L.; Heyderman, L. J. Advances in artificial spin ice. *Nature Reviews Physics* **2020**, *2* (1), 13-28

(6) Cheng, H. A.-O.; Distler, M. A.-O.; Lee, B. A.-O.; Zhou, W. A.-O.; Weigand, S.; Mirkin, C. A.-O. Nanoparticle Superlattices through Template-Encoded DNA Dendrimers. (1520-5126 (Electronic)),

(7) Macfarlane, R. J.; Lee, B.; Jones, M. R.; Harris, N.; Schatz, G. C.; Mirkin, C. A. Nanoparticle Superlattice Engineering with DNA. *Science* **2011**, *334* (6053), 204-208

(8) Auyeung, E.; Morris, W.; Mondloch, J. E.; Hupp, J. T.; Farha, O. K.; Mirkin, C. A. Controlling Structure and Porosity in Catalytic Nanoparticle Superlattices with DNA. *Journal of the American Chemical Society* **2015**, *137* (4), 1658-1662

(9) Harris, M. J.; Bramwell, S. T.; McMorrow, D. F.; Zeiske, T.; Godfrey, K. W. Geometrical Frustration in the Ferromagnetic Pyrochlore ${\mathrm{Ho}}_{2}{\mathrm{Ti}}_{2}{O}_{7}$. *Physical Review Letters* **1997**, *79* (13), 2554-2557

(10) Castelnovo, C.; Moessner R Fau - Sondhi, S. L.; Sondhi, S. L. Magnetic monopoles in spin ice. (1476-4687 (Electronic)),

(11) Chopdekar, R. V.; Duff, G.; Hügli, R. V.; Mengotti, E.; Zanin, D. A.; Heyderman, L. J.; Braun, H. B. Controlling vortex chirality in hexagonal building blocks of artificial spin ice. *New Journal of Physics* **2013**, *15* (12), 125033

(12) Bramwell, S. T.; Harris, M. J. The history of spin ice. *Journal of Physics: Condensed Matter* **2020**, *32* (37), 374010

(13) Greedan, J. E. Frustrated rare earth magnetism: Spin glasses, spin liquids and spin ices in pyrochlore oxides. *Journal of Alloys and Compounds* **2006**, *408-412*, 444-455

(14) Schiffer, P.; Nisoli, C. Artificial spin ice: Paths forward. *Applied Physics Letters* **2021**, *118* (11), 110501

(15) Wang, R. F.; Nisoli, C.; Freitas, R. S.; Li, J.; McConville, W.; Cooley, B. J.; Lund, M. S.; Samarth, N.; Leighton, C.; Crespi, V. H.; et al. Artificial 'spin ice' in a geometrically frustrated lattice of nanoscale ferromagnetic islands. *Nature* **2006**, *439* (7074), 303-306

(16) Tokiwa, Y.; Yamashita, T.; Udagawa, M.; Kittaka, S.; Sakakibara, T.; Terazawa, D.; Shimoyama, Y.; Terashima, T.; Yasui, Y.; Shibauchi, T.; et al. Possible observation of highly itinerant quantum magnetic monopoles in the frustrated pyrochlore Yb2Ti2O7. *Nature Communications* **2016**, *7* (1), 10807

(17) Wang, Y.; Reeder, T.; Karaki, Y.; Kindervater, J.; Halloran, T.; Maliszewskyj, N.; Qiu, Y.; Rodriguez, J. A.; Gladchenko, S.; Koohpayeh, S. M.; et al. Monopolar and dipolar relaxation in spin ice Ho2Ti2O7. *Science Advances 7* (25), eabg0908

(18) Samarakoon, A. M.; Barros, K.; Li, Y. W.; Eisenbach, M.; Zhang, Q.; Ye, F.; Sharma, V.; Dun, Z. L.; Zhou, H.; Grigera, S. A.; et al. Machine-learning-assisted insight into spin ice Dy2Ti2O7. *Nature Communications* **2020**, *11* (1), 892

(19) Borzi, R. A.; Gómez Albarracín, F. A.; Rosales, H. D.; Rossini, G. L.; Steppke, A.; Prabhakaran, D.; Mackenzie, A. P.; Cabra, D. C.; Grigera, S. A. Intermediate magnetization state and competing orders in Dy2Ti2O7 and Ho2Ti2O7. *Nature Communications* **2016**, *7* (1), 12592

(20) Ruokokoski, E.; Pietilä, V.; Möttönen, M. Ground-state Dirac monopole. *Physical Review A* **2011**, *84* (6), 063627

(21) Arava, H.; Vedmedenko, E. Y.; Cui, J.; Vijayakumar, J.; Kleibert, A.; Heyderman, L. J. Control of emergent magnetic monopole currents in artificial spin ice. *Phys. Rev. B* **2020**, *102* (14), 144413

(22) Gingras, M. J. P.; McClarty, P. A. Quantum spin ice: a search for gapless quantum spin liquids in pyrochlore magnets. *Reports on Progress in Physics* **2014**, *77* (5), 056501

(23) Farhan, A.; Kleibert, A.; Derlet, P. M.; Anghinolfi, L.; Balan, A.; Chopdekar, R. V.; Wyss, M.; Gliga, S.; Nolting, F.; Heyderman, L. J. Thermally induced magnetic relaxation in building blocks of artificial kagome spin ice. *Phys. Rev. B* **2014**, *89* (21), 214405

(24) Möller, G.; Moessner, R. Magnetic multipole analysis of kagome and artificial spin-ice dipolar arrays. *Phys. Rev. B* **2009**, *80* (14), 140409

(25) Hügli, R. V.; Duff G Fau - O'Conchuir, B.; O'Conchuir B Fau - Mengotti, E.; Mengotti E Fau - Rodríguez, A. F.; Rodríguez Af Fau - Nolting, F.; Nolting F Fau - Heyderman, L. J.; Heyderman Lj Fau - Braun, H. B.; Braun, H. B. Artificial kagome spin ice: dimensional reduction, avalanche control and emergent magnetic monopoles. (1364-503X (Print)),

(26) Wen, T.; Majetich, S. A. Ultra-Large-Area Self-Assembled Monolayers of Nanoparticles. *ACS Nano* **2011**, *5* (11), 8868-8876

(27) Toulemon, D.; Liu, Y.; Cattoën, X.; Leuvrey, C.; Bégin-Colin, S.; Pichon, B. P. Enhanced Collective Magnetic Properties in 2D Monolayers of Iron Oxide Nanoparticles

Favored by Local Order and Local 1D Shape Anisotropy. *Langmuir* **2016**, *32* (6), 1621-1628

(28) Koo, J.; Kim, H.; Kim, K.-Y.; Jang, Y. R.; Lee, J.-S.; Yoon, S. W.; Suh, B. J.; Yu, T.; Bang, J.; Yoon, K.; et al. Controlling the magnetic properties of polymer–iron oxide nanoparticle composite thin films via spatial particle orientation. *RSC Advances* **2016**, *6* (61), 55842-55847

(29) Park, S.; Urbach, Z.; Brisbois, C.; Parker, K.; Partridge, B.; Oh, T.; Dravid, V.; de la Cruz, M.; Mirkin, C. DNA- and Field-Mediated Assembly of Magnetic Nanoparticles into High-Aspect Ratio Crystals. *Advanced Materials* **2020**, *32* (4),

(30) Park, S. Y.; Lytton-Jean, A. K. R.; Lee, B.; Weigand, S.; Schatz, G. C.; Mirkin, C. A. DNA-programmable nanoparticle crystallization. *Nature* **2008**, *451* (7178), 553-556

(31) Nykypanchuk, D.; Maye, M. M.; van der Lelie, D.; Gang, O. DNA-guided crystallization of colloidal nanoparticles. *Nature* **2008**, *451* (7178), 549-552

(32) Meyer, T. A.; Zhang, C.; Bao, G.; Ke, Y. Programmable Assembly of Iron Oxide Nanoparticles Using DNA Origami. *Nano Letters* **2020**, *20* (4), 2799-2805

(33) Badini Confalonieri, G. A.; Vega, V.; Ebbing, A.; Mishra, D.; Szary, P.; Prida, V. M.; Petracic, O.; Zabel, H. Template-assisted self-assembly of individual and clusters of magnetic nanoparticles. *Nanotechnology* **2011**, *22* (28), 285608

(34) Price, S. L. Predicting crystal structures of organic compounds. *Chemical Society Reviews* **2014**, *43* (7), 2098-2111

(35) Woodley, S. M.; Catlow, R. Crystal structure prediction from first principles. (1476-4660 (Electronic)),

(36) Zhang, C.; Macfarlane Rj Fau - Young, K. L.; Young Kl Fau - Choi, C. H. J.; Choi Ch Fau - Hao, L.; Hao L Fau - Auyeung, E.; Auyeung E Fau - Liu, G.; Liu G Fau - Zhou, X.; Zhou X Fau - Mirkin, C. A.; Mirkin, C. A. A general approach to DNA-programmable atom equivalents. (1476-4660 (Electronic)),

(37) Macfarlane, R. J.; Jones Mr Fau - Senesi, A. J.; Senesi Aj Fau - Young, K. L.; Young Kl Fau - Lee, B.; Lee B Fau - Wu, J.; Wu J Fau - Mirkin, C. A.; Mirkin, C. A. Establishing the design rules for DNA-mediated programmable colloidal crystallization. (1521-3773 (Electronic)),

(38) Seo, S. E.; Wang, M. X.; Shade, C. M.; Rouge, J. L.; Brown, K. A.; Mirkin, C. A. Modulating the Bond Strength of DNA–Nanoparticle Superlattices. *ACS Nano* **2016**, *10* (2), 1771-1779

(39) Urbach, Z.; Park, S.; Weigand, S.; Rix, J.; Lee, B.; Mirkin, C. Probing the Consequences of Cubic Particle Shape and Applied Field on Colloidal Crystal Engineering with DNA. *Angewandte Chemie-International Edition* **2021**, *60* (8), 4065-4069

(40) Sharma, J.; Chhabra, R.; Andersen, C. S.; Gothelf, K. V.; Yan, H.; Liu, Y. Toward Reliable Gold Nanoparticle Patterning On Self-Assembled DNA Nanoscaffold. *Journal of the American Chemical Society* **2008**, *130* (25), 7820-7821

(41) Lalander, C. H.; Zheng, Y.; Dhuey, S.; Cabrini, S.; Bach, U. DNA-Directed Self-Assembly of Gold Nanoparticles onto Nanopatterned Surfaces: Controlled Placement of Individual Nanoparticles into Regular Arrays. *ACS Nano* **2010**, *4* (10), 6153-6161

(42) Julin, S.; Nummelin, S.; Kostiainen, M. A.; Linko, V. DNA nanostructure-directed assembly of metal nanoparticle superlattices. *Journal of Nanoparticle Research* **2018**, *20* (5), 119

(43) Freitas, M.; Sá Couto, M.; Barroso, M. F.; Pereira, C.; de-los-Santos-Álvarez, N.; Miranda-Ordieres, A. J.; Lobo-Castañón, M. J.; Delerue-Matos, C. Highly Monodisperse Fe3O4@Au Superparamagnetic Nanoparticles as Reproducible Platform for Genosensing Genetically Modified Organisms. *ACS Sensors* **2016**, *1* (8), 1044-1053

(44) Hurst, S.; Lytton-Jean, A.; Mirkin, C. Maximizing DNA loading on a range of gold nanoparticle sizes. *Analytical Chemistry* **2006**, *78* (24), 8313-8318

(45) Macfarlane, R. J.; Lee, B.; Hill, H. D.; Senesi, A. J.; Seifert, S.; Mirkin, C. A. Assembly and organization processes in DNA-directed colloidal crystallization. *Proceedings of the National Academy of Sciences* **2009**, *106* (26), 10493-10498

(46) Auyeung, E.; Macfarlane, R. J.; Choi, C. H. J.; Cutler, J. I.; Mirkin, C. A. Transitioning DNA-Engineered Nanoparticle Superlattices from Solution to the Solid State. *Advanced Materials* **2012**, *24* (38), 5181-5186

(47) Teja, A. S.; Koh, P.-Y. Synthesis, properties, and applications of magnetic iron oxide nanoparticles. *Progress in Crystal Growth and Characterization of Materials* **2009**, *55* (1), 22-45

(48) Xie, J.; Peng, S.; Brower, N.; Pourmand, N.; Wang, S. X.; Sun, S. One-pot synthesis of monodisperse iron oxide nanoparticles for potential biomedical applications. **2006**, *78* (5), 1003-1014

(49) Wang, L.; Park, H.-Y.; Lim, S. I. I.; Schadt, M. J.; Mott, D.; Luo, J.; Wang, X.; Zhong, C.-J. Core@shell nanomaterials: gold-coated magnetic oxide nanoparticles. *Journal of Materials Chemistry* **2008**, *18* (23), 2629-2635

(50) Smith, M.; McKeague, M.; DeRosa, M. C. Synthesis, transfer, and characterization of core-shell gold-coated magnetic nanoparticles. *MethodsX* **2019**, *6*, 333-354

(51) WangWang; Luo, J.; Fan, Q.; Suzuki, M.; Suzuki, I. S.; Engelhard, M. H.; Lin, Y.; Kim, N.; Wang, J. Q.; Zhong, C.-J. Monodispersed Core−Shell Fe3O4@Au Nanoparticles. *J. Phys. Chem. B* **2005**, *109* (46), 21593-21601

(52) Xu, Z.; Hou, Y.; Sun, S. Magnetic Core/Shell Fe3O4/Au and Fe3O4/Au/Ag Nanoparticles with Tunable Plasmonic Properties. *Journal of the American Chemical Society* **2007**, *129* (28), 8698-8699

(53) Hurst, S. J.; Hill, H. D.; Mirkin, C. A. "Three-Dimensional Hybridization" with Polyvalent DNA−Gold Nanoparticle Conjugates. *Journal of the American Chemical Society* **2008**, *130* (36), 12192-12200

(54) Rose, K.; Mason Jo Fau - Lathe, R.; Lathe, R. Hybridization parameters revisited: solutions containing SDS. (0736-6205 (Print)),

(55) Marko, J. F. 1 - DNA Mechanics. In *Nuclear Architecture and Dynamics*, Lavelle, C., Victor, J.-M. Eds.; Vol. 2; Academic Press, 2018; pp 3-40.

(56) Oh, T.; Park, S. S.; Mirkin, C. A. Stabilization of Colloidal Crystals Engineered with DNA. *Advanced Materials* **2019**, *31* (1), 1805480